

FINAL REPORT

J.L. Volakis, L.C. Kempel, R. Sliva, H.T.G.Wang and A. G.Woo

National Aeronautics and
Space Administration
Ames Research Center
Moffett Field, CA 94035

Naval Weapons Center
China Lake, CA 93555-6001

September 1994

N95-12382

Unclass

G3/32 0026404



THE UNIVERSITY OF MICHIGAN

Radiation Laboratory
Department of Electrical Engineering
and Computer Science
Ann Arbor, Michigan 48109-2122
USA

(NASA-CR-195211) ANALYSIS OF
CYLINDRICAL WRAP-AROUND AND DOUBLY
CONFORMAL PATCH ANTENNAS BY WAY OF
THE FINITE ELEMENT-ARTIFICIAL
ABSORBER METHOD Final Report
(Michigan Univ.) 68 p

NASA Interchange No. NCA2-839
FINAL REPORT

Grant Interchange Title: Analysis of Cylindrical Wrap-Around and Doubly Conformal Patch Antennas Via the Finite Element-Artificial Absorber Method

Report Title : Final Report

Report Authors: J.L. Volakis, L.C. Kempel, R. Sliva, H.T.G. Wang and A.G. Woo

Primary University Collaborator: John L. Volakis
volakis@engin.umich.edu
Telephone: (313) 764-0500

Primary NASA-Ames Collaborator: Alex Woo
woo@ra-next.arc.nasa.gov
Telephone: (415) 604-6010

University Address: Radiation Laboratory
Department of Electrical Engineering
and Computer Science
The University of Michigan
Ann Arbor, MI 48109-2122

Date: September 30, 1994

Funds for the support of this study have been allocated in part of the NASA-Ames Research Center, Moffett Field, California, under interchange No. NCA2-839

Table of Contents

Executive Summary.....	1
FE-ABC Formulation for Patch Antennas on a Circular Cylinder.....	5
Radiation by Cavity-backed Antennas on a Circular Cylinder.....	21
Scattering by Cavity-backed Antennas on a Circular Cylinder.....	45
A Hybrid Finite Element-Boundary Integral Method for the Analysis of Cavity-Backed Antennas of Arbitrary Shape.....	57

EXECUTIVE SUMMARY

J.L. Volakis, L.C. Kempel, R.J. Sliva, H. Wang and A. Woo

Project Goal

The goal of this project was to develop analysis codes for computing the scattering and radiation of antennas on cylindrically and doubly conformal platforms. Available techniques and codes can only treat antennas on planar surfaces whereas in most cases (missile and aircraft platforms), the printed antennas are situated in cylindrical or doubly curved surfaces. Modern vehicle platforms are also composite and/or coated with dielectric materials and this presents an additional challenge in the analysis.

Progress Summary

Because of our previous experience in finite element and boundary integral methods, a hybrid finite element-boundary integral (FE-BI) method was employed for the analysis of patch antennas on planar and cylindrical platforms. The main challenge in this implementation was the efficient evaluation of the cylinder's Green's function in a form useful for the FE-BI method. After 4 months of preparatory work, both the FE-BI formulation and the Green's function evaluation were completed and programmed in a rather general purpose computer code. This is the first code of its kind for the analysis of antennas on cylindrical platforms and because of its future utility, several user-oriented features were included with it. The code is referred to as FEMA-CYL (**F**inite **E**lement **M**ethod for **A**ntennas on **C**ylinders) and has already been delivered to NASA and Navy users along with a test case and users manual. To validate the code, measurements were performed by J. Silva at the Naval Weapons Center, China Lake and these overlaid the calculations.

Over the last few months of the project period, we concentrated on the extension of the FEMA-CYL code to antennas on coated and possibly doubly conformal platforms. Such a requirement precludes use of the boundary integral method for terminating the mesh because integral equations are inefficient for modeling doubly conformal surfaces. Consequently, we examined a class of new absorbing boundary conditions (ABCs) for terminating the finite element mesh. These ABCs proved quite accurate for antenna

applications and their performance and capability is described in the first section of this final report. Also, an earlier report describes a comparison of the computational advantages associated with ABC and boundary mesh terminations(see U-M Radiation Laboratory report 031173-1-T). The implementation of the finite element-ABC formulation resulted in the code FEMA-CYLA and we are currently preparing a users manual for this code. Note that this code is capable of analyzing antennas embedded in coated platforms and results are included at least for one of those situations. In addition, we began the development of a finite element formulation for modeling non-rectangular printed antennas on doubly conformal platforms. This formulation employs prismatic elements which are most suitable for coupling with triangular surface meshes in generating the volume mesh. For typical patch antennas we anticipate that the mesh generation will be done without a need to use a external meshing facilities.

A total of three reports and 4 journal papers were published as a result of this consortium agreement:

REPORTS

"A comparative study of an ABC and an artificial absorber for truncating finite element meshes" Univ. of Michigan Radiation Laboratory Technical Report 031173-1-T

This report compares three different techniques for terminating the finite element mesh in modeling conformal patch antennas and slot arrays. 15pp.

"Radiation and scattering from cylindrically conformal printed antennas" Univ. of Michigan Radiation Laboratory Technical Report 031173-2-T, 166pp.

This is an extensive report describing the theory and capabilities of the FEMA-CYL code. Many results for scattering and radiation by cylindrically conformal antennas are included along with measurements.

"Radiation and scattering from antennas in coated conformal platforms" Univ. of Michigan Radiation Laboratory Technical Report 031173-3-T (this report)

This is the final report and contains several sections which highlight the research activity over the length of the project/consortium agreement. The report contains the following sections:

1. *FE-ABC formulation for patch antennas on a coated circular cylinder*--describes the formulation of the FEMA-CYLA code.
2. *Radiation by cavity-backed antennas on a circular cylinder*--describes the performance of the FEMA-CYL code for antenna radiation analysis and includes the measured results collected by J. Silva at the Naval Weapons Center, China Lake, CA. This section has been submitted as a paper to *IEE Proceedings-Pt. H*. The paper is co-authored with J.Silva
3. *Scattering by cavity-backed antennas on a circular cylinder*--describes the performance of the FEMA-CYL code for computing antenna scattering. This section is a reprint of the journal paper which appeared in *IEEE Trans. Antennas & Propagat.*, Vol. 42, Sept. 1994, pp. 1268-1279.
4. *A Hybrid finite element-boundary integral method for the analysis of cavity-backed antennas of arbitrary shape*--describes the basics of the finite element-boundary integral formulation for modeling conformal antennas. This section is a reprint of the journal paper which appeared in *IEEE Trans. Antennas & Propagat.* Vol. 42, Sept. 1994, pp. 1233-1242. It is co-authored with A. Woo (NASA-Ames) and H. Wang(Naval Weapons Center)

Journal Papers

J. Gong, J.L. Volakis, A.C. Woo and H.T. G. Wang, "A hybrid finite element method for the analysis of cavity-backed antennas of arbitrary shape," *IEEE Trans Antennas Propagat.*, vol. 42, Sept. 1994, pp. 1233-1242.

L.C. Kempel and J. L. Volakis, "Scattering by cavity-backed antennas on a circular cylinder," *IEEE Trans. Antennas & Propagat.*, Vol. 42, Sept. 1994, pp. 1268-1279.

L.C. Kempel, J.L., Volakis and J. Silva, "Radiation by cavity-backed antennas on a circular cylinder," submitted for publication *IEE Proceedings, Pt. H*.

T. Ozdemir and J.L. Volakis, "A comparative study of an ABC and an artificial absorber for truncating finite element meshes," *Radio Science*, to appear in 1995

FE-ABC FORMULATION FOR PATCH ANTENNAS ON A CIRCULAR CYLINDER

Leo C. Kempel and John L. Volakis
The University of Michigan
Radiation Laboratory
1301 Beal Ave.
Ann Arbor, MI 48109-2122

Abstract

The finite element-boundary integral (FE-BI) method has been shown to accurately model the scattering and radiation of cavity-backed patch antennas. Unfortunately, extension of this rigorous technique to coated or doubly curved platforms is cumbersome and inefficient. An alternative approximate approach is to employ an absorbing boundary condition for terminating the finite element mesh thus avoiding use of a Green's function. In this report, a FE-ABC method is used to calculate the radar cross section (RCS) and radiation pattern of a cavity-backed patch antenna which is recessed within a metallic surface. It is shown that this approach is accurate for RCS and antenna pattern calculations with an ABC surface displaced as little as 0.3λ from the cavity aperture. These patch antennas may have a dielectric overlay which may also be modelled with this technique.

1 Introduction

Recently, a Finite Element-Boundary Integral (FE-BI) formulation was proposed by the authors [1] for modeling the scattering and radiation of cavity-backed patch antennas recessed in a cylindrical platform. The use of the boundary integral for terminating the FE mesh renders the FE-BI method numerically exact but leads to a partially full and partially sparse matrix. To obtain a fully sparse system, we must use approximate local boundary conditions for terminating the FE mesh and this is usually done by employing absorbing boundary conditions (ABCs).

In this report, a new conformal ABC recently introduced by Chatterjee and Volakis [2] will be used for scattering and radiation parameter calculations in connection with cavity-backed antenna elements on a cylindrical

platform. This second order conformal ABC allows the closure surface to be brought quite close to the cavity aperture. As a result, the required degrees of freedom are significantly less than the number typically used with traditional spherical surface/boundary condition such as the one proposed by Peterson [3] or the one introduced by Webb and Kanellopoulos [4]. The accuracy of this FE-ABC method will be established along with guidelines for the distance between the structure and the ABC boundary. In addition, this new FE-ABC approach will be used to compute the radiation pattern and input impedance of conformal patch antennas with a dielectric overlay.

2 Formulation

Consider the computational domain shown in Figure 1. There are two volume

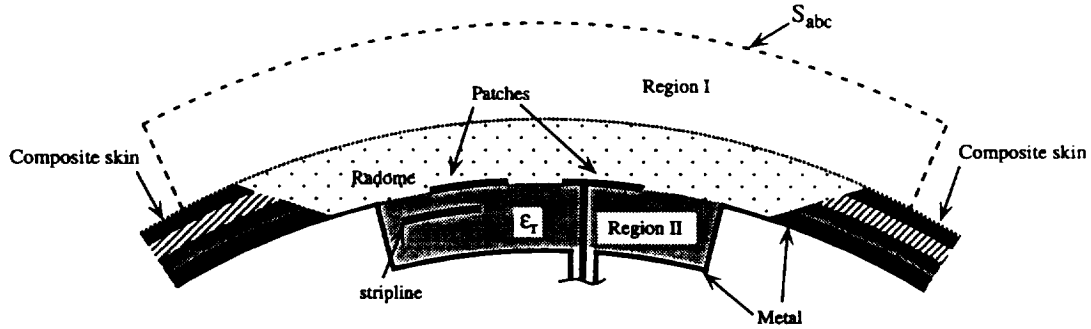


Figure 1: Typical coated cavity-backed patch antenna with ABC mesh termination.

regions: an exterior region, V^I , which includes any radome overlay and an interior region, V^{II} . Both regions may be inhomogeneous and are separated by the aperture surface, S^{ap} , and the surface metallization surface, S^{sm} both of which lie on the surface of the metallic cylinder ($\rho = a$). Thus, the exterior region is defined by $\rho \geq a$ while the interior region has $\rho \leq a$. The computational domain is bounded by the union of the metallic surface, $S^{metal} = S^{sm} + S^{cm}$ where S^{cm} is the metallic walls of the cavity and the ABC surface, S^{abc} .

Within the computational volume, the total electric fields may be written as

$$\begin{aligned}\vec{E}(\vec{r}) &= \vec{E}^I(\vec{r}) + \vec{E}^{cyl}(\vec{r}) \quad \vec{r} \in V^I \\ &= \vec{E}^{II}(\vec{r}) \quad \vec{r} \in V^{II}\end{aligned}\quad (1)$$

where $\vec{E}^{cyl}(\vec{r}) = \vec{E}^i(\vec{r}) + \vec{E}^r(\vec{r})$ as before. The total magnetic fields are likewise written

$$\begin{aligned}\vec{H}(\vec{r}) &= \vec{H}^I(\vec{r}) + \vec{H}^{cyl}(\vec{r}) \quad \vec{r} \in V^I \\ &= \vec{H}^{II}(\vec{r}) \quad \vec{r} \in V^{II}\end{aligned}\quad (2)$$

where $\vec{H}^{cyl}(\vec{r}) = \vec{H}^i(\vec{r}) + \vec{H}^r(\vec{r})$. The boundary conditions are readily written in terms of the electric and magnetic fields. Within the cavity, the tangential electric field vanishes on the metallic walls

$$\hat{n} \times \vec{E}^{II}(\vec{r}) = 0 \quad \vec{r} \in S^{cm} \quad (3)$$

while on the aperture, the total tangential fields are continuous

$$\begin{aligned}\hat{n} \times \vec{E}^I(\vec{r}) &= \hat{n} \times \vec{E}^{II}(\vec{r}) \quad \vec{r} \in S^{ap} \\ \hat{n} \times \vec{H}^I(\vec{r}) &= \hat{n} \times \vec{H}^{II}(\vec{r}) - \hat{n} \times \vec{H}^{cyl}(\vec{r}) \quad \vec{r} \in S^{ap}\end{aligned}\quad (4)$$

On metallic surfaces, all tangential electric fields vanish, i.e.

$$\hat{n} \times \vec{E}^{cyl}(\vec{r}) = \hat{n} \times \vec{E}^I(\vec{r}) = \hat{n} \times \vec{E}^{II}(\vec{r}) = 0 \quad \vec{r} \in S^{sm} \quad (5)$$

while $\hat{n} \times \vec{E}^{cyl}(\vec{r})$ also vanishes over the aperture

$$\hat{n} \times \vec{E}^{cyl}(\vec{r}) = 0 \quad \vec{r} \in S^{ap} \quad (6)$$

since it contains both the incident and reflected fields. Thus, the only non-zero electric fields on the surface of the metallic cylinder correspond to the unknown fields within each region which are continuous across the surface aperture as implied by (4).

The FE equations may be developed by considering the inhomogeneous vector wave equation. Employing the method of weighted residuals and

Green's first vector identity, the weak form of the vector wave equation

$$\begin{aligned}
& \int_{V_i} \frac{\nabla \times \vec{E}(\rho, \phi, z) \cdot \nabla \times \vec{W}_i(\rho, \phi, z)}{\mu_r(\rho, \phi, z)} \rho d\rho d\phi dz \\
& - k_o^2 \int_{V_i} \epsilon_r(\rho, \phi, z) \vec{E}(\rho, \phi, z) \cdot \vec{W}_i(\rho, \phi, z) \rho d\rho d\phi dz \\
& - j k_o Z_o \oint_{S_i} \hat{n}(\rho, \phi, z) \times \vec{H}(\rho, \phi, z) \cdot \vec{W}_i(\rho, \phi, z) dS = f_i^{int} \quad (7)
\end{aligned}$$

where $\hat{n}(\rho, \phi, z)$ indicates the outward pointing normal of the element surface associated with the i th unknown, S_i is the surface area of that element, and $\vec{H}(\rho, \phi, z)$ is the total magnetic field. It can be shown that the surface integral of (7) vanishes for all elements which do not border the cavity aperture. Furthermore, their non-zero contribution is limited to the portion of their surface which coincides with the aperture. The interior source functional, f_i^{int} , is once again given by

$$f_i^{int} = - \int_{V_i} \left\{ \nabla \times \left[\frac{\vec{M}^i(\rho, \phi, z)}{\mu_r(\rho, \phi, z)} \right] + j k_o Z_o \vec{J}^i(\rho, \phi, z) \right\} \cdot \vec{W}_i(\rho, \phi, z) \rho d\rho d\phi dz$$

where \vec{M}^i and \vec{J}^i are impressed currents within the cavity.

A domain decomposition is accomplished by substituting the total field relationships (1) and (2) into (7) and after some manipulation we get the FE-ABC equation

$$\begin{aligned}
& \int_{V_i^I} \left[\frac{\nabla \times \vec{E}^I \cdot \nabla \times \vec{W}_i}{\mu_r} - k_o^2 \epsilon_r \vec{E}^I \cdot \vec{W}_i \right] dV + \\
& \int_{V_i^{II}} \left[\frac{\nabla \times \vec{E}^{II} \cdot \nabla \times \vec{W}_i}{\mu_r} - k_o^2 \epsilon_r \vec{E}^{II} \cdot \vec{W}_i \right] dV + \\
& \int_{S_i^{abc}} (\hat{n} \times \nabla \times \vec{E}^I) \cdot \vec{W}_i dS = f_i^{int} + j \frac{k_o Z_o}{\mu_{re}} \int_{S_i^{ap}} (\hat{\rho} \times \vec{H}^{cyl}) \cdot \vec{W}_i dS - \\
& k_o^2 \int_{V_i^{Id}} \left[\frac{1}{\mu_r} - \epsilon_r \right] \vec{E}^{cyl} \cdot \vec{W}_i dV - j k_o Z_o \left[\frac{1}{\mu_{ri}} - \frac{1}{\mu_{re}} \right] \int_{S_i^{Id}} \hat{n} \cdot [\vec{W}_i \times \vec{H}^{cyl}] dS \quad (9)
\end{aligned}$$

where S_i^{ap} denotes integration of the aperture associated with the i^{th} unknown, S_i^{Id} is associated with integration over the bounding surface of any

dielectric elements in the exterior region, μ_{ri} is the relative permeability of the elements interior to S_i^{fd} whereas μ_{re} is the permeability exterior to that surface.

This set of FE-ABC equations may be written as a linear system of equations

$$\left[\mathcal{A}_{fe-abc} \right] \begin{Bmatrix} E_j^{ap} \\ E_j^{int} \end{Bmatrix} = \begin{Bmatrix} f_i^{ext(abc)} \\ f_i^{int} \end{Bmatrix} \quad (10)$$

where the FE matrix $[\mathcal{A}_{\Gamma-\Gamma U}]$ may be written as a sum of the FE matrix used in the FE-BI formulation [1] and a second term attributed to the ABC surface

$$[\mathcal{A}_{\Gamma-\Gamma U}] = [\mathcal{A}] + [\mathcal{A}^{\Gamma U}] \quad (11)$$

The new FE-ABC equation (9) is comparable to (7) except that the latter utilizes a total field formulation throughout the computational domain. However, previously we utilized an integral expression for the total magnetic field across the aperture which resulted in the FE-BI equation used in [1]. Such an integral expression provides an exact relationship between the total tangential electric and magnetic fields over the aperture surface which also formed the computational domain boundary. Alternatively, we may employ an approximate relationship between these two fields with the goal of retaining the sparsity of the resulting linear system. Additionally, as shown in (9), this FE-ABC formulation may be used for coated as well as uncoated geometries. In the next section, we will develop an approximate relationship suitable for mesh closure.

3 Conformal ABCs

Traditional three-dimensional vector ABCs [3, 4] require a spherical outer boundary which results in an excessive number of unknowns. New conformal ABCs have recently been proposed by Chatterjee and Volakis [2] which have an outer boundary that follows the contour of the enclosed geometry resulting in a minimal number of unknowns. In this section, the specific expressions required by this new ABC for a cylindrical-rectangular box boundary will be derived. A definition of ABC order will be given and subsequently the first- and second-order ABC expressions will be presented.

For the purposes of discussion, we define a secondary field as the field which is a consequence of equivalent currents that are supported by some primary source which is either external or internal to the computational domain. Thus for scattering problems, the scattered field is the secondary field while the incident and reflected fields are considered primary fields. Likewise, for a radiation problem, the radiated field is the secondary field whereas the source field due to an impressed current is the primary field. In (9), we recognize that an ABC must supply a relationship between the tangential components of magnetic and electric *secondary* fields on the absorbing boundary, S^{abc} .

The secondary field may be expressed as a Wilcox expansion

$$\vec{E}^s(n, t_1, t_2) = \frac{e^{-jk_o n}}{4\pi\sqrt{u}} \lim_{P \rightarrow \infty} \sum_{p=0}^P \frac{\vec{E}_p^s(t_1, t_2)}{u^p} \quad (12)$$

where $u = \sqrt{R_1 R_2}$, $R_i = \rho_i + n$ and ρ_i is a principal radius of curvature. In this form, the curvature of the non-spherical wavefront is explicitly used. The point of observation is given in Dupin coordinates as

$$x = n\hat{n} + \vec{x}_o(t_1, t_2) \quad (13)$$

where \hat{n} is the unit normal and $\vec{x}_o(t_1, t_2)$ denotes the surface of the reference phase front and therefore, t_1 and t_2 denote tangential coordinates on that surface. Absorbing boundary conditions annihilate outward propagating waves up to a certain order. A zeroth-order ($P = 0$) ABC represents the usual Sommerfeld radiation condition. A first-order ABC ($P = 1$) annihilates all fields with up to a u^{-1} dependency while all higher order fields are reflected back into the computational domain. For a cylindrical surface, $u = \sqrt{\rho}$, thus the zeroth-order ABC is simply the geometrical optics spread factor while the first order ABC annihilates fields up to $\mathcal{O}(\rho^{-\infty})$. Evidently, as the ABC order increases, the reflected fields have an increasingly higher attenuation factor and hence the boundary may be placed closer to the geometry without inducing erroneous reflections.

We present the second order conformal ABCs attributed to Chatterjee and Volakis[2]. In particular, the appropriate expressions for a cylindrical-rectangular box boundary will be given.

Absorbing boundary conditions provide a local relationship between the electric field and its curl which may be approximated as

$$\hat{n} \times \nabla \times \vec{E}^s = \bar{\alpha} \cdot \vec{E}_t^s + \bar{\beta} \cdot \nabla \times [\hat{n} (\hat{n} \cdot \nabla \times \vec{E}^s)] + \bar{\gamma} \cdot \nabla_t (\hat{n} \cdot \vec{E}^s) \quad (14)$$

where ∇_t denotes the tangential surface gradient operator. Unfortunately, use of (14) would result in an asymmetric system $[\mathcal{A}^{-1}\mathbb{U}]$ due to the last term which possesses only one differential operator. An asymmetric system requires an iterative solver which utilizes two vector-matrix products such as the conjugate gradient squared (CSG) solver such as the one presented by [5]. A symmetric system requires only one matrix-vector product if the BiCG solver is used. Additionally, for symmetric systems, only the upper or lower triangle of the matrix need be computed and stored.

The gradient in (14) may be approximated by

$$\nabla_t (\nabla \cdot \vec{E}_t^s) = jk_o \nabla_t (\hat{n} \cdot \vec{E}^s) + \mathcal{O}(\lambda^{-\nabla}) \quad (15)$$

With both a gradient and a divergence operator present, one operator can be transferred to the test vector while the other may remain with the source vector. Hence, the resulting matrix *may* be symmetric since both the test and source fields are differentiated. With (15), (14) may be written

$$\hat{n} \times \nabla \times \vec{E}^s = \bar{\alpha} \cdot \vec{E}_t^s + \bar{\beta} \cdot \nabla \times [\hat{n} (\hat{n} \cdot \nabla \times \vec{E}^s)] + \bar{\gamma} \cdot \nabla_t (\nabla \cdot \vec{E}_t^s) \quad (16)$$

For the basis vectors used in [1], $\nabla \cdot \vec{E}_t^s$ is always zero on S^{abc} and hence the third term of (16) will not contribute to this form of the ABC. For surfaces with a common constant curvature for both tangential directions on a surface, this new vector ABC (16) will lead to a symmetric FE system $[\mathcal{A}^{-1}\mathbb{U}]$. However, if the principal curvatures on a surface are unequal, the system will be asymmetric. For either (14) or (16), the three coefficient dyads are given by

$$\begin{aligned} \bar{\alpha} &= \sum_{i=1}^2 \left\{ \frac{\hat{t}_i \hat{t}_i}{D - \Delta\kappa - 2\kappa_i} \left[4\kappa_m^2 - \kappa_g + D(jk_o - \kappa_i) + \kappa_i^2 \right] \right\} \\ \bar{\beta} &= \sum_{i=1}^2 \left\{ \frac{\hat{t}_i \hat{t}_i}{D - \Delta\kappa - 2\kappa_i} \right\} \\ \bar{\gamma} &= \sum_{i=1}^2 \left\{ \frac{1}{(D - \Delta\kappa - 2\kappa_i)} \left[jk_o + 3\kappa_m - \frac{\kappa_g}{\kappa_m} - 2\kappa_i \right] \hat{t}_i \hat{t}_i \right\} \end{aligned} \quad (17)$$

where $\kappa_g = \kappa_1 \kappa_2$, $\Delta\kappa = \kappa_1 - \kappa_2$ and $D = jk_o + 5\kappa_m - \frac{\kappa_g}{\kappa_m}$. In the case of (16), $\bar{\gamma}$ must be divided by jk_o due to (15).

It is advantageous to consider the second-order ABC for singly curved and flat surfaces separately. For a singly curved surface, the unit normal direction and curvature parameters are $\hat{n} = \hat{\rho}$, $\kappa_1 = -\frac{1}{\rho}$ and $\kappa_2 = 0$ as before. After some manipulation, we find that (17) becomes

$$\begin{aligned}\bar{\bar{\alpha}} &= \frac{2\rho}{j2k_o\rho + 1} \left[\frac{2}{\rho^2} + D \left(jk_o + \frac{1}{\rho} \right) \right] \hat{\phi}\hat{\phi} + \frac{2\rho}{j2k_o\rho - 3} \left[\frac{1}{\rho^2} + jk_o D \right] \hat{z}\hat{z} \\ \bar{\bar{\beta}} &= \frac{2\rho}{j2k_o\rho + 1} \hat{\phi}\hat{\phi} + \frac{2\rho}{j2k_o\rho - 3} \hat{z}\hat{z} \\ \bar{\bar{\gamma}} &= [\hat{\phi}\hat{\phi} + \hat{z}\hat{z}]\end{aligned}\tag{18}$$

where $D = jk_o - \frac{5}{2\rho}$. Note that $\bar{\bar{\beta}}$ is not symmetric unless $\rho \rightarrow \infty$

For the second-order ABC, it is advantageous to segment the matrix entry $[\mathcal{A}^{\text{U}}]$ into three parts. After some vector manipulation, these contributions are given by

$$\begin{aligned}I^{(1)abc} &= \int_{S_i^{abc}} \vec{W}_i \cdot [\bar{\bar{\alpha}} \cdot \vec{W}_j] dS \\ I^{(2)abc} &= \int_{S_i^{abc}} [\hat{n} \cdot \nabla \times \vec{W}_i] [\hat{n} \cdot \nabla \times (\bar{\bar{\beta}} \cdot \vec{W}_j)] dS \\ I^{(3)abc} &= \int_{S_i^{abc}} \vec{W}_i \cdot [\bar{\bar{\gamma}} \cdot \nabla_t (\hat{n} \cdot \vec{W}_j)] dS\end{aligned}\tag{19}$$

where $I^{(3)abc}$ is only used for the original, asymmetric ABC (14). Closed form expressions for these three integrals may be readily found by utilizing the vector basis functions given in [1]. As mentioned previously, since the principal radii of curvature are not identical for a cylindrically curved surface, $I^{(2)abc}$ will not be symmetric. However, these terms are asymptotically identical as the radius of the ABC surface becomes large since the surface will then be approximately planar. A symmetric ABC may be obtained by dividing both the numerator and the denominator of $I^{(2)abc}$ by the ABC radius, ρ , which results in a symmetric operator.

4 Radiation Integral

Not surprisingly, since the FE-ABC method is being proposed for modelling more complex geometries than the FE-BI method presented previously by the

authors [1], some support task such as computation of the far-zone radiated fields must become necessarily more complex.

The radiation integral for computing the far-zone radiated fields previously was confined to the surface of the cylinder for uncoated antennas. This field was solely due to radiating magnetic currents in the aperture of the cavity due to the use of a second kind dyadic Green's function (see [1] for details). However, when an overlay or a protruding element is present, the radiation integral must contain such material. Thus, for this work, the radiation integration surface is deformed to contain any material above the cavity. To do so, both electric and magnetic currents over this blister must be used along with both the first and second kind dyadic Green's functions.

5 Results

The aforementioned FE-ABC has been implemented and in this section, it will be used to examine the radiation and input impedance properties of conformal patch antennas with dielectric overlays. However, the formulation's accuracy must first be established via comparison with the FE-BI method presented previously by the authors [1].

Consider a $2\text{ cm} \times 3\text{ cm}$ patch antenna residing atop a $5\text{ cm} \times 6\text{ cm} \times 0.07478\text{ cm}$ dielectric filled cavity. This substrate has a dielectric constant of 2.17 and the cylinder radius is 15.27887 cm. The patch antenna is fed as to excite a pure axial mode ($\phi_s = 0^\circ, z_s = -0.375\text{ cm}$). Figure 2 compares the FE-ABC and FE-BI formulations. In this, data was taken from 3.0 GHz to 3.2 GHz every 5 MHz. The agreement is quite good and we find that the resonant frequency is 3.11 GHz. At this frequency, the H-plane radiation pattern is shown in figure 3.

The previous example involved a single antenna element placed within a discrete cavity with a minimal ABC surface. Since no superstrate was present, the exterior region of the computational domain was limited to the immediate vicinity of the cavity. However, if a dielectric coating is used, a continuous wraparound exterior region is desirable. In this way, the physics involved in substrate mode guided waves is included explicitly in the finite element analysis. The next example utilizes such a computational domain where the exterior region extends a full 360° around the cylinder while its axial length is limited. Furthermore, the discrete cavity which contains the

antenna element is minimized.

To consider the effect of a dielectric overlay, Ke and Wong [6] examined the antenna used by Dahele *et. al.* in [7] which is 3 cm \times 4 cm and fed to excite a pure axial mode ($\phi_s = 0^\circ$, $z_s = 1.0$ cm). The substrate is 0.0795 cm thick with a dielectric constant of 2.32. Figure 4 compares the H-plane pattern of this antenna for uncoated and with a 0.3975 cm dielectric cover which is identical in material parameters with the substrate. In this, each antenna was excited at their resonant frequencies, 3.0 GHz and 2.91 GHz, respectively. Note that, as one might expect, there is no change between the antenna pattern associated with the coated and uncoated antennas. The agreement with the corresponding E-plane pattern is shown in figure 5. However, a slight beam broadening is observed rather than narrowing as predicted by Ke and Wong [6]. The differences may likely be due to the finite cavity aperture in our calculations whereas in [6] the coating and substrate were assumed to cover the entire cylinder. Further communication will be conducted with the authors of [6] to clear up this area of disagreement.

In the previous example, the resonance frequency was seen to shift due to the presence of the dielectric overlay. Such a shift is illustrated in figure 6 which shows the input resistance of a 2 cm \times 3 cm patch antenna (see figure 2) with different overlay thickness. In this example, the substrate and superstrate are identical material ($\epsilon_r = 2.17$).

6 Comments

In this report, we have presented a new application for the FE-ABC method which has been developed at the Radiation Laboratory: radiation analysis of conformal antennas mounted on an infinite cylinder. We have sketched the formulation and presented some initial validation results. Currently, this new FE-ABC formulation has matched data generated by a FE-BI method for uncoated patch antennas. We have presented some preliminary data for patch antennas with dielectric overlays and are currently seeking appropriate measured data. In this report, only axial polarization was considered. Circumferential polarization should also be studied with emphasis on dielectric overlay effects.

Initial results are promising and correspond to expectation. It should be stressed that this new FE-ABC approach is considerably more flexible than

previously developed FE-BI methods since it permits material or protruding elements in the exterior region of the cylinder. We will explore the utility of this approach for inhomogeneous coatings, complex protruding antennas, etc. in future reports.

References

- [1] L.C. Kempel and J.L. Volakis, "A finite element-boundary integral method for cavities in a circular cylinder," *1993 IEEE Antennas and Propagat. Soc. Int. Symp.*, Vol. 1, pp. 292-295, June 1993.
- [2] A. Chatterjee and J.L. Volakis, "Conformal absorbing boundary conditions for the vector wave equation," *Microwave Opt. Technol. Lett.*, Vol. 6, pp. 886-889, Dec. 1993.
- [3] A.F. Peterson, "Absorbing boundary conditions for the vector wave equation," *Microwave Opt. Technol. Lett.*, Vol. 1, pp. 62-64, April 1988.
- [4] J.P. Webb and V.N. Kanellopoulos, "Absorbing boundary conditions for finite element solution of the vector wave equation," *Microwave Opt. Technol. Lett.*, Vol. 2, pp. 370-372, Oct. 1989.
- [5] H.A. van der Vorst, "BI-CGSTAB: A fast and smoothly converging variant of BI-CG for the solution of nonsymmetric linear systems," *SIAM J. Sci. Stat. Comput.*, Vol. 13, No. 2, pp. 631-644, Mar. 1992.
- [6] S-Y Ke and K-L Wong, "Full wave analysis of probe-fed superstrate-loaded rectangular microstrip antennas on a cylindrical body," *1994 IEEE Antennas and Propagat. Soc. Int. Symp.*, Vol. 3, pp. 2224-2227, June 1994.
- [7] J.S. Dabele, R.J. Mitchell, K.M. Luk and K.F. Lee, "Effect of curvature on characteristics of rectangular patch antenna," *Electronics Letters*, Vol. 23, No. 14, pp. 748-749, 1987.

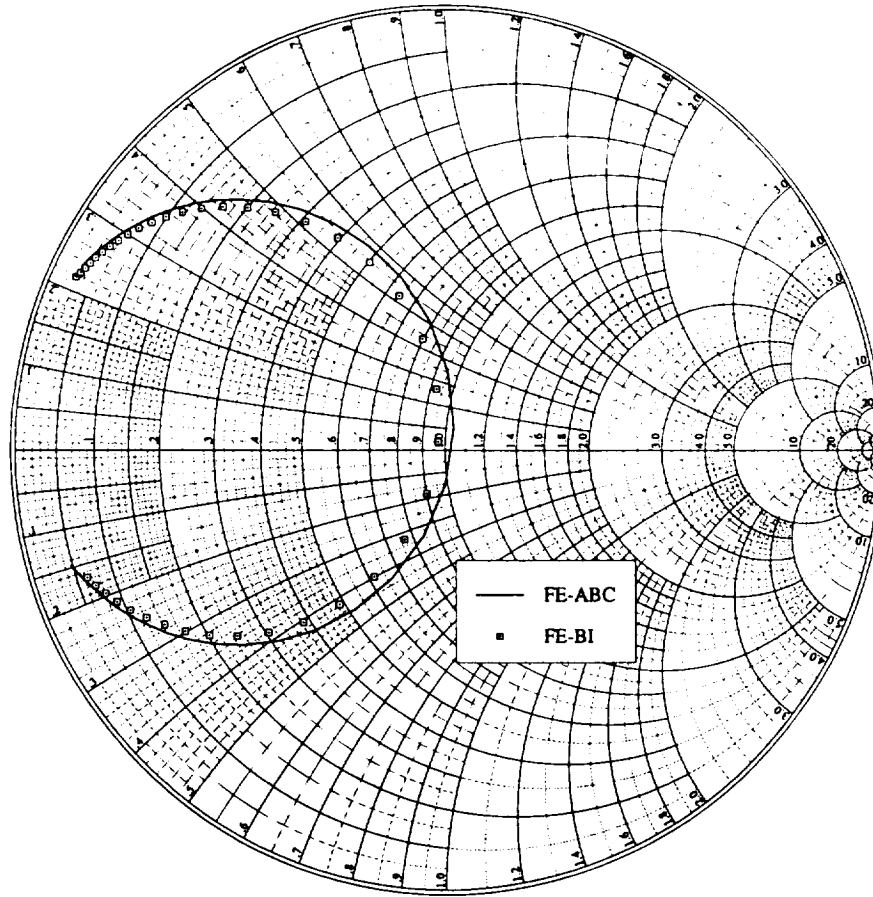


Figure 2: Input impedance for the axially polarized patch antenna which is $2\text{ cm} \times 3\text{ cm}$ in a $5\text{ cm} \times 6\text{ cm} \times 0.07874\text{ cm}$ cavity. The frequency range is 3.0 to 3.2 GHz with data taken every 5 MHz.

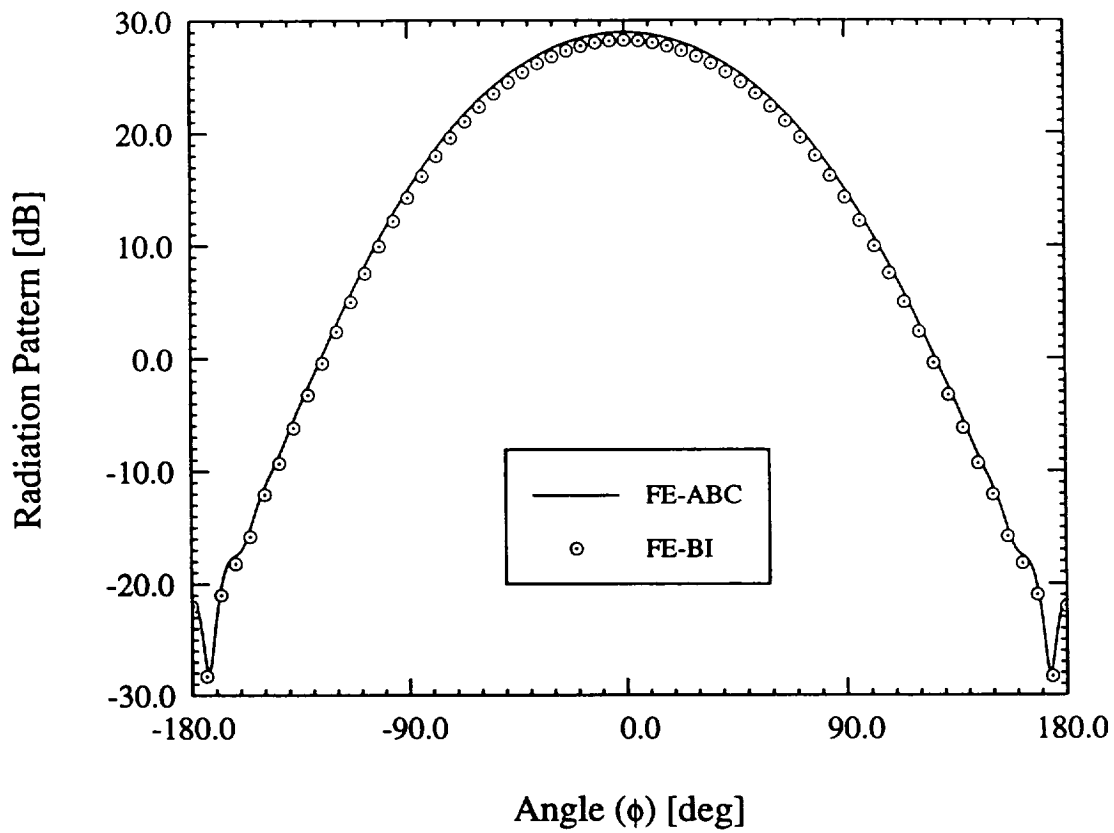


Figure 3: Radiation pattern for a patch antenna which is 2 cm × 3 cm in a 5 cm × 6 cm × 0.07874 cm cavity operated at 3.11 GHz.

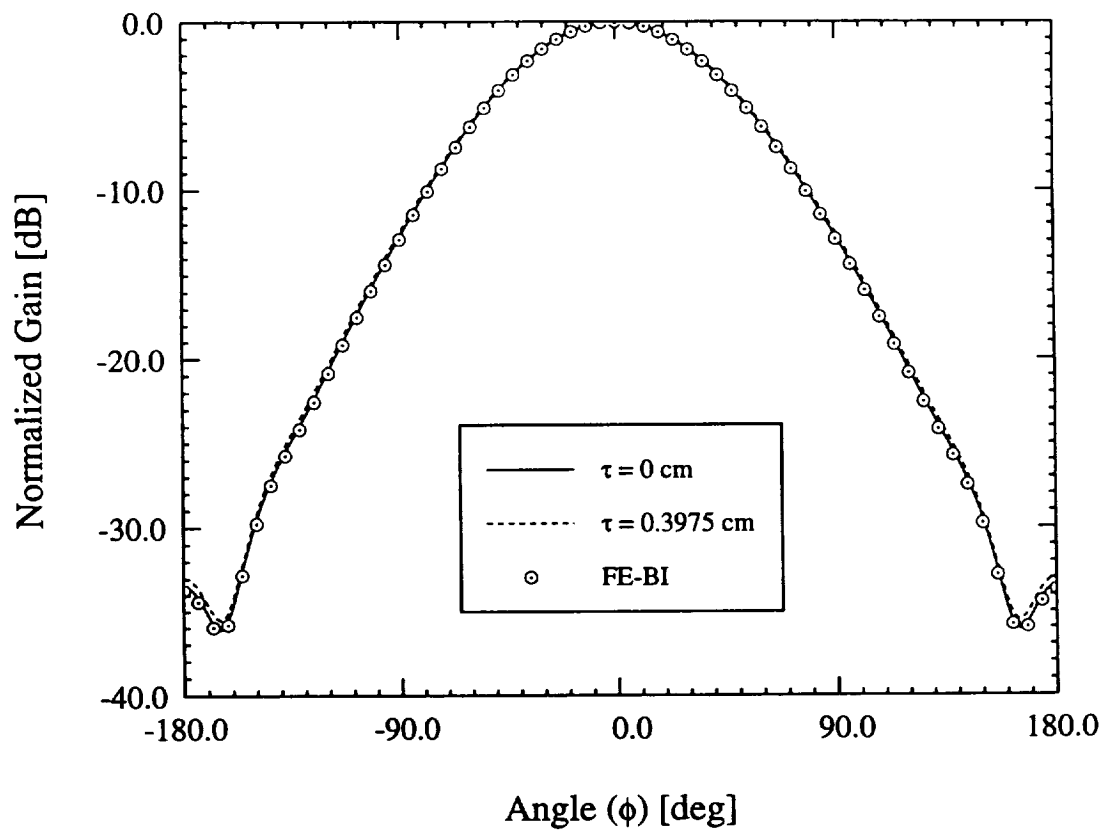


Figure 4: H-plane radiation pattern for a patch antenna which is $4 \text{ cm} \times 3 \text{ cm}$ in a $8 \text{ cm} \times 6 \text{ cm} \times 0.0795 \text{ cm}$ cavity with different overlay thickness. The dielectric constant of the overlay and the substrate is 2.32 and the feed point is ($\phi_s = 0^\circ, z_s = 1.0 \text{ cm}$).

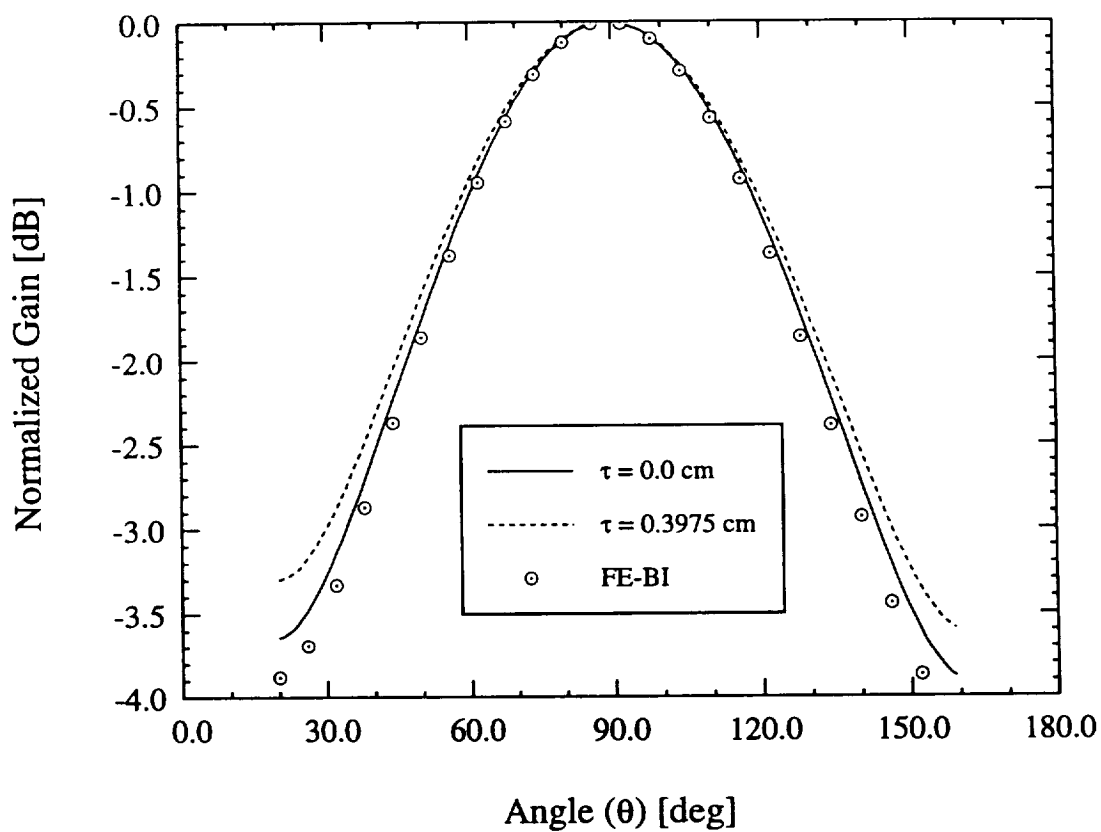


Figure 5: E-plane radiation pattern for a patch antenna which is 4 cm × 3 cm in a 8 cm × 6 cm × 0.0795 cm cavity with different overlay thickness. The dielectric constant of the overlay and the substrate is 2.32 and the feed point is ($\phi_s = 0^\circ$, $z_s = 1.0$ cm).

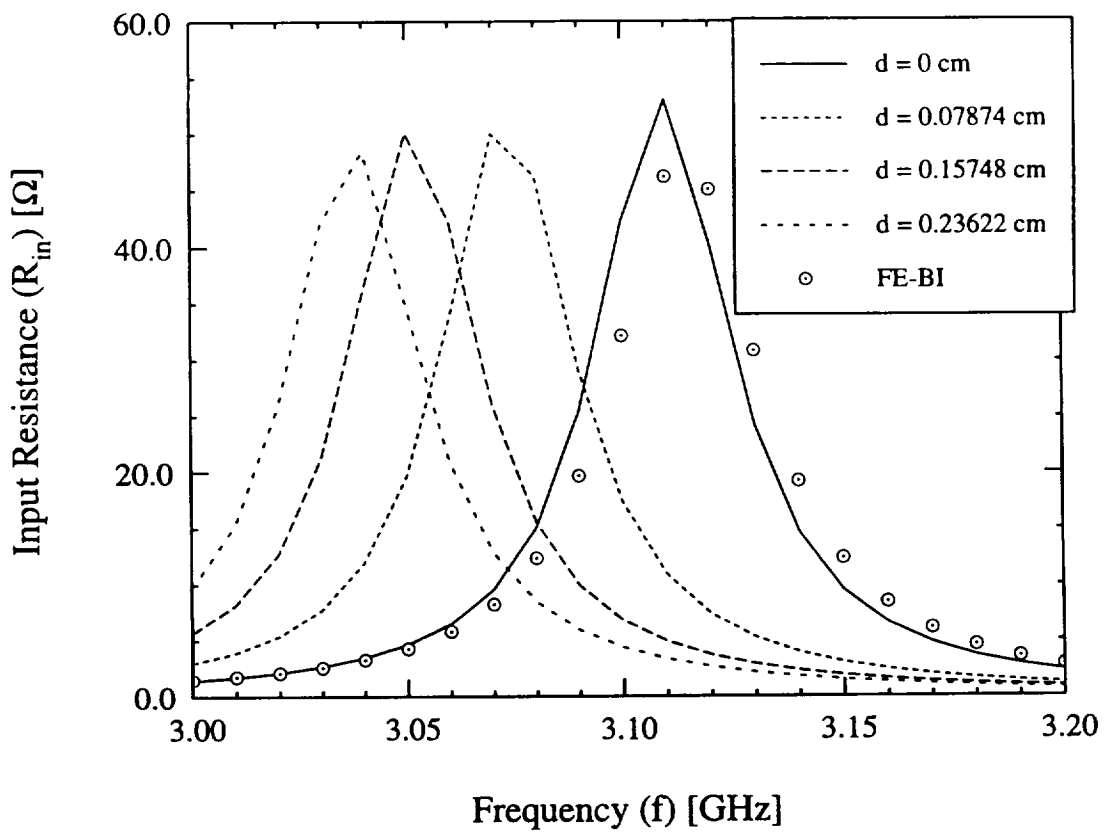


Figure 6: Input resistance for a patch antenna which is $2 \text{ cm} \times 3 \text{ cm}$ in a $5 \text{ cm} \times 6 \text{ cm} \times 0.07874 \text{ cm}$ cavity with different overlay thickness. The dielectric constant of the overlay and the substrate is 2.17 and the feed point is $(\phi_s = 0^\circ, z_s = -0.375 \text{ cm})$.

Radiation by Cavity-backed Antennas on a Circular Cylinder

Leo C. Kempel, John L. Volakis

Radiation Laboratory

University of Michigan

1301 Beal Ave.

Ann Arbor, MI 48109-2122

and

Randall J. Sliva

Naval Air Warfare Center

China Lake, CA 93555-6001

June 14, 1994

Abstract

Conformal antenna arrays are popular for deployment on curved aircraft, spacecraft and land vehicle platforms due to their inherent low weight, cost and drag properties. However, to date there has been a dearth of rigorous analytical and numerical solutions to aid the designer. In fact, it has been common practice to use limited measurements and planar approximations in designing such non-planar antennas. In this paper, we extend the finite element-boundary integral method to radiation by cavity-backed structures recessed in an infinite, metallic cylinder. The accuracy of the developed FE-BI code for a microstrip patch arrays is established by comparison with measurements. The formulation is then used to investigate the effect that the finite aperture has on the radiation pattern. In addition, the effect of curvature on resonant frequency, gain, input impedance and pattern shape is examined.

1 Introduction

Modern aircraft and missile designs seek to utilize conformal antenna arrays rather than conventional protruding antennas due to their low weight, low drag, low cost and flexibility. Although most useful aircraft surfaces possess some curvature, the vast majority of available design information assumes planar elements. Indeed, the literature is rich with approximate [1], numerical [2] and experimental [3] design and characterization data for planar structures. The most common antenna element is a microstrip patch printed on a dielectric coated groundplane. Dielectric coated cylinders have also been investigated using approximate [4] and numerical [5] approaches.

Often, it is desirable to enclose each radiating element within a metallic cavity to suppress parasitic substrate coupling [6]. Approximate methods, such as the cavity model [1], do not include finite aperture effects since the radiating currents are restricted to the immediate vicinity of the patch. Most integral equation formulations such as the one proposed by Pozar and Voda [2] utilize a grounded slab Green's function in their construction which precludes practical finite aperture simulations. Recently, Aberle [6] proposed an integral equation formulation which partitions the geometry into an exterior half space and an interior homogeneously filled cavity. This approach determines the electric field attributed to the patch and feed currents and the two regions are coupled by enforcing field continuity across the finite aperture. Unfortunately, as with all integral formulations, the linear system requires $\mathcal{O}(N^2)$ storage and considerable computational effort due the fully populated system and the slowly converging cavity Green's function. The simulation of large finite cavity-backed arrays using such an approach is therefore not practical.

An alternative formulation, utilizing the Finite Element-Boundary Integral (FE-BI) method, was proposed by Jin and Volakis [7]. This approach is also suitable for inhomogeneously filled cavity-backed antennas recessed in a metallic ground plane. As with all partial differential equation formulations, this approach is associated with a highly sparse system which requires only $\mathcal{O}(N)$ storage. Additionally, when coupled with a Conjugate or Biconjugate Gradient-Fast Fourier Transform (BiCG-FFT) solver, the computational burden is significantly reduced. The FE-BI method has been successfully used for scattering and antenna performance analysis involving planar platforms.

A similar FE-BI method was proposed by the authors [8] for scattering

by cylindrical-rectangular and wraparound patch antennas. New divergence free, high fidelity edge-based elements were presented along with an efficient solution strategy which exploited an asymptotic evaluation of the appropriate dyadic Green's function as well as a BiCG-FFT solver. The resulting computer code was shown to accurately compute the scattering by both planar and highly curved elements. This paper investigates the accuracy and utility of such a FE-BI formulation for antenna performance analysis. The radiation pattern of a single element as well as that of a wraparound array is compared with measured results. The importance of modelling finite apertures is examined and in addition, the effect that curvature has on the resonant frequency, gain, driving point impedance and pattern shape is quantified.

2 Formulation

In this section, the FE-BI formulation appropriate for radiation analysis is developed for cavity-backed antennas recessed in an infinite metallic cylinder (see figure 1). As usual, the finite element formulation permits substantial modeling flexibility, including cavity inhomogeneities, lumped loads and microstrip feeding lines.

The FE-BI formulation begins with the weak form of the vector wave equation followed by specification of appropriate vector shape functions and dyadic Green's function. The resulting FE-BI equations are then used to solve for the total electric fields within the cavity and on the aperture (for further details, see Volakis *et al.* [9]). The weak form of the wave equation can be written as

$$\begin{aligned} \sum_j E_j \left\{ \int_{V_i} \left[\frac{\nabla \times \vec{W}_j(\rho, \phi, z) \cdot \nabla \times \vec{W}_i(\rho, \phi, z)}{\mu_r(\rho, \phi, z)} \right. \right. \\ \left. \left. - k_o^2 \epsilon_r(\rho, \phi, z) \vec{W}_j(\rho, \phi, z) \cdot \vec{W}_i(\rho, \phi, z) \right] \rho d\rho d\phi dz \right. \\ \left. + (k_o a)^2 \delta_a(j) \delta_a(i) \int_{S_i} \int_{S_j} \left[\vec{W}_i(a, \phi, z) \cdot \hat{\rho}(a, \phi, z) \times \right. \right. \\ \left. \left. \overline{\overline{G}}_{e2}(a, \bar{\phi}, \bar{z}) \times \hat{\rho}(a, \phi', z') \cdot \vec{W}_j(a, \phi', z') \right] d\phi' dz' d\phi dz \right\} = f_i^{int} \quad (1) \end{aligned}$$

In this, \vec{W}_i are vector basis functions with support limited to the finite el-

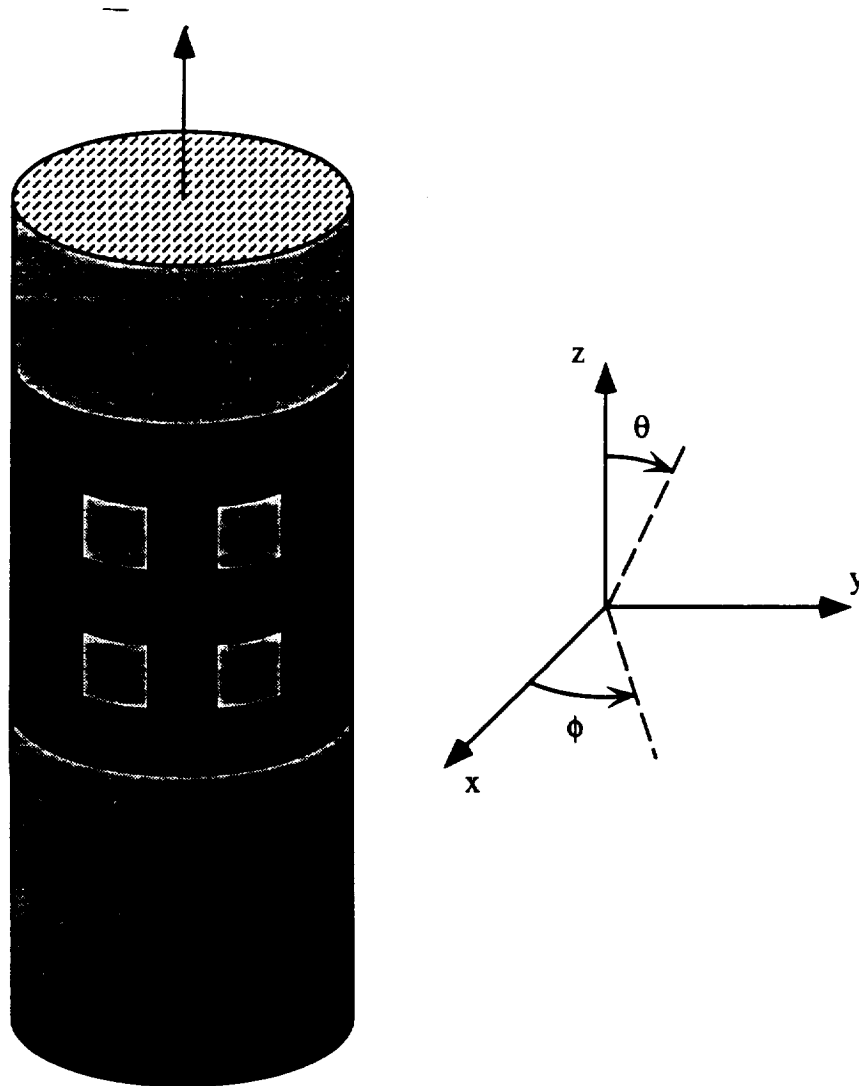


Figure 1: Illustration of a typical cavity-backed antenna situated on a metallic cylinder and the associated coordinate system.

element volume V_i which is associated with the i^{th} degree of freedom, and in a similar fashion. S_i and S_j represent aperture surfaces associated with the i^{th} and j^{th} degrees of freedom, respectively. The appropriate dyadic Green's function is denoted by $\overline{\overline{G}}_{e2}$ and it has convolutional ($\bar{\phi} = \phi - \phi'$, $\bar{z} = z - z'$) form when evaluated on the surface of the cylinder, $\rho = a$. The unprimed coordinates represent the test point while the primed ones denote the source point and (ρ, ϕ, z) are the usual cylindrical coordinates. The free-space propagation constant is given by $k_0 = \frac{2\pi}{\lambda_0}$, where λ_0 is the free-space wavelength. The cavity is filled with an inhomogeneous material having relative constitutive properties ϵ_r and μ_r . The function $\delta_a(i)\delta_a(j)$ identifies when both the source and test unknowns belong to the aperture and accordingly contribute to the boundary integral sub-matrix. The FE-BI equation (1) may be rewritten in matrix form as

$$[\mathcal{A}] \begin{Bmatrix} E_j^{ap} \\ E_j^{int} \end{Bmatrix} + \begin{bmatrix} [\mathcal{G}] & [0] \\ [0] & [0] \end{bmatrix} \begin{Bmatrix} E_j^{ap} \\ E_j^{int} \end{Bmatrix} = \begin{Bmatrix} 0 \\ f_i^{int} \end{Bmatrix} \quad (2)$$

where the entries of $[\mathcal{A}]$ are due to the FE portion of the formulation and $[\mathcal{G}]$ is the boundary integral sub-matrix. In (2), E_j^{ap} and E_j^{int} denote degrees of freedom associated with the aperture and interior fields, respectively. In (2), f_i^{int} represents the internal excitation and for this paper, a radially oriented probe feed is considered.

The vector elements, dyadic Green's function evaluation, matrices $[\mathcal{A}]$ and $[\mathcal{G}]$ and the far-zone field formulae are given in [8] and are therefore not repeated here. The interior source function is given by

$$f_i^{int} = - \int_{V_i} \left\{ \nabla \times \left[\frac{\vec{M}^{int}(\rho, \phi, z)}{\mu_r(\rho, \phi, z)} \right] + jk_0 Z_0 \vec{J}^{int}(\rho, \phi, z) \right\} \cdot \vec{W}_i(\rho, \phi, z) \rho d\rho d\phi dz \quad (3)$$

where \vec{J}^{int} and \vec{M}^{int} are the impressed electric or magnetic current densities. For a radially ($\hat{\rho}$) directed probe feed, the impressed current located at (ϕ_s, z_s) is given by

$$\vec{J}^{int} = \hat{\rho} I_0 \frac{\delta(\phi - \phi_s)(z - z_s)}{\rho} \quad (4)$$

and (3) becomes

$$f_i^{int} = -jk_o Z_o I_o \frac{\tilde{s}_i \rho_b}{\alpha_i h_i} \ln \left(\frac{\rho_b}{\rho_a} \right) [(\phi_s - \phi_i)(z_s - z_i)] \quad (5)$$

if the edge-based elements introduced in [8] are used.

Having computed the finite element and boundary integral matrices as well as the internal excitation, the BiCG method is used to solve for the unknown electric fields throughout the computation domain. Given that the FE matrix is highly sparse and symmetric, the BiCG method is a well-suited choice among iterative solvers. It is also important to note that the matrix-vector product associated with the boundary integral can be performed using FFTs resulting in a reduced storage and computational burden. The computed electric field within and on the aperture of the cavity may now be used to compute antenna parameters such as the gain and the input impedance.

The radiated magnetic field is computed by integrating the aperture fields with the far-zone dyadic Green's function given in [8]

$$\vec{H}^r(r, \theta, \phi) = jY_o k_o a \int_S \vec{\vec{G}}_{e2}(r, \theta, \phi; a, \phi', z') \cdot [\hat{\rho}(a, \phi', z') \times \vec{E}(a, \phi', z')] d\phi' dz' \quad (6)$$

where (r, θ, ϕ) indicates the observation point in spherical coordinates. The far-zone electric field may be obtained from (6) in the usual manner. The radiation pattern, directive gain and other useful antenna parameters may be calculated using (6). For example, the antenna gain may be computed from the far-zone electric field as

$$G_{dB}(\theta, \phi) = 10 \log_{10} [4\pi |E^r(\theta, \phi)|^2] + 10 \log_{10} \left[\frac{1}{Z_o R_{in}} \right] \quad (7)$$

where R_{in} is the input resistance which is given below and E^r is the radiated electric field as $r \rightarrow \infty$.

In addition to the antenna gain, designers are concerned with the input impedance of an antenna for feed line matching purposes. The input impedance is comprised of two contributions [10]

$$Z_{in} = Z_P + Z_D \quad (8)$$

where the first term is the probe's self-impedance and the second term is the contribution due to the presence of the patch. The probe self-impedance accounts for the finite radius of the probe and hence can be omitted when a zero-thickness probe is assumed. Accordingly, the driving point impedance may be found by calculating the voltage between the patch and the cavity base

$$Z_{in} = Z_D = -\frac{1}{I_o^2} \int_V \vec{E}(\rho, \phi, z) \cdot \vec{J}^{int}(\rho, \phi, z) \rho d\rho d\phi dz \quad (9)$$

where the impressed current is given by (4), V_i refers to the volume of the finite element which contains the probe-feed, $\vec{E}(\rho, \phi, z)$ is the interior field and I_o is the constant current impressed upon the probe. Substituting (4) into (9), for the cylindrical edge elements presented in [8], it follows that the input impedance is given by

$$Z_{in} = \sum_{i=1}^4 Z_{in}^i \quad (10)$$

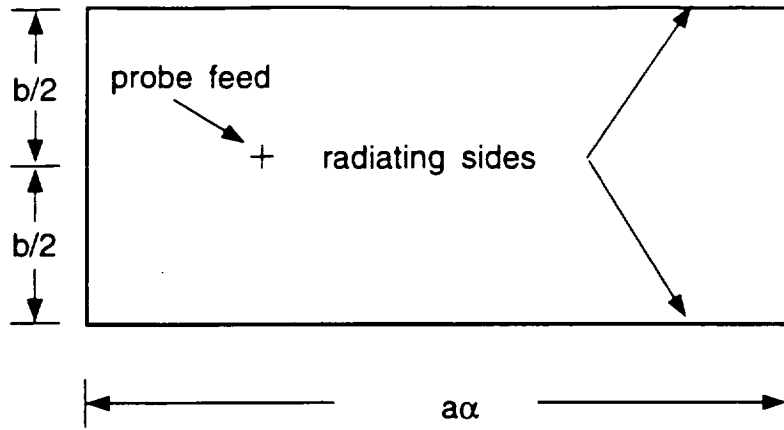
where

$$Z_{in}^i = -\frac{E(i)}{I_o} \frac{\tilde{s}_i \rho_b^i}{\alpha_i h_i} \ln \left(\frac{\rho_b}{\rho_a} \right) [(\phi_s - \tilde{\phi}_i)(z_s - \tilde{z}_i)] \quad (11)$$

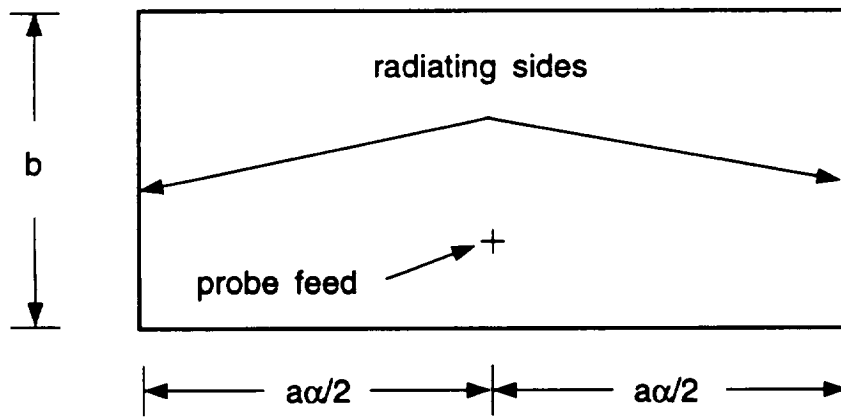
is the contribution due to one of the four radial edges of the element containing the probe.

3 Results

Two types of antenna elements are considered in this paper and they are shown in figure 2 where each patch is $a\alpha^\circ \times b$ in size with a denoting the radius of the cylinder. Although the FE-BI method permits mixed-mode feeding, for this paper it is convenient to consider only the two lowest order non-hybrid modes. A patch whose radiating side walls are axially oriented is termed an axially polarized patch and is fed at $\phi_s = \frac{\alpha}{2}$. Circumferentially (or azimuthally) polarized patches have radiating walls forming constant z -surfaces and are typically fed at $z_s = \frac{b}{2}$. The $\theta = 90^\circ$ cut is the E-plane for circumferentially polarized patches and the H-plane for axially polarized



(a)



(b)

Figure 2: Illustration of (a) a circumferentially polarized patch element; and (b) an axially polarized patch element. The radius of the cylinder is denoted by a .

elements. Observation is considered in the $\theta = 90^\circ$ cut/plane since creeping wave effects are a primary interest of this paper.

Several computed and measured antenna patterns have been published for patches printed on a coated cylinder. One such patch, which is $3.5 \text{ cm} \times 3.5 \text{ cm}$, was used by Sohtell [11] to compare the accuracy of the cavity model [4] to a surface current integral equation [5]. The measured data was taken at 2.615 GHz for a metallic cylinder which was 63.5 cm long and had a radius of 14.95 cm. The cylinder was coated with a 0.3175 cm uniform dielectric having relative permittivity of $\epsilon_r = 2.32$. Data was taken for $-180^\circ \leq \phi \leq 180^\circ$ in the $\theta = 90^\circ$ plane. Figure 3 compares these measured patterns with data generated using the FE-BI method for an identical patch placed within a $360^\circ \times 7 \text{ cm}$ cavity. This wraparound cavity was chosen to simulate the coated physical test body. Note that the H-plane patterns are symmetric due to the symmetric placement of the feed, whereas the E-plane patterns are not symmetric. The placement of the feed was not specified in [11]; however, the agreement for the E-plane pattern shown in figure 3 indicates that the position used in the FE-BI model ($a\phi_s = -1 \text{ cm}$) is reasonable. The feed was placed at $z_s = -1 \text{ cm}$ for the axially polarized (H-plane) case.

We next consider patch arrays. Being a rigorous method, the FE-BI formulation accounts for mutual coupling and cavity termination effects. The H-plane pattern of a four element array was measured to gauge the accuracy of the FE-BI approach. Each element is $2 \text{ cm} \times 3 \text{ cm}$ and placed within a $5 \text{ cm} \times 6 \text{ cm} \times 0.07874 \text{ cm}$ cavity which is filled with a dielectric having $\epsilon_r = 2.17$. The cylinder is 91.44 cm long and has a radius of 15.24 cm. The cavities are placed symmetrically around the cylinder (e.g. a patch is centered at $0^\circ, 90^\circ, 180^\circ$ and 270°). Only the patch centered at 0° was excited while the remaining patches were terminated with a 50Ω load. The driven patch was axially polarized and the feed was located at $z_s = -0.375 \text{ cm}$. Figure 4 illustrates the excellent agreement between the FE-BI formulation and the measured data.

In a previous paper [8], discrete wraparound cavity arrays were found to have a significantly lower radar cross section (RCS) compared to a continuous wraparound cavity array. Thus, the size of the cavity had a significant effect on the scattering properties of the array. The two antennas presented by Sohtell [11] were placed within individual cavities which were 7 cm high and approximately $30^\circ, 50^\circ, 90^\circ, 180^\circ, 270^\circ$ or 360° in angular extent. Figure 5 illustrates that the azimuthal cavity size has little effect on the radiation

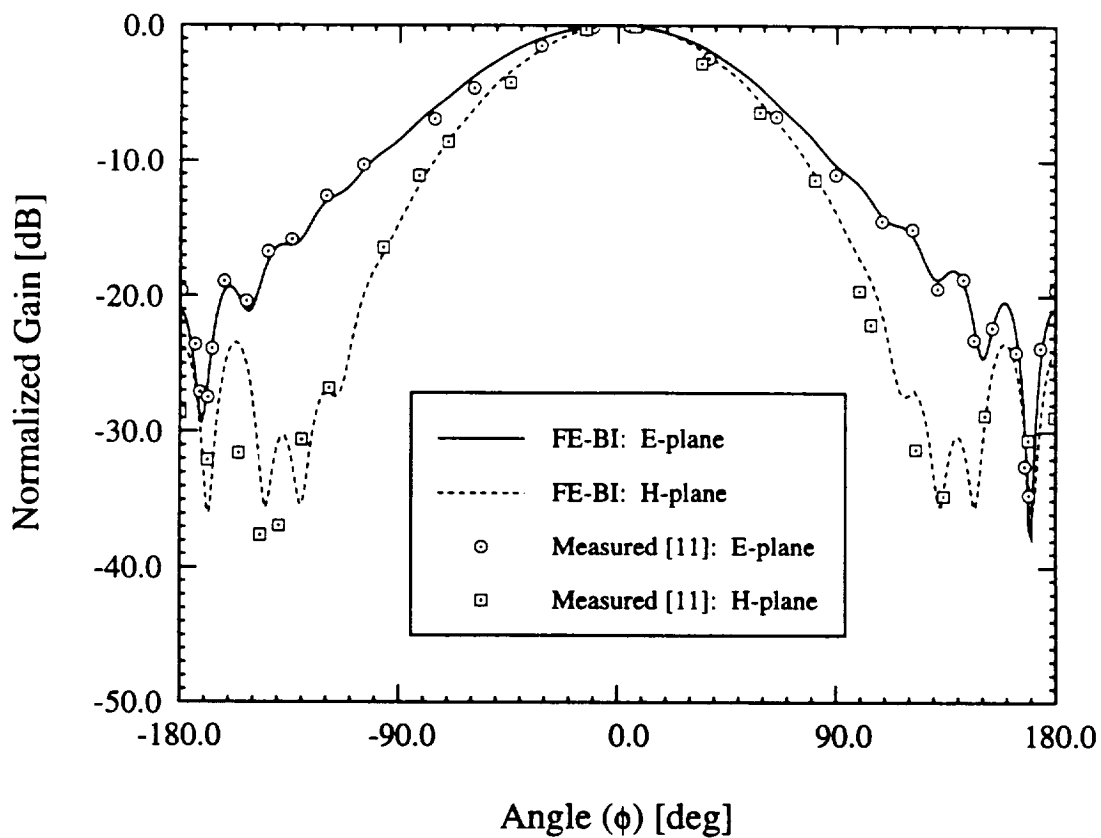


Figure 3: Comparison of measured and computed data for a circumferentially polarized element (E-plane) and an axially polarized element (H-plane). The antenna ($3.5 \text{ cm} \times 3.5 \text{ cm}$) was printed on a 14.95 cm cylinder with a 0.3175 cm coating ($\epsilon_r = 2.32$). The probe feed was placed at $(a\phi_s, z_s) = (-1.0, 0.0)$ for the circumferentially polarized patch and at $(a\phi_s, z_s) = (0.0, -1.0)$ for the axially polarized antenna.

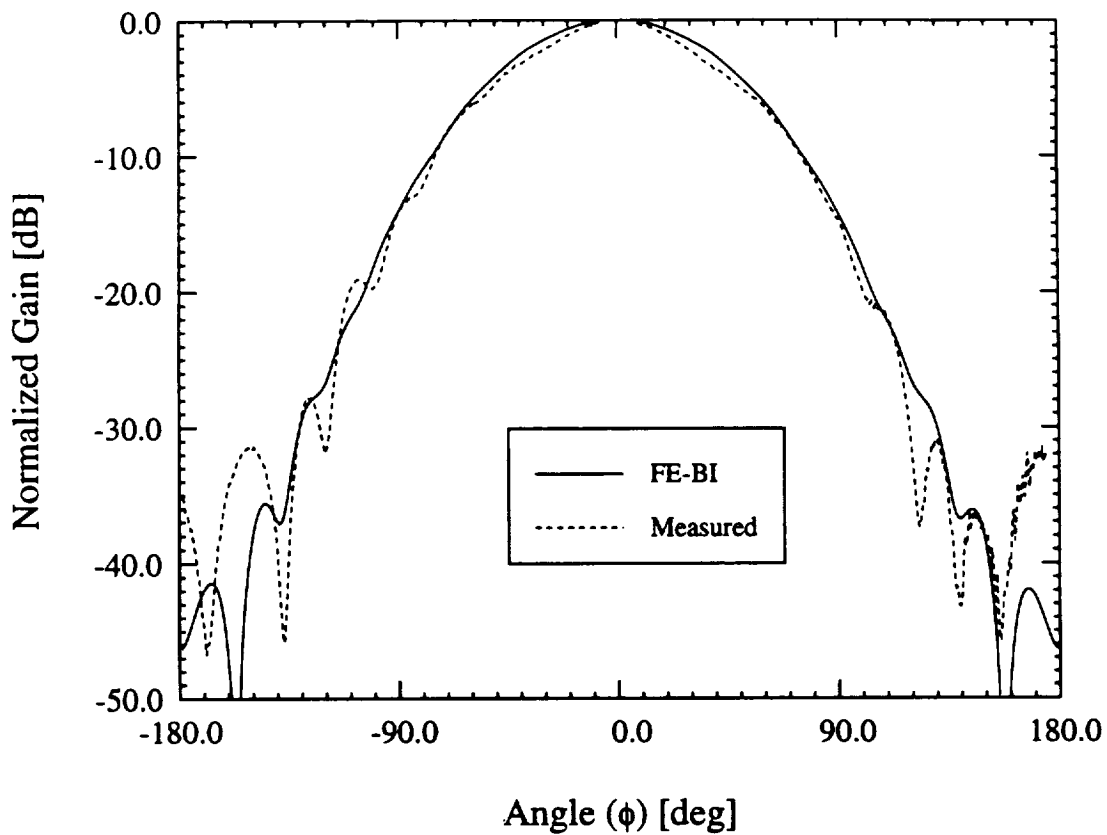


Figure 4: H-plane pattern for a four element patch array. Each patch is $2 \text{ cm} \times 3 \text{ cm}$ and the patches are placed symmetrically around the cylinder. Only the patch centered at 0° is fed while the other patches are terminated with 50Ω loads.

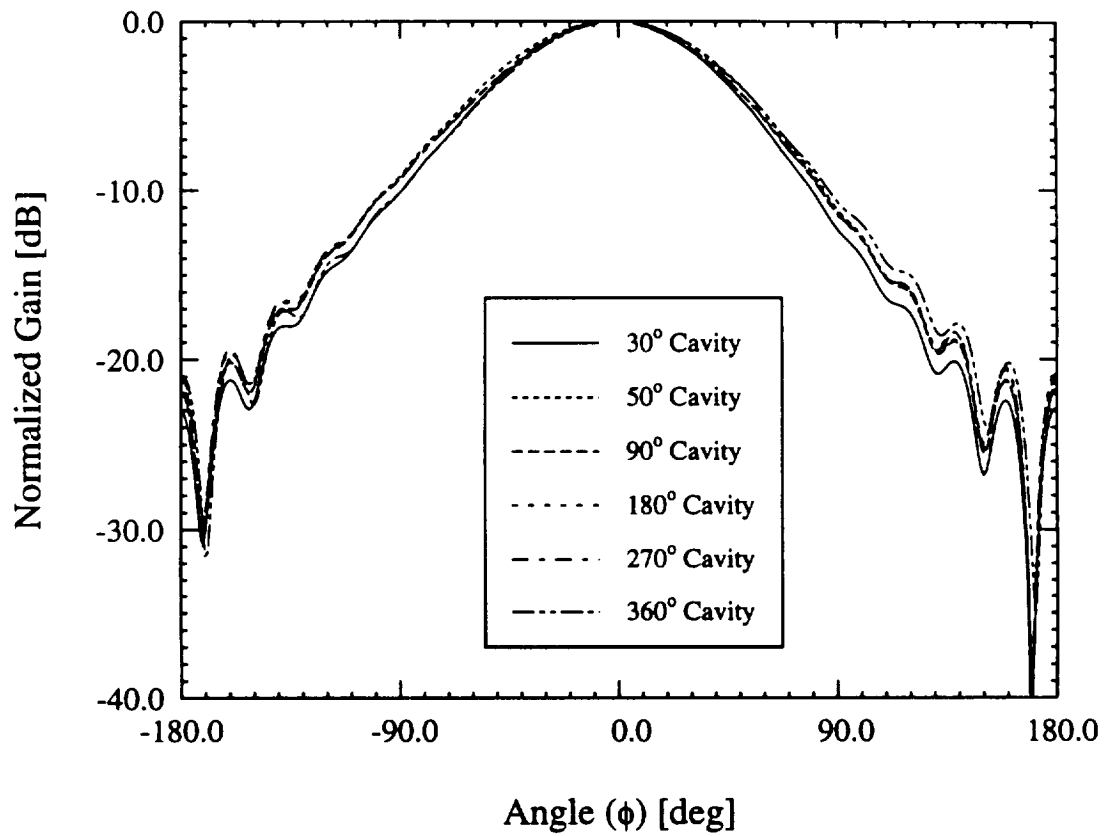


Figure 5: Effect of cavity size on the E-plane radiation pattern of a circumferentially polarized patch antenna.

pattern for a circumferentially polarized element and a similar comparison for the axially polarized patch is shown in figure 6. The back lobe of the antenna (near $\phi = 180^\circ$) is very small for cavities less than 180° but increases for larger cavities. For cavities which lie solely on the forward face of the cylinder, the substrate modes apparently diffract off the cavity walls; an effect which has little influence on the main lobe of the pattern. However, for wraparound cavities and cavities which extend into the back side of the cylinder, the substrate modes either shed like creeping waves or diffract strongly behind the cylinder thus giving rise to the back lobe.

Having examined the effect of cavity size on the radiation patterns, we will now look at the effect of curvature on the gain of patch antennas on cylindrical platforms near resonance. Each of the two antennas used above were separately placed within $10.5 \text{ cm} \times 10.5 \text{ cm}$ cavities which were embedded in cylinders with increasing radius. The frequency was allowed to vary from 2.4 GHz to 2.7 GHz and the gain (7) was recorded every 5 MHz. Figure 7 illustrates that the gain decreases with increasing element curvature for a circumferentially polarized patch. Since the input impedance is only slightly affected by curvature as shown in figure 8 the resulting decrease in gain implies a decreased radiated power which is expected since the effective aperture area observed normal to the patch is reduced as the curvature increases. The axially polarized patch exhibits a greater decrease in gain with increasing curvature as shown in figure 9. For this polarization, the input impedance is affected by curvature as shown in figure 10. The enhanced sensitivity of the axially polarized antenna is due to the combined effects of a decreased radiated power and driving point impedance. Both antennas exhibit a small decrease in resonant frequency (less than 1.5 percent) with increasing curvature as illustrated by the rotation of the curves in figures 8 and 10.

The radiation pattern of a circumferentially polarized antenna at resonance exhibits reduced creeping wave interactions with decreasing curvature due to attenuation as shown in figure 11 when excited at a resonant frequency. For circumferentially polarized E-plane observation, the radiating surface fields are aligned along the $\hat{\phi}$ -axis which results in little pattern broadening. The radiation pattern of the axially polarized antenna broadens as the curvature increases which is illustrated in figure 12. Since the radiating aperture fields are aligned along the \hat{z} -axis for axially polarized H-plane observation, the pattern exhibits broadening due to the orientation of the

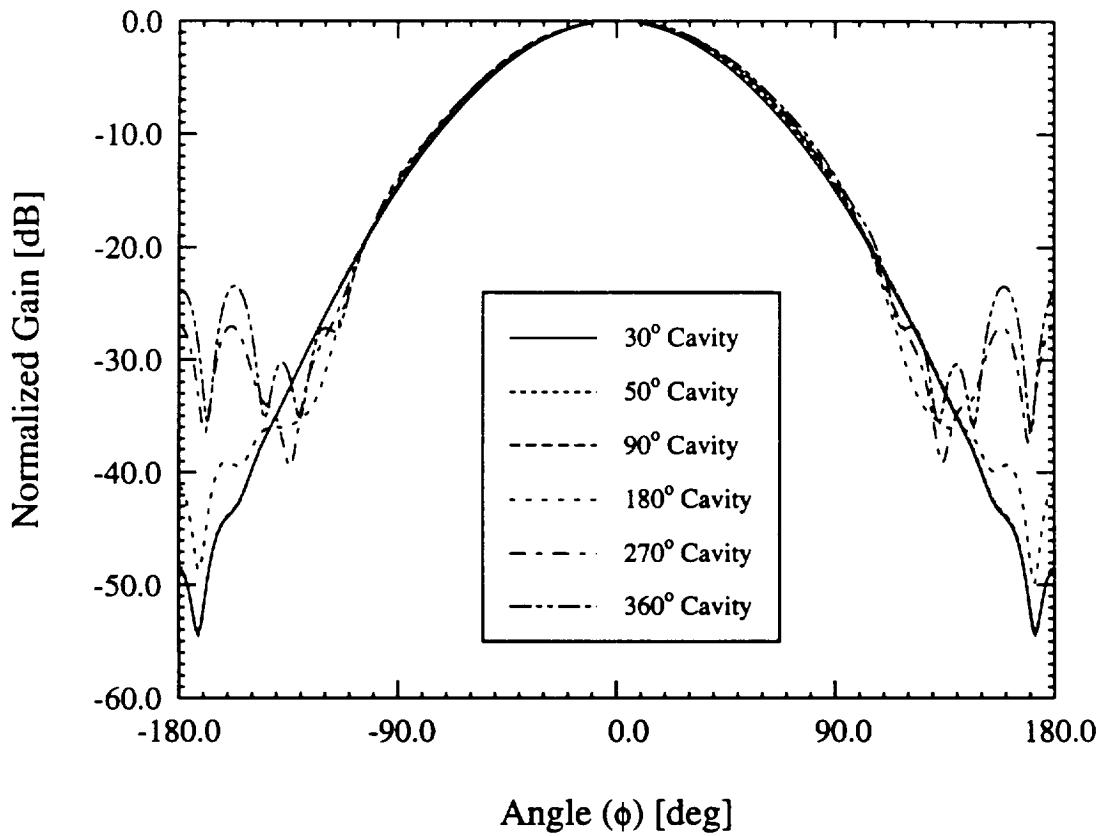


Figure 6: Effect of cavity size on the H-plane radiation pattern of an axially polarized patch antenna.

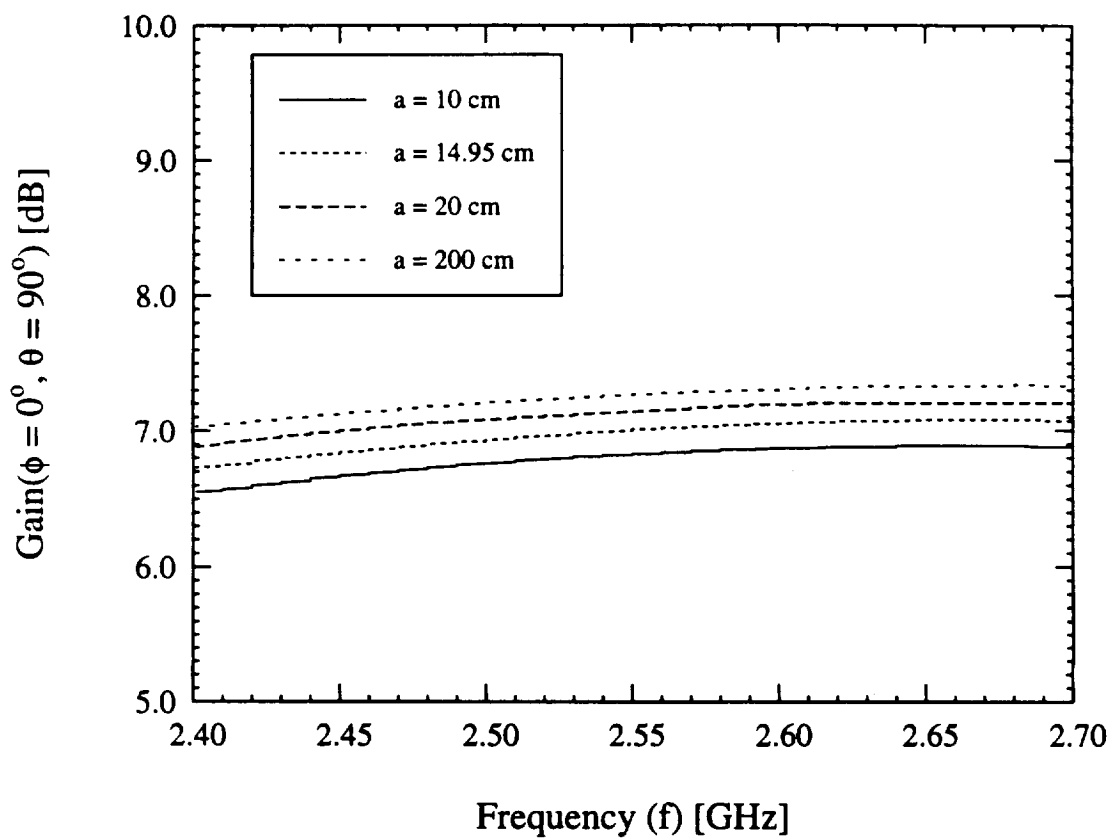


Figure 7: Gain (7) of a circumferentially polarized patch antenna near resonance for various cylinder radii.

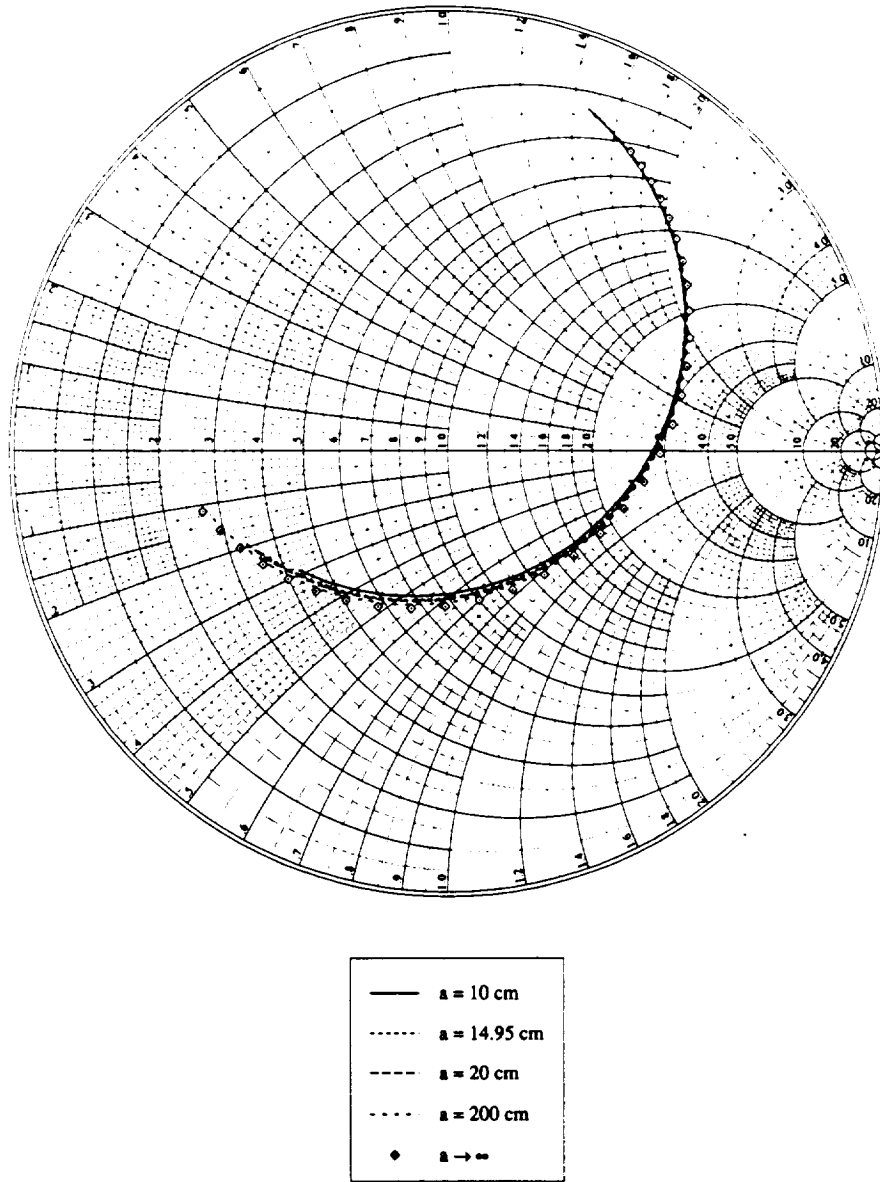


Figure 8: Input impedance of a circumferentially polarized patch antenna for various cylinder radii. The frequency range was 2.4 GHz to 2.7 GHz and the cavity size was 10.5 cm \times 10.5 cm.

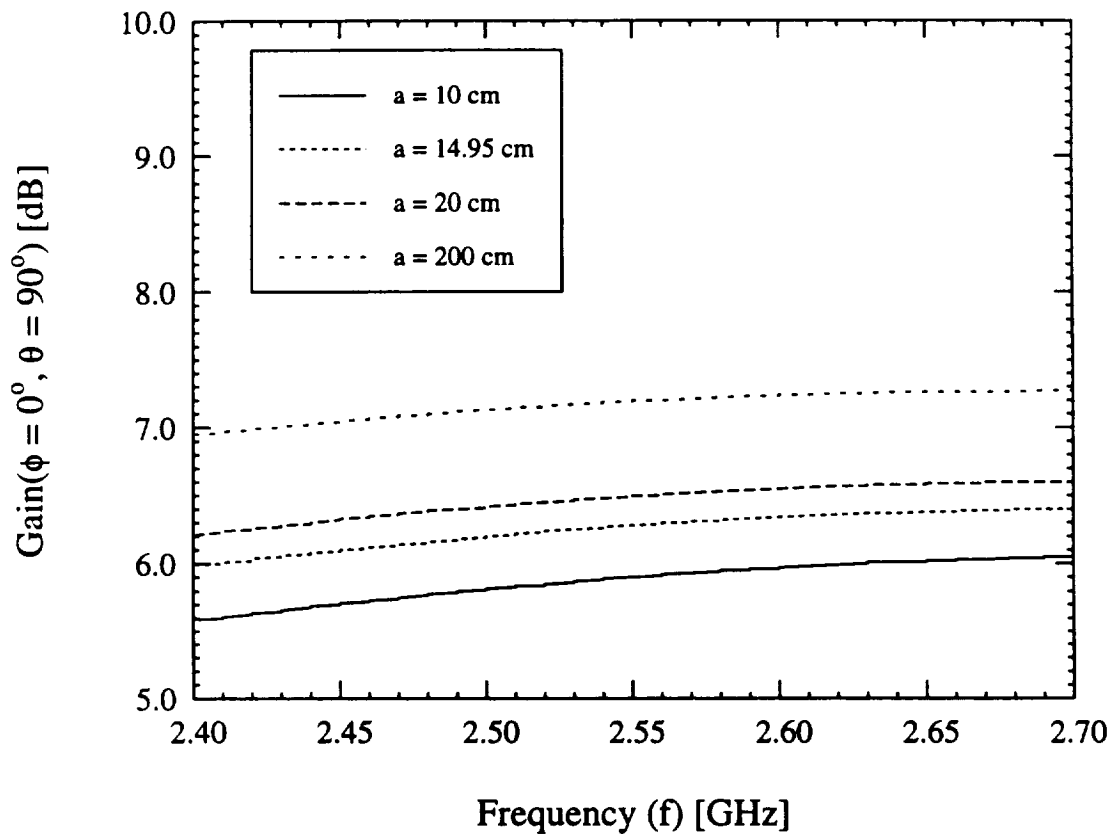


Figure 9: Gain (7) of an axially polarized patch antenna near resonance for various cylinder radii.

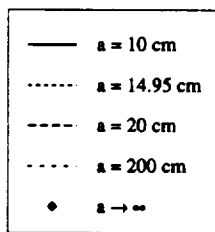
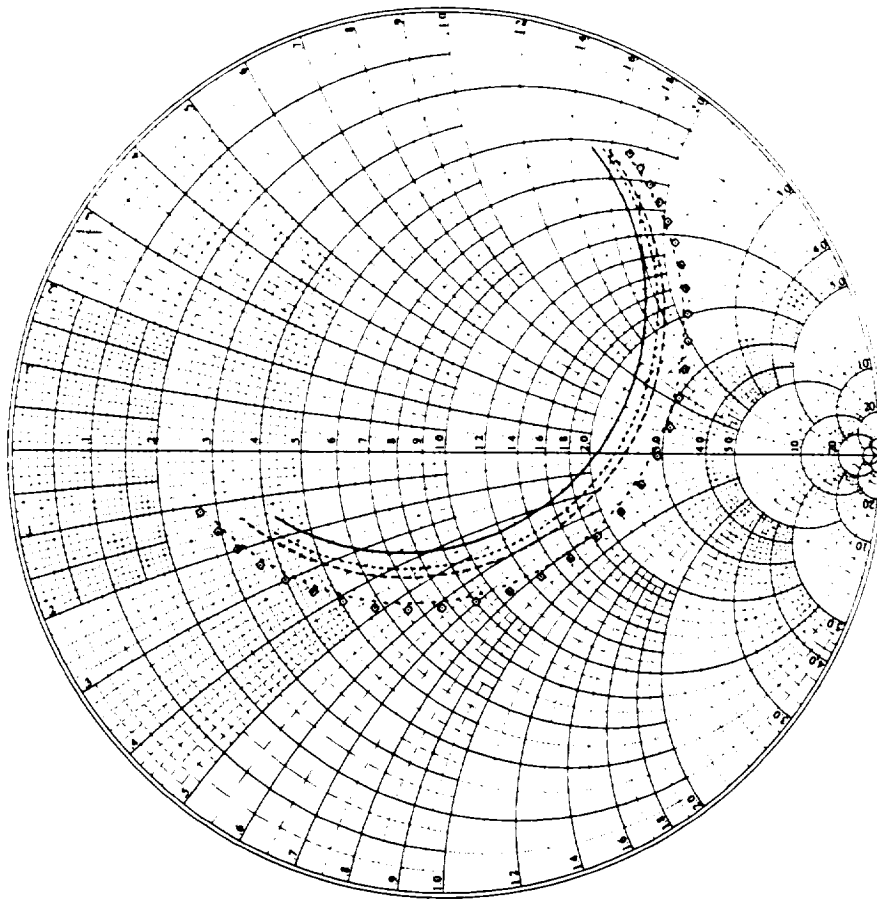


Figure 10: Input impedance of an axially polarized patch antenna for various cylinder radii. The frequency range was 2.4 GHz to 2.7 GHz and the cavity size was 10.5 cm \times 10.5 cm.

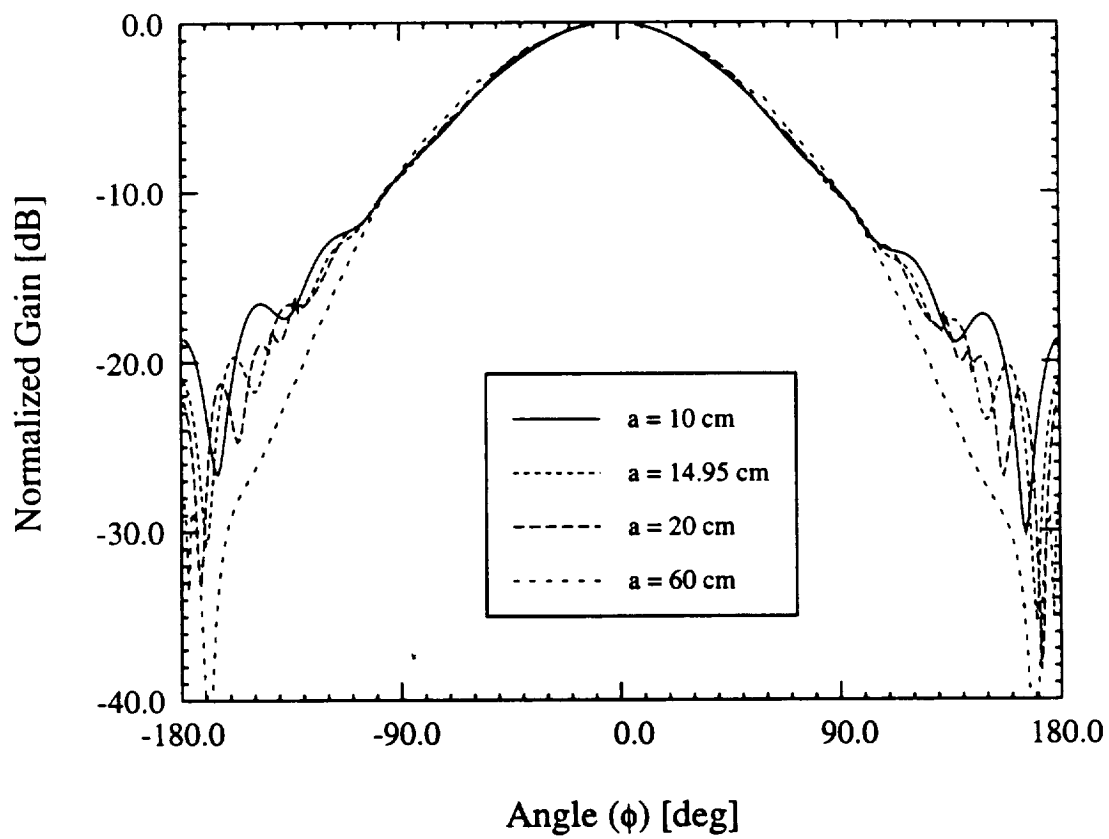


Figure 11: Variation of the radiation pattern shape with respect to curvature for a circumferentially polarized antenna.

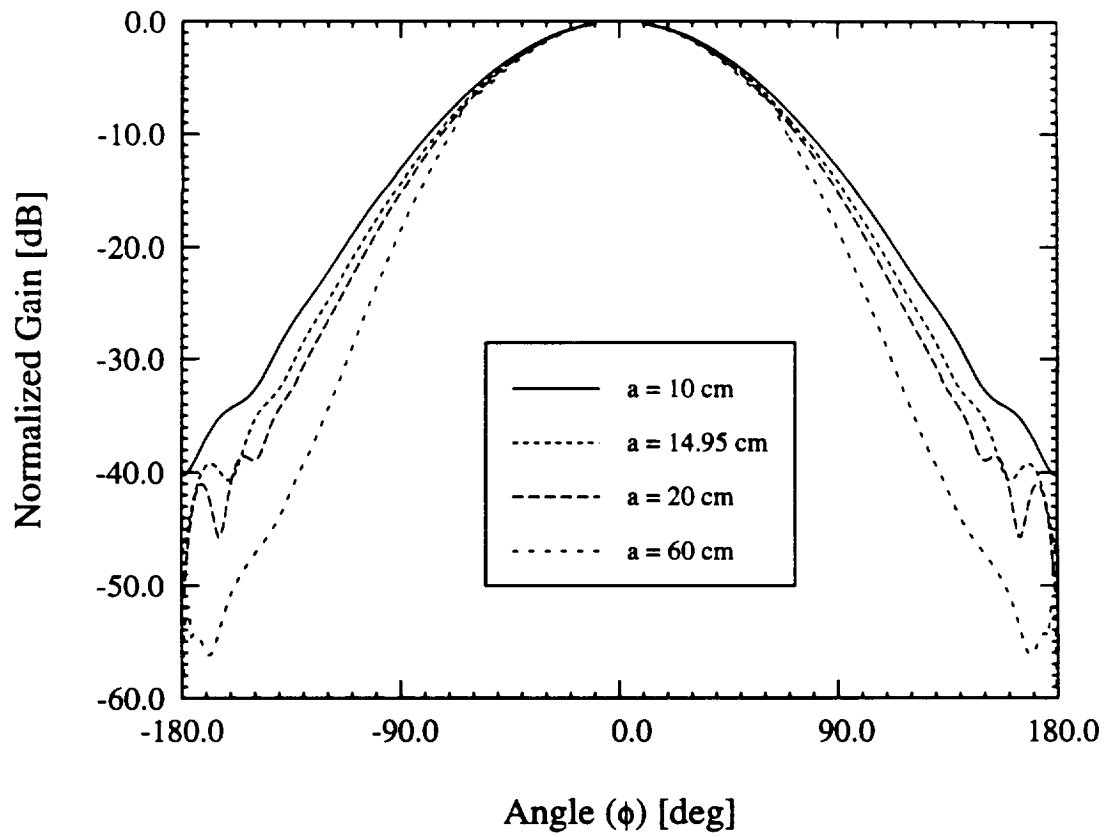


Figure 12: Variation of the radiation pattern shape with respect to curvature for an axially polarized antenna.

surface field with respect to the observation direction.

4 Conclusions

In this paper, we presented a rigorous analysis of the radiation by individual and arrays of patches placed in a cavity recessed in a cylindrical platform. A finite element-boundary integral code was developed and the data generated by this code for a typical cylindrical-rectangular patches were found to compare favorably with measurements. Since the cavity model does not include mutual coupling and the usual integral equation formulations requires large storage and computational resources, the FE-BI formulation is especially attractive for array analysis.

This FE-BI method was used to study the radiation properties of circumferentially and axially polarized patch antennas. The finite cavity size was found to have little effect on the circumferentially polarized E-plane pattern. However, for the H-plane pattern of an axially polarized element, the back lobe is significantly larger for cavities which extend from the front side to the back side of the cylinder. A wraparound antenna exhibited the largest back lobe implying that this lobe is a result of creeping wave shedding rather than diffraction off the lateral metallic walls of the cavity. The presence of a back lobe must be considered when designing low observable, jam-resistant antennas or antennas on complex platforms (e.g. an antenna near an obstruction). Thus, as was the case for scattering reduction, it is advisable to configure the patch antenna in the smallest possible cavity.

The effect of curvature on resonance, gain, radiation pattern shape and input impedance was studied. Both circumferentially and axially polarized antennas were considered and was found that the resonant frequency increased with increasing curvature for both antennas. The gain of both types of patch antennas decreased with increasing curvature with the axially polarized antenna exhibiting greater sensitivity attributed to the orientation of the radiating surface fields and the decreasing driving point impedance. The radiation pattern for axially polarized antennas broadens with increasing curvature while the corresponding patterns for circumferentially polarized antennas does not broaden; however, creeping wave interactions are reduced for the latter element with decreasing curvature as expected. We conclude that axially polarized antennas exhibit more sensitivity to curvature as compared

to their circumferentially polarized counterparts.

References

- [1] Y.T. Lo, D. Solomon and W.F. Richards, "Theory and experiments on microstrip antennas," *IEEE Trans. Antennas and Propagat.*, Vol. 27, pp. 137-145, 1979.
- [2] D.M. Pozar and S.M. Voda, "A rigorous analysis of a microstripline fed patch antenna," *IEEE Antennas Propagat.*, Vol. 35, pp. 1343-1350, Dec. 1987.
- [3] J.R. James and G.J. Wilson, "Microstrip antennas and arrays, Pt. 1 - Fundamental action and limitations," *IEE J. Microwaves, Optics, and Acoustics*, Vol. 1, pp. 165-174, 1977.
- [4] J.S. Dahele, R.J. Mitchell, K.M. Luk and K.F. Lee, "Effect of curvature on characteristics of rectangular patch antenna," *Electronics Letters*, Vol 23, pp. 748-749, 2 July 1987.
- [5] J. Ashkenazy, S. Shtrikman and D. Treves, "Electric surface current model for the analysis of microstrip antennas on cylindrical bodies," *IEEE Antennas Propagat.*, Vol. 33, pp. 295-300, Mar. 1985.
- [6] J. T. Aberle and F. Zavosh, "Analysis of probe-fed circular microstrip patches backed by circular cavities," *Electromagnetics*, Vol. 14, pp. 239-258, Mar-Apr 1994.
- [7] J-M Jin and J.L. Volakis, "A hybrid finite element method for scattering and radiation by microstrip patch antennas and arrays residing in a cavity," *IEEE Trans. Antennas and Propagat.*, Vol. 39, No. 11, pp. 1598-1604, Nov. 1991.
- [8] L.C. Kempel and J.L. Volakis, "Scattering by cavity-backed antennas on a circular cylinder," *IEEE Trans. Antennas and Propagat.*, 1994 (in press).
- [9] J.L. Volakis, A. Chatterjee and J. Gong, "A review of the finite element method for three-dimensional electromagnetic scattering," *J. Opt. Soc. Am. - A*, pp. 1422-1433, Apr. 1994.

- [10] T.M. Hashaby, S.M. Ali and J.A. Kong. "Input impedance and radiation pattern of cylindrical-rectangular and wraparound microstrip antennas." *IEEE Trans. Antennas and Propagat.*, Vol. 38, No. 5, pp. 722-731, May 1990.
- [11] E.V. Sohtell, "Microstrip antennas on a cylindrical surface," in *Handbook of microstrip antennas*, Ed. J.R. James and P.S. Hall, Peregrinus: London, pp. 1227-1255, 1989.
- [12] K-M Luk, K-F Lee and J.S. Dahele, "Analysis of the cylindrical-rectangular patch antenna," *IEEE Trans. Antennas and Propagat.*, Vol. 37, No. 2, pp. 143-147, Feb. 1989.

Scattering by Cavity-Backed Antennas on a Circular Cylinder

94N21886

Leo C. Kempel, *Student Member, IEEE*, and John L. Volakis, *Senior Member, IEEE*

Abstract—Conformal arrays are popular antennas for aircraft, spacecraft, and land vehicle platforms due to their inherent low weight, drag, and observables. However, to date there has been a dearth of rigorous analytical or numerical solutions to aid the designer. In fact, it has been common practice to use limited measurements and planar approximations in designing such nonplanar antennas. In this paper, we extend the finite element-boundary integral method to scattering by cavity-backed structures in an infinite, metallic cylinder. In particular, we discuss the formulation specifics, such as weight functions, dyadic Green's function, implementation details, and particular difficulties inherent to cylindrical structures. Special care is taken to ensure that the resulting computer program has low memory demand and minimal computational requirements. Scattering results are presented and validated as much as possible.

I. INTRODUCTION

CONFORMAL antenna arrays are attractive for aircraft, spacecraft, and land vehicle applications since these antenna systems have low weight, low drag, flexibility, and cost advantages over conventional protruding antennas. The majority of previous studies pertaining to nonplanar conformal antennas has been conducted experimentally due to a dearth of rigorous analysis techniques. Traditional rigorous techniques involve an integral equation and are limited in terms of radius of curvature and structural complexity. Some approximate methods have been considered, but these are restricted in accuracy and element shape.

Recently, the finite element-boundary integral (FE-BI) method was successfully employed for scattering analysis of large cavity-backed planar arrays [1]. The resulting system is sparse due to the local nature of the finite element method, whereas the boundary integral submatrix is fully populated. However, by resorting to an iterative solver such as the Biconjugate Gradient (BiCG) method, the boundary integral subsystem may be cast in circulant form, allowing use of the Fast Fourier Transform (FFT) in performing the matrix-vector products. This BiCG-FFT solution scheme ensures $\mathcal{O}(N)$ memory demand for the entire FE-BI system and minimizes the computational requirements.

In this paper, the FE-BI formulation is extended to scattering by aperture antennas conformal to a cylindrical metallic surface. In contrast to the planar aperture array, the implementation of the cylindrically conformal array requires shell-shaped elements rather than bricks, and the required external

Green's function must satisfy the boundary conditions on the surface of the cylinder. In its exact form, this Green's function is an infinite series that imposes unacceptable computational burdens on the method. However, for large-radius cylinders, a suitable asymptotic formula is available and herein used for an efficient evaluation of the Green's function. In addition, the resulting BI system is again cast in circulant form to ensure an $\mathcal{O}(N)$ memory demand and to take advantage of the FFT's efficiency when carrying out the matrix-vector product.

A primary difficulty in studying cavity-backed antennas mounted on curved surfaces is the lack of reference data. In this paper, scattering calculations based on the FE-BI method are compared with data based on different techniques. Although such validation is necessarily limited, it provides confidence in the formulation's accuracy so that this approach may be used in extending the available reference data.

An alternative approach for terminating the FE mesh is to use an absorbing boundary condition rather than the exact boundary integral used herein. The finite element-absorbing boundary condition (FE-ABC) method is associated with a higher CPU cost because of its enlarged computational domain; however, it is more flexible than the FE-BI method presented in this paper since it may include a complex radome as well as the cavity-backed antenna elements. Such an FE-ABC formulation will be the subject of a future paper.

II. FE-BI FOR CIRCULAR CYLINDERS

In this section, the FE-BI formulation is developed for cavities recessed in an infinite metallic cylinder, having walls that coincide with constant ρ -, ϕ - or z -surfaces (see Fig. 1).

As usual, the finite element formulation permits substantial modeling flexibility, including cavity inhomogeneities, lumped loads, super/substrate antenna configurations, or microstrip lines and so on.

The FE-BI approach possesses both low memory and computational demand when implemented with a BiCG-FFT solver. Although the system of equations associated with the FE formulation is sparse, the boundary integral submatrix is fully populated. However, if the aperture mesh is a uniform grid, the BiCG-FFT solver may be employed for that portion of the system, thus retaining $\mathcal{O}(N)$ memory demand for the entire system. In addition, the solver has low computational demand since the sparse matrix-vector

Manuscript received November 19, 1993; revised April 11, 1994.
The authors are with the Radiation Laboratory, University of Michigan, Ann Arbor, MI 48109-2122.
IEEE Log Number 9404568.

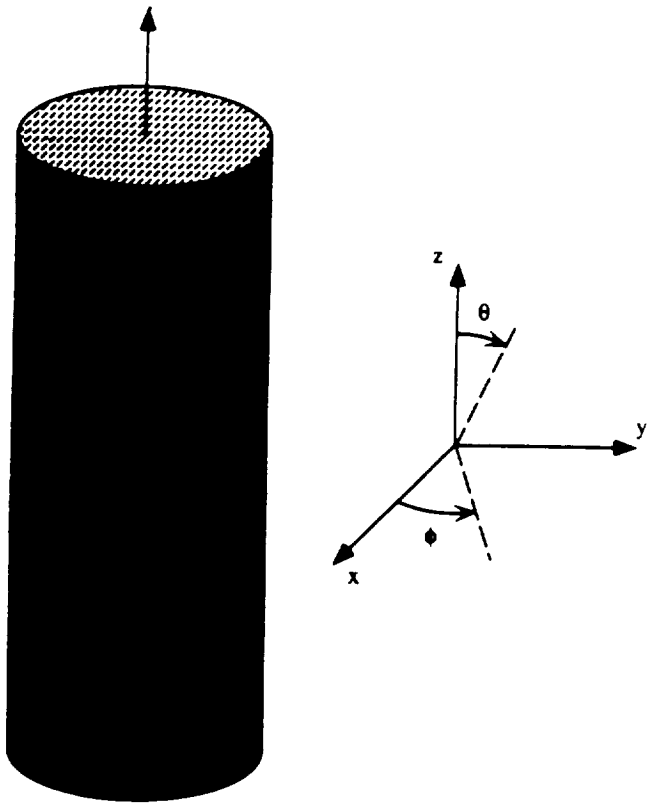


Fig. 1. Illustration of a typical cavity-backed antenna situated on a metallic indenter and the associated coordinate system.

products require $\mathcal{O}(N)$ operations per iteration and the discrete convolutions that utilize FFTs require only $\mathcal{O}(N \log N)$ operations per iteration.

The FE-BI formulation begins with the weak form of the vector wave equation followed by specification of appropriate vector shape functions and a dyadic Green's function. The resulting FE-BI equations are then used to solve for the total electric fields within the cavity and on the aperture (see, for example, Volakis *et al.* [2]). For the specific configuration at hand, the weak form of the wave equation can be written

$$\int_{V_i} \left\{ \frac{\nabla \times \vec{W}_j(\rho, \phi, z) \cdot \nabla \times \vec{W}_i(\rho, \phi, z)}{\mu_r(\rho, \phi, z)} - k_o^2 \epsilon_r(\rho, \phi, z) \vec{W}_j(\rho, \phi, z) \cdot \vec{W}_i(\rho, \phi, z) \right\} \rho d\rho d\phi dz$$

$$+ (k_o a)^2 \delta_a(j) \delta_a(i) \int_{S_i} \int_{S_j} \left[\vec{W}_i(a, \phi, z) \cdot \hat{\rho}(a, \phi, z) \times \overline{\overline{G}}_2(a, \phi, \bar{z}) \times \hat{\rho}(a, \phi', z') \cdot \vec{W}_j(a, \phi', z') \right] d\phi' dz' d\phi dz$$

$$= f_i^{int} + f_i^{ext} \quad (1)$$

thus, \vec{W}_i are vector basis functions with support over volume V_i , which is associated with the i th degree of freedom, and in a similar fashion, S_i and S_j represent aperture faces associated with the i th and j th degrees of freedom, respectively. The appropriate dyadic Green's function denoted by $\overline{\overline{G}}_2$, and it has convolutional ($\bar{\phi} = \phi - \phi'$,

$\bar{z} = z - z'$) form when evaluated on the surface of the cylinder $\rho = a$. The unprimed coordinates represent the test point, while the primed ones denote the source point. The free-space propagation constant is given by $k_o = \frac{2\pi}{\lambda_o}$, where λ_o is the free-space wavelength. The cavity is filled with an inhomogeneous material having relative constitutive properties ϵ_r and μ_r . The function $\delta_a(i)\delta_a(j)$ is the product of two Kronecker delta functions. Hence, it identifies which pairs of unknowns belong to the aperture and accordingly contribute to the boundary integral submatrix. The right-hand side contains an internal source (f_i^{int}) and an external source (f_i^{ext}) term. The former is used only for radiation analysis and is omitted for this paper. The latter is used for scattering analysis and is discussed later.

The FE-BI equation (1) may be rewritten in matrix form as

$$[\mathcal{A}] \begin{Bmatrix} E_j^{ap} \\ E_j^{int} \end{Bmatrix} + \begin{bmatrix} [\mathcal{G}] & [0] \\ [0] & [0] \end{bmatrix} \begin{Bmatrix} E_j^{ap} \\ E_j^{int} \end{Bmatrix} = \begin{Bmatrix} f_i^{ext} \\ 0 \end{Bmatrix} \quad (2)$$

where the entries of $[\mathcal{A}]$ are due to the FE portion of the formulation and $[\mathcal{G}]$ is the boundary integral submatrix. In (2), E_j^{ap} and E_j^{int} denote degrees of freedom associated with the aperture and interior fields, respectively.

An important factor in choosing the finite elements for gridding the cavity is the element's suitability for satisfying the mathematical requirements of the formulation as well as the physical features of the antenna system. Traditional node-based finite elements associate the degrees of freedom with the nodal fields and have proven unsatisfactory for three-dimensional electromagnetics applications since they do not correctly represent the null space of the curl operator, and hence spurious modes are generated [3]–[4]. In contrast, edge-based elements correctly model the curl operator and therefore the electromagnetic fields. In addition, edge-based elements avoid explicit specification of the fields at corners where edge conditions may require a singularity. Jin and Volakis [6] presented edge-based brick elements, which are convenient for rectangular-type structures and cavities. For cavities residing in a circular cylinder, shell elements are the natural choice.

Cylindrical shell elements possess both geometrical fidelity and simplicity for cylindrical-rectangular cavities. Fig. 2 illustrates a typical shell element, which has eight nodes connected by twelve edges: four edges aligned along each of the three orthogonal directions of the cylindrical coordinate system. Each element is associated with twelve vector shape functions given by

$$\vec{W}_{12}(\rho, \phi, z) = \vec{W}_\rho(\rho, \phi, z; \phi_r, z_t, +)$$

$$\vec{W}_{43}(\rho, \phi, z) = \vec{W}_\rho(\rho, \phi, z; \phi_l, z_t, -)$$

$$\vec{W}_{56}(\rho, \phi, z) = \vec{W}_\rho(\rho, \phi, z; \phi_r, z_b, -)$$

$$\vec{W}_{87}(\rho, \phi, z) = \vec{W}_\rho(\rho, \phi, z; \phi_l, z_b, +)$$

$$\vec{W}_{14}(\rho, \phi, z) = \vec{W}_\phi(\rho, \phi, z; \rho_b, \dots, z_t, +)$$

$$\vec{W}_{23}(\rho, \phi, z) = \vec{W}_\phi(\rho, \phi, z; \rho_a, \dots, z_t, -)$$

$$\vec{W}_{58}(\rho, \phi, z) = \vec{W}_\phi(\rho, \phi, z; \rho_b, \dots, z_b, -)$$

$$\vec{W}_{67}(\rho, \phi, z) = \vec{W}_\phi(\rho, \phi, z; \rho_a, \dots, z_b, +)$$

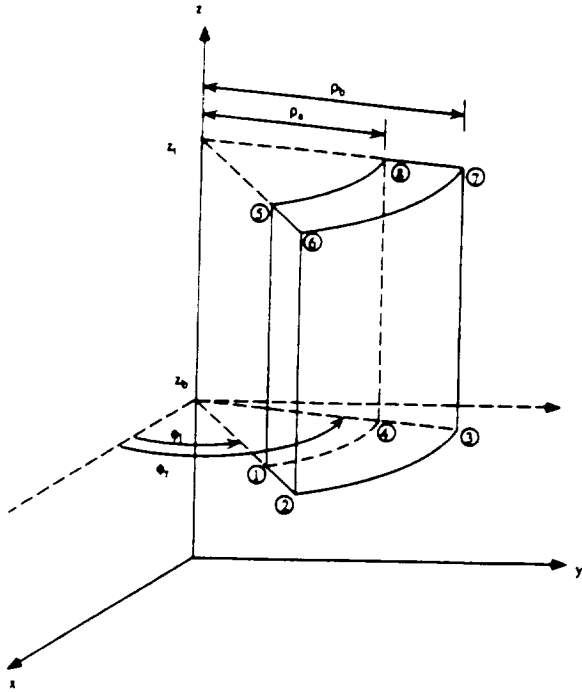


Fig. 2. Cylindrical shell element.

$$\begin{aligned}
 \vec{W}_{15}(\rho, \phi, z) &= \vec{W}_z(\rho, \phi, z; \rho_b, \phi_r, \cdot, +), \\
 \vec{W}_{26}(\rho, \phi, z) &= \vec{W}_z(\rho, \phi, z; \rho_a, \phi_r, \cdot, -) \\
 \vec{W}_{48}(\rho, \phi, z) &= \vec{W}_z(\rho, \phi, z; \rho_b, \phi_l, \cdot, -), \\
 \vec{W}_{37}(\rho, \phi, z) &= \vec{W}_z(\rho, \phi, z; \rho_a, \phi_l, \cdot, +)
 \end{aligned} \quad (3)$$

where \vec{W}_{lk} is associated with the edge which is delimited by local nodes (l, k) , as shown in Fig. 2. As seen from (3), three fundamental vector weight functions are required for the complete representation of the shell element. They are

$$\begin{aligned}
 \vec{W}_\rho(\rho, \phi, z; \tilde{\rho}, \tilde{\phi}, \tilde{z}, \tilde{s}) &= \frac{\tilde{s}\rho_b(\phi - \tilde{\phi})(z - \tilde{z})}{\alpha h} \hat{\rho} \\
 \vec{W}_\phi(\rho, \phi, z; \tilde{\rho}, \tilde{\phi}, \tilde{z}, \tilde{s}) &= \frac{\tilde{s}}{th}(\rho - \tilde{\rho})(z - \tilde{z}) \hat{\phi} \\
 \vec{W}_z(\rho, \phi, z; \tilde{\rho}, \tilde{\phi}, \tilde{z}, \tilde{s}) &= \frac{\tilde{s}}{t\alpha}(\rho - \tilde{\rho})(\phi - \tilde{\phi}) \hat{z}
 \end{aligned} \quad (4)$$

where the element parameters $(\rho_a, \rho_b, \phi_l, \phi_r, z_b, z_t)$ are shown in Fig. 2, $t = \rho_b - \rho_a$, $\alpha = \phi_r - \phi_l$, and $h = z_t - z_b$. Each local edge is distinguished by $\tilde{\rho}$, $\tilde{\phi}$, \tilde{z} , and \tilde{s} as given in (3). The $\frac{1}{\rho}$ -term, which appears in the definition of the $\hat{\rho}$ -directed weight (4), is essential in satisfying the divergence free requirement, i.e., so that $\nabla \cdot \vec{W}_j = 0$.¹ Note that as the radius of the cylinder becomes large, the curvature of these elements decreases, resulting in weight functions that are functionally similar to the bricks presented by Jin and Volakis [6]. Having specified the vector basis functions, we may proceed to develop the matrix entries for the system (2).

The FE-BI system is composed of two parts: a sparse FE matrix and a fully populated BI submatrix, as shown in (2).

¹ $\vec{W}_j(\rho, \phi, z)$ will satisfy this requirement only within the volume of the element. These weighting functions introduce artificial charges on the faces of the element and are not divergenceless at element interfaces. This is allowable since these elements do not guarantee normal field continuity across the element faces.

The FE matrix entries are represented by

$$A_{ij} = \frac{1}{\mu_r} I_{st}^{(1)ij} - k_o^2 \epsilon_r I_{st}^{(2)ij} \quad (5)$$

where constant material properties have been assumed within each element. The subscripts (i, j) refer to the row and column of the matrix entry and correspond to the test and source edges, respectively. The auxiliary functions

$$\begin{aligned}
 I_{st}^{(1)ij} &= \int_{V_i} \nabla \times \vec{W}_s(\rho, \phi, z; \tilde{\rho}_j, \tilde{\phi}_j, \tilde{z}_j, \tilde{s}_j) \\
 &\quad \cdot \nabla \times \vec{W}_t(\rho, \phi, z; \tilde{\rho}_i, \tilde{\phi}_i, \tilde{z}_i, \tilde{s}_i) \rho d\rho d\phi dz \\
 I_{st}^{(2)ij} &= \int_{V_i} \vec{W}_s(\rho, \phi, z; \tilde{\rho}_j, \tilde{\phi}_j, \tilde{z}_j, \tilde{s}_j) \\
 &\quad \cdot \vec{W}_t(\rho, \phi, z; \tilde{\rho}_i, \tilde{\phi}_i, \tilde{z}_i, \tilde{s}_i) \rho d\rho d\phi dz
 \end{aligned} \quad (6)$$

are identically zero unless both test and source edges share at least one element in common, resulting in a highly sparse system. Physically, such a system is a consequence of the locality property inherent in a partial differential equation formulation. In (6), the direction of the source and test edges are represented by $(s, t) \in \{\rho, \phi, z\}$, respectively. Since the edges of the mesh are aligned along three orthogonal directions, only six unique combinations of (s, t) are required for $I^{(1)}$, and only three such combinations for $I^{(2)}$. Since (6) is symmetric with respect to source and test edges, the FE matrix will also be symmetric. Evaluations of (6) using (4) are presented in the Appendix.

A lumped impedance post may be included in the formulation by adding a term to (1) and equivalently to (5); surface or subsurface metallization layers may also be modeled. Radially oriented lumped loads are approximated in the FE-BI formulation by a filamentary load located at (ϕ_L, z_L) [2]. Such posts have length l , cross-sectional area s and impedance Z_L . The contribution to $[\mathcal{A}]$ is given by

$$A_{ij} = jk_o Z_o \frac{l}{sZ_L} \int_V \frac{\delta(\phi - \phi_L)\delta(z - z_L)}{\rho} \cdot W_i(\rho, \phi, z) W_j(\rho, \phi, z) \rho d\rho d\phi dz \quad (7)$$

which may be readily evaluated in closed form. In addition, infinitesimally thin metallization layers may be represented by simply fixing *a priori* the weight coefficients to zero for weights associated with edges which are tangential to the metal. This is a consequence of using a total electric field formulation. The symmetry and sparsity of the FE system $[\mathcal{A}]$ is maintained after the addition of these loads, while the BI system $[\mathcal{G}]$ remains fully populated and symmetric.

The boundary integral provides an exact boundary condition for mesh closure, and its construction relies on a cylindrical dyadic Green's function. The entries of the boundary integral submatrix are

$$\begin{aligned}
 G_{ij} &= (k_o a)^2 \int_{S_i} \int_{S_j} W_t(a, \phi, z; \tilde{\rho}_i, \tilde{\phi}_i, \tilde{z}_i, \tilde{s}_i) \\
 &\quad \left[\hat{\rho}(a, \phi, z) \times \overline{\overline{G}}_2(a, \phi, \tilde{z}) \times \hat{\rho}(a, \phi', z') \right] \\
 &\quad \cdot W_s(a, \phi', z'; \tilde{\rho}_j, \tilde{\phi}_j, \tilde{z}_j, \tilde{s}_j) d\phi' dz' d\phi' dz'
 \end{aligned} \quad (8)$$

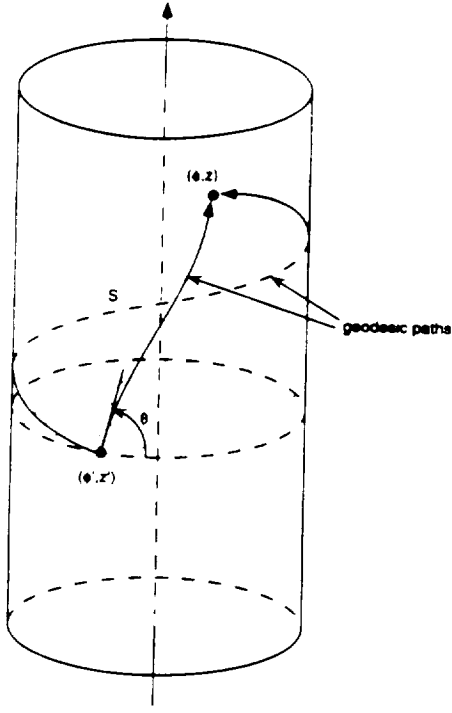


Fig. 3. Geodesic paths on a circular cylinder.

where the weight functions are given by (4) and evaluated at the surface $\rho = a$. In (8), the dyadic Green's function ($\bar{\bar{G}}_2$) satisfies both the radiation condition, and the Neumann boundary condition at $\rho = a$. This dyadic Green's function may be expressed exactly [8]

$$\begin{aligned}
 G^{zz}(a, \bar{\phi}, \bar{z}) &= -\frac{1}{(2\pi)^2} \sum_{n=-\infty}^{\infty} \int_{-\infty}^{\infty} \left(\frac{k_\rho}{k_o}\right)^2 \frac{1}{\gamma} \frac{H_n^{(2)}(\gamma)}{H_n^{(2)'}(\gamma)} e^{j(n\bar{\phi} - k_z \bar{z})} dk_z \\
 G^{\phi z}(a, \bar{\phi}, \bar{z}) &= -\frac{1}{(2\pi)^2} \sum_{n=-\infty}^{\infty} \int_{-\infty}^{\infty} \left(\frac{nk_z}{k_o^2 a \gamma}\right) \frac{H_n^{(2)}(\gamma)}{H_n^{(2)'}(\gamma)} e^{j(n\bar{\phi} - k_z \bar{z})} dk_z \\
 G^{\phi\phi}(a, \bar{\phi}, \bar{z}) &= \frac{1}{(2\pi)^2} \sum_{n=-\infty}^{\infty} \int_{-\infty}^{\infty} \frac{1}{\gamma} \\
 &\quad \cdot \left[\frac{H_n^{(2)'}(\gamma)}{H_n^{(2)'}(\gamma)} - \left(\frac{nk_z}{k_o a k_\rho}\right)^2 \frac{H_n^{(2)}(\gamma)}{H_n^{(2)'}(\gamma)} \right] e^{j(n\bar{\phi} - k_z \bar{z})} dk_z \quad (9)
 \end{aligned}$$

where $\gamma = k_\rho a$ and $k_\rho = \sqrt{k_o^2 - k_z^2}$. However, for large radius cylinders (e.g., $ka \geq 3$), (9) is computationally prohibitive. In these cases, which are of main concern in this paper, it is advantageous to employ an asymptotic expression for $\bar{\bar{G}}_2$ [9]-[12]. These employ a creeping wave series expansion of which only the two direct path contributions (see Fig. 3) are retained.

The formula due to Pathak and Wang [9]

$$G^{zz}(a, \bar{\phi}, \bar{z}) \sim -\frac{jk_o}{2\pi} q e^{-jk_o s}$$

$$\begin{aligned}
 &\cdot \left\{ (\cos^2 \theta + q(1-q)(2-3\cos^2 \theta)) [v(\beta) - 1] \right\} \\
 G^{\phi z}(a, \bar{\phi}, \bar{z}) &\sim \frac{jk_o}{2\pi} q e^{-jk_o s} \\
 &\cdot \sin \theta \cos \theta \left\{ (1-3q(1-q)) [v(\beta) - 1] \right\} \\
 G^{\phi\phi}(a, \bar{\phi}, \bar{z}) &\sim -\frac{jk_o}{2\pi} q e^{-jk_o s} \\
 &\cdot \left\{ (\sin^2 \theta + q(1-q)(2-3\sin^2 \theta)) [v(\beta) - 1] \right. \\
 &\quad \left. + q [\sec^2 \theta (u(\beta) - v(\beta))] \right\} \quad (10)
 \end{aligned}$$

where $\beta = ks \left[\frac{\cos^2 \theta}{\sqrt{2} k_o a} \right]^{\frac{1}{2}}$ and $q = \frac{1}{k_o s}$ has proven quite accurate. In the definition of β , s is the usual geodesic path length ($s = \sqrt{(a\bar{\Phi})^2 + z^2}$) and θ is the direction of the geodesic trajectory ($\theta = \tan^{-1} \left[\frac{a\bar{\Phi}}{z} \right]$). Depending on which of the two direct paths (shown in Fig. 3) is used, $\bar{\Phi} = \bar{\phi}$ or $\bar{\Phi} = 2\pi - \bar{\phi}$. The soft and hard Fock functions, $u(\beta)$ and $v(\beta)$, respectively, are characteristic of on-surface creeping wave interactions and have been extensively investigated by Logan [13]. These functions are also presented in the appendix of this paper. Although computation of the Green's function (10) is now tractable, evaluation of (8) must be done so that a discrete convolutional system is maintained and the singularity of (8) at $s = 0$ is properly treated.

Care must be taken in evaluating (8) so that the overall storage requirement remains $\mathcal{O}(N)$ and the singular integrals of (8) are accurately computed. If uniform zoning is used, the resulting submatrix (\mathcal{G}) is block Toeplitz and hence amenable to solution using the BiCG-FFT method. For the nonself-cell contributions, midpoint integration may be used while a regularization procedure must be employed for the self-cell. Bird [12] noted that (8) recovers the metallic screen Green's function when $\beta = 0$ within the available approximation order. This suggests that (8) may be regularized by adding and subtracting from (10) the function

$$2\bar{\bar{G}}_o(a, \bar{\phi}, \bar{z}) = \left[\bar{I} + \frac{\nabla \nabla}{k_o^2} \right] \frac{e^{-jk_o R}}{2\pi R} \quad ; \quad R = |\bar{r} - \bar{r}'| \quad (11)$$

which is the free-space dyadic Green's function multiplied by two. The resulting regularized Green's function (curvature contribution) is given by

$$\begin{aligned}
 \tilde{G}^{zz}(a, \bar{\phi}, \bar{z}) &\sim -\frac{jk_o}{2\pi} q e^{-jk_o s} \left\{ (\cos^2 \theta + q(1-q)) \right. \\
 &\quad \left. \cdot (2-3\cos^2 \theta) [v(\beta) - 1] \right\} \\
 \tilde{G}^{\phi z}(a, \bar{\phi}, \bar{z}) &\sim \frac{jk_o}{2\pi} q e^{-jk_o s} \sin \theta \cos \theta \left\{ (1-3q(1-q)) \right. \\
 &\quad \left. \cdot [v(\beta) - 1] \right\}
 \end{aligned}$$

$$G^{(1)}(a, \phi, z) \sim -\frac{jk_o a}{2\pi} q e^{-jk_o z} \left\{ (1 - \sin^2 \theta - q)(1 - q) \right. \\ \left. + (2 - 3\sin^2 \theta) [r(\beta) - 1] \right. \\ \left. + q [\sec^2 \theta (u(\beta) - r(\beta))] \right\} \quad (12)$$

and since it is no longer singular it may be evaluated numerically. The planar contribution may be calculated in the manner described previously by Jin and Volakis [5]. The FE-BI matrix has now been fully developed and it remains to specify the excitation function for external sources.

III. PLANE WAVE EXCITATION

Plane wave excitation of the geometry is considered in this section for scattering analysis. The use of the exact boundary condition in (1) allows coupling of an exterior excitation field into the cavity. We will describe the form of the source function f_i^{ext} and discuss its numerical implementation.

The forcing function, due to exterior sources (f_i^{ext}) is given by

$$f_i^{ext} = jZ_o k_o a \int_{S_i} \bar{W}_i(a, \phi', z') \cdot \hat{\rho}(a, \phi', z') \\ \times \bar{H}^{cyl}(a, \phi', z') d\phi' dz' \quad (13)$$

where $\bar{W}_i(\rho, \phi, z)$ is the testing weight for the i th row of the matrix and \bar{H}^{cyl} represents the magnetic field on the cylinder's surface in the absence of the cavity. A plane wave

$$\bar{E}^i = \hat{e}^i e^{-jk_o(k^i \cdot \bar{r})} \\ \bar{H}^i = Y_o \left[\hat{\rho}(\sin \gamma \cos \theta, \cos \bar{\phi}_i - \cos \gamma \sin \bar{\phi}_i) \right. \\ \left. - \hat{\phi}(\sin \gamma \cos \theta, \sin \bar{\phi}_i + \cos \gamma \cos \bar{\phi}_i) \right. \\ \left. - \hat{z} \sin \gamma \sin \theta_i \right] e^{jk_o[a \sin \theta_i \cos \bar{\phi}_i + z \cos \theta_i]} \quad (14)$$

is assumed to be incident on the cylinder from the direction (θ_i, ϕ_i) , where γ is the polarization angle and $\hat{e}^i = \hat{\theta}^i \cos \gamma + \hat{\phi}^i \sin \gamma$ is the electric field polarization. In these, the difference between the observation and incidence angles is denoted by $\bar{\phi}_i = \phi - \phi_i$. The total surface field is given by the sum of the incident and corresponding scattered field from the infinite metallic cylinder [14]. Specifically,

$$\bar{H}^{cyl}(a, \phi, z) = \bar{H}^i(a, \phi, z) + \bar{H}_{cyl}^s(a, \phi, z) \\ = \hat{c} H_o^{cyl} + \hat{z} H_z^{cyl} \quad (15)$$

where

$$H_o^{cyl}(a, \phi, z) = -2Y_o \frac{e^{jk_o z \cos \theta}}{\pi k_o a \sin \theta_i} \sum_{n=-\infty}^{\infty} \left[\frac{\cos \gamma}{H_n^{(2)}(k_o a \sin \theta_i)} \right. \\ \left. + j \frac{n}{k_o a \sin \theta_i} \frac{\sin \gamma \cos \theta_i}{H_n^{(2)}(k_o a \sin \theta_i)} \right] e^{jn(\frac{\phi}{2} + \phi - \phi_i)} \\ H_z^{cyl}(a, \phi, z) = j2Y_o \frac{\sin \gamma}{\pi k_o a} e^{jk_o z \cos \theta_i} \sum_{n=-\infty}^{\infty} \\ \left[\frac{e^{jn(\frac{\phi}{2} + \phi - \phi_i)}}{H_n^{(2)}(k_o a \sin \theta_i)} \right] \quad (16)$$

is obtained from traditional modal analysis. These expressions may be approximated by retaining only a few terms of the series if $k_o a \sin \theta_i$ is small. However, as this parameter becomes large (e.g., for large a and $\theta_i \rightarrow 90^\circ$), (16) may be replaced with equivalent asymptotic representations similar to those considered earlier. Utilizing Watson's transformation and Fock theory [14] in connection with (16), we find that

$$H_z^{cyl} \sim -Y_o \sin \gamma \sin \theta_i e^{jk_o z \cos \theta_i} \\ \cdot \sum_{p=1}^2 e^{-jk_o a \sin \theta_i \Phi_p} \left[g^{(0)}(m \Phi_p) \right]^* \\ H_o^{cyl} \sim j2Y_o \cos \gamma \frac{m^2}{k_o a \sin \theta_i} e^{jk_o z \cos \theta_i} \\ \cdot \sum_{p=1}^2 e^{-jk_o a \sin \theta_i \Phi_p} \left[f^{(0)}(m \Phi_p) \right]^* \\ - Y_o \sin \gamma \cos \theta_i e^{jk_o z \cos \theta_i} \\ \cdot \sum_{p=1}^2 (-1)^p e^{-jk_o a \sin \theta_i \Phi_p} \left[g^{(0)}(m \Phi_p) \right. \\ \left. - j \frac{m}{k_o a \sin \theta_i} g^{(1)}(m \Phi_p) \right]^* \quad (17)$$

in which $\Phi_1 = \frac{3\pi}{2} - (\phi - \phi_i)$, $\Phi_2 = (\phi - \phi_i) - \frac{\pi}{2}$, $m = \left[\frac{k_o a \sin \theta_i}{2} \right]^{\frac{1}{2}}$, and complex conjugation is denoted by an asterisk. The appropriate far-zone Fock functions ($g^{(0)}$, $g^{(1)}$, and $f^{(0)}$) are given by Logan [13] and are also presented in the appendix of this paper.

The asymptotic formulas (17) are quite accurate except in the geometrical optics region ($\phi \approx \phi_i$). In this case, Goriainov's [15] expressions

$$H_z^{cyl} \sim -Y_o \sin \alpha \sin \theta_i e^{jk_o z \cos \theta_i} \left\{ e^{-jk_o a \sin \theta_i \Phi_1} \left[g^{(0)}(m \Phi_1) \right]^* \right. \\ \left. + e^{jk_o a \sin \theta_i \cos(\phi - \phi_i)} \left[G(-m \cos(\phi - \phi_i)) \right]^* \right\} \\ H_o^{cyl} \sim j2Y_o \cos \alpha \frac{m^2}{k_o a \sin \theta_i} e^{jk_o z \cos \theta_i} \left\{ e^{-jk_o a \sin \theta_i \Phi_1} \left[f^{(0)}(m \Phi_1) \right]^* \right. \\ \left. + e^{jk_o a \sin \theta_i \cos(\phi - \phi_i)} \left[F(-m \cos(\phi - \phi_i)) \right]^* \right\} \\ + Y_o \sin \alpha \cos \theta_i e^{jk_o z \cos \theta_i} \left\{ e^{-jk_o a \sin \theta_i \Phi_1} \left[g^{(0)}(m \Phi_1) \right. \right. \\ \left. - j \frac{m}{k_o a \sin \theta_i} g^{(1)}(m \Phi_1) \right]^* \\ \left. - e^{jk_o a \sin \theta_i \cos(\phi - \phi_i)} \left[G(-m \cos(\phi - \phi_i)) \right. \right. \\ \left. - j \frac{m}{k_o a \sin \theta_i} G^{(1)}(-m \cos(\phi - \phi_i)) \right]^* \left. \right\} \quad (18)$$

have been found to be more accurate and can be used instead of (17). The Fock functions (G , $G^{(1)}$ and F) are again defined in Logan [13] and given in the appendix. These surface field expressions may be used to calculate the entries of the column vector $\{f_i^{ext}\}$ efficiently via a numerical evaluation of (13). In particular, the modal series (16) is used when $k_0 a \sin \theta_i \leq 10$ and either (17) or (18) for $k_0 a \sin \theta_i > 10$, as appropriate. With the excitation function and the FE-BI matrix now specified, the BiCG-FFT method [16]–[17] may be used to determine the unknown electric fields within the cavity.

IV. SCATTERING

Once the cavity aperture and volume electric fields have been determined by solving (2) for an external excitation, the radar cross section (RCS) may be calculated. The far-zone fields may be computed by integrating the aperture fields with a suitable Green's function. In this section we present the relevant formula for calculating the far-zone fields and hence the RCS due to excitation by a plane wave (14).

To determine the far-zone fields, we begin with the integral representation for the scattered magnetic field in terms of the aperture fields. We have

$$\vec{H}^s(r, \theta, \phi) = jY_0 k_0 a \int_S \vec{G}_2(r, \theta, \phi; a, \phi', z') \cdot [\hat{\rho}(a, \phi', z') \times \vec{E}(a, \phi', z')] d\phi' dz' \quad (19)$$

with (r, θ, ϕ) indicating the observation point in spherical coordinates. When the observation point is very far from the cylinder, the dyadic Green's function in (19) can be replaced by its far-zone representation

$$\vec{G}_2(r, \theta, \phi; a, \phi', z') \sim \frac{e^{-jk_0 r}}{k_0 r} [G^{\theta\phi} \hat{\theta} \hat{\phi}' + G^{\theta z} \hat{\theta} \hat{z}' + G^{\phi\phi} \hat{\phi} \hat{\phi}'] \quad (20)$$

where the unprimed unit vectors are functions of the observation position and the primed ones are functions of the integration point in (19). The components of this far-zone Green's function

$$\begin{aligned} G^{\theta\phi} &\sim \frac{j}{(2\pi)^2} \frac{2k_0 \cos \theta}{(k_0 a \sin \theta)^2} e^{jk_0 \cos \theta z'} \\ &\cdot \sum_{n=-\infty}^{\infty} \frac{n}{H_n^{(2)}(k_0 a \sin \theta)} e^{jn(\frac{\pi}{2} + (\phi - \phi'))} \\ G^{\theta z} &\sim \frac{j}{(2\pi)^2} \frac{2}{a} e^{jk_0 \cos \theta z'} \\ &\cdot \sum_{n=-\infty}^{\infty} \frac{1}{H_n^{(2)}(k_0 a \sin \theta)} e^{jn(\frac{\pi}{2} + (\phi - \phi'))} \\ G^{\phi\phi} &\sim \frac{j}{(2\pi)^2} \frac{2}{a \sin \theta} e^{jk_0 \cos \theta z'} \\ &\cdot \sum_{n=-\infty}^{\infty} \frac{1}{H_n^{(2)}(k_0 a \sin \theta)} e^{jn(\frac{\pi}{2} + (\phi - \phi'))} \end{aligned} \quad (21)$$

are determined by a mode matching procedure. As one might expect, these series converge rather slowly for large $k_0 a \sin \theta$.

They must therefore be recast in another form by employing Watson's transformation and Fock theory, as was done previously (17). In doing so, we obtain

$$\begin{aligned} G^{\theta\phi} &\sim \frac{k_0 \cos \theta}{4\pi} e^{jk_0 \cos \theta z'} \sum_{p=1}^2 (-1)^{p-1} e^{-jk_0 a \sin \theta \Phi_p} \\ &\cdot \left[g^{(10)}(m\Phi_p) - j \frac{m}{k_0 a \sin \theta} g^{(11)}(m\Phi_p) \right] \\ G^{\theta z} &\sim -\frac{k_0 \sin \theta}{4\pi} e^{jk_0 \cos \theta z'} \sum_{p=1}^2 (-1)^{p-1} e^{-jk_0 a \sin \theta \Phi_p} \left[g^{(10)}(m\Phi_p) \right] \\ G^{\phi\phi} &\sim \frac{m^2}{2a\pi \sin \theta} e^{jk_0 \cos \theta z'} \sum_{p=1}^2 (-1)^{p-1} e^{-jk_0 a \sin \theta \Phi_p} \left[f^{(10)}(m\Phi_p) \right] \end{aligned} \quad (22)$$

where the Fock functions are the same as those used with (17) due to reciprocity. As was the case for the plane wave source, Goriainov's [15] approximations are more accurate in the geometrical optics region ($\phi \approx \phi_0$) and similar expressions may be obtained for (22), as was found for (17). The far-zone scattered field can be computed numerically by using (19) and either the series or asymptotic formula as appropriate. Having done so, the RCS is calculated from

$$\sigma(\theta, \phi) = \lim_{r \rightarrow \infty} 4\pi r^2 \frac{|\vec{E}^s(r, \theta, \phi)|}{|\vec{E}^i(r, \theta, \phi)|} \quad (23)$$

Above we presented a FE-BI formulation suitable for modeling cavity-backed structures embedded in a circular cylinder. Next, we consider a few numerical calculations aimed at validating this formulation and giving us an appreciation on how the cylinder's curvature influences the scattering parameters.

V. RESULTS

Having solved for the electric fields induced by an incident plane wave, the resulting RCS data must be validated with known results. As previously mentioned, available measured or computed data is rather scarce, and as a consequence we are forced to rely on limiting cases in order to validate this work. As the radius of curvature decreases, a cylindrical-rectangular cavity will approximate a planar-rectangular cavity. Another limiting case involves comparison of an elongated 3-D cavity with a corresponding 2-D cavity for normal incidence ($\theta_i = 90^\circ$). Finally, we may compare our infinite cylinder results with a finite body of revolution (BOR) model for certain polarizations and angles of incidence. We begin with the quasiplanar case.

The first validation effort for scattering by cavity-backed patch antennas relies on the fact that a small patch on a very large radius cylinder is quasiplanar and approximates rather well an equal sized planar patch. For our test we chose as a reference a planar 3.678 cm \times 2.75 cm patch residing on a 7.34 cm \times 5.334 cm \times 0.1448 cm cavity filled with a dielectric having $\epsilon_r = 4$. The equivalent patch on a 32.6 cm cylinder is 6.46° \times 2.75 cm residing on a 12.90° \times 5.334 cm \times 0.1448

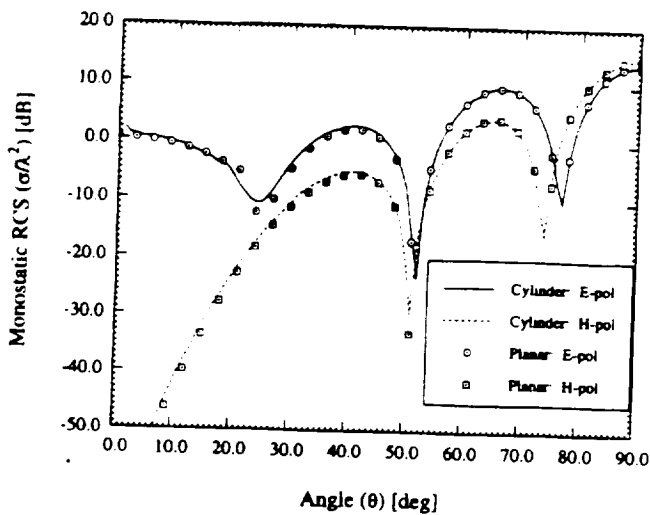


Fig. 4. Comparison of RCS for a planar patch (3.678 cm × 2.75 cm) residing on a 7.34 cm × 5.334 cm × 0.1448 cm cavity filled with $\epsilon_r = 4$ dielectric and a corresponding quasi-planar patch on a large radius (32.6 cm) cylinder. The operating frequency is 9.2 GHz.

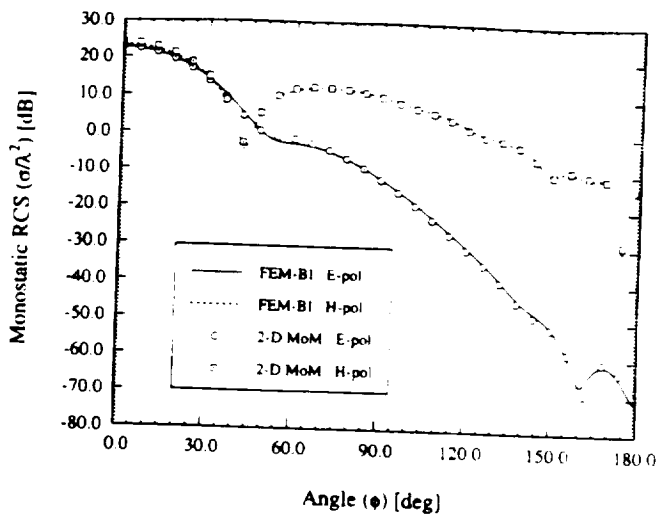


Fig. 5. Comparison of 2-D MoM results and FE-BI RCS results for a $45^\circ \times 5\lambda_0 \times 0.1\lambda_0$ air-filled cavity that is recessed in a cylinder with a radius of $1\lambda_0$.

cm cavity. At the operating frequency of 9.2 GHz, the cylinder has an electrical radius of $10\lambda_0$.

Fig. 4 shows the results for the patch on a large radius cylinder with corresponding data for the planar cavity-backed patch. Clearly, the two RCS patterns are in excellent agreement, and although Fig. 4 illustrates only monostatic scattering in the $\phi = 0^\circ$ plane, additional runs for normally incident monostatic scattering and various bistatic situations yield similar agreement.

Comparisons may also be made for elongated cavities and 2-D MoM results. Long narrow cavities have very little axial interaction for principal plane ($\theta = 90^\circ$) excitation and therefore results based on this formulation should compare well with corresponding 2-D data. It is well known that the RCS of a 3-D scattering body of length $L \gg \lambda_0$ is related to the corresponding 2-D scattering of the same cross section via the relation

$$\sigma_{3D} = 2 \left(\frac{L}{\lambda_0} \right)^2 \sigma_{2D}. \quad (24)$$

Such a comparison is shown in Fig. 5 for monostatic scattering by a $45^\circ \times 5\lambda \times 0.1\lambda$ cavity recessed in a cylinder with a radius of $1\lambda_0$ for both principal polarizations. Once again the agreement between the two results is excellent, thus providing a partial validation of the formulation for highly curved geometries. We remark that similar agreement has been observed for bistatic scattering in the $\theta = 90^\circ$ plane.

The planar approximation eliminates the effects of curvature, which is a primary interest in this work, and the 2-D comparisons done above are only valid for normal incidence and observation. To consider oblique angles and a highly curved structure, we resort to comparisons with a body of revolution (BOR) code for wraparound cavities. Since the BOR code can only model finite structures, we simulate an infinite cylinder by coherently subtracting the far-zone fields

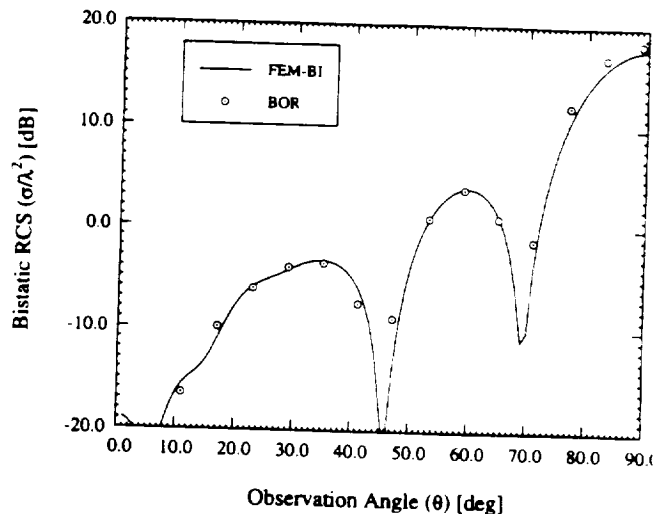


Fig. 6. Comparison of the RCS computed via the FE-BI method and a BOR code for a $3\lambda_0 \times 0.1\lambda_0$ air-filled wraparound cavity recessed in a cylinder with a radius of $1\lambda_0$ that is excited by a normally incident H-polarized ($\alpha = 90^\circ$) plane wave.

of the finite structure without a cavity from similar data which includes the cavity. Such a procedure mimics common measurement practices and was found suitable for near normal incidence and quite acceptable near grazing incidence in the case of H-polarization ($\alpha = 90^\circ$). An example calculation for the former case is given in Fig. 6, where a bistatic scattering pattern is presented in the $\phi = 0^\circ$ plane due to a plane wave incident at $(\theta_i = 90^\circ, \phi_i = 0^\circ)$. Clearly, there is good agreement between the FE-BI results and data based on the BOR formulation.

The previous comparisons serve to validate the formulation. Having done so, it is instructive to examine the effect that curvature has on the scattering properties of cavity-backed patch antennas. Consider a 2 cm × 3 cm patch residing on a 5 cm × 6 cm × 0.07874 cm cavity that is filled with a dielectric having $\epsilon_r = 2.17$. The cylinder has a radius of 15.28 cm. Figs.

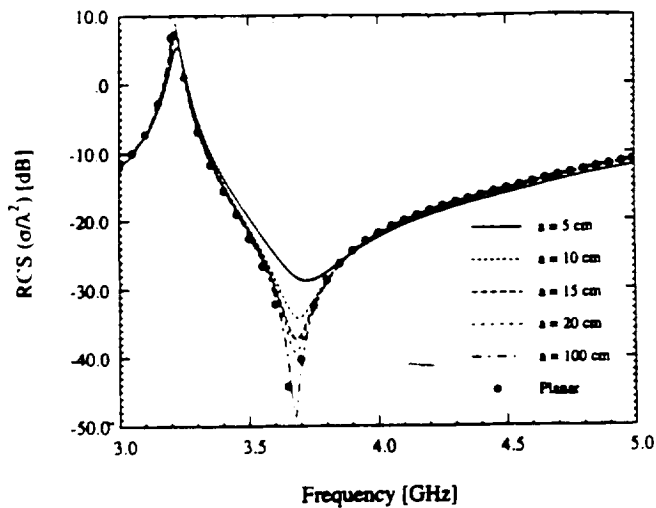


Fig. 7. RCS frequency response for a $2 \text{ cm} \times 3 \text{ cm}$ patch residing in a $5 \text{ cm} \times 6 \text{ cm} \times 0.07874 \text{ cm}$ cavity with $\epsilon_r = 2.17$ as a function of curvature for E-polarization ($\alpha = 0^\circ$).

and 8 illustrate the behavior of this geometry as a function of frequency and curvature.

Evidently, the resonance behavior of this patch is sensitive to curvature for both principal polarizations. The frequency response for E-polarization is more sensitive to curvature since the radiating surface field component is parallel to the long side of the patch and cavity. If the patch and cavity were oriented so that the long side is in the ϕ direction, the response to H-polarization would exhibit greater sensitivity. Such an effect is important to low observable antenna designers since they want to operate the antenna in the region of lowest RCS. This low return region is a consequence of delicate cancellations due to the physical layout of the aperture. Such cancellations are not as complete for highly curved structures as they are for planar cavities.

Conformal antenna designers often use wraparound antennas to achieve omnidirectional coverage. Two different configurations are typically used: a continuous cavity where the cavity is filled with a single continuous collar of dielectric, and discrete cavities symmetrically placed around the circumference of the cylinder. These two configurations are shown in Fig. 9.

Since near resonance the radiation properties of these two types of antennas are similar, any RCS advantage one might possess could govern the appropriate choice of arrays. Fig. 10 compares the E-polarized monostatic scattering at 3 GHz in the $\theta = 90^\circ$ plane for a wraparound cavity and four discrete cavities, where the patches and cavities are identical to those used in the previous example. The radius of the cylinder is 15.28 cm, and the four patches are centered at 0° , 90° , 180° , and 270° . Not surprisingly, the wraparound structure has a higher return due to coupling within the substrate. However, since in this case the scattered field is due to the z component of the surface field (ϕ -directed magnetic currents), both cavities yield large scattered fields in the four directional lobes. Fig. 11 is the corresponding comparison for H-polarization.

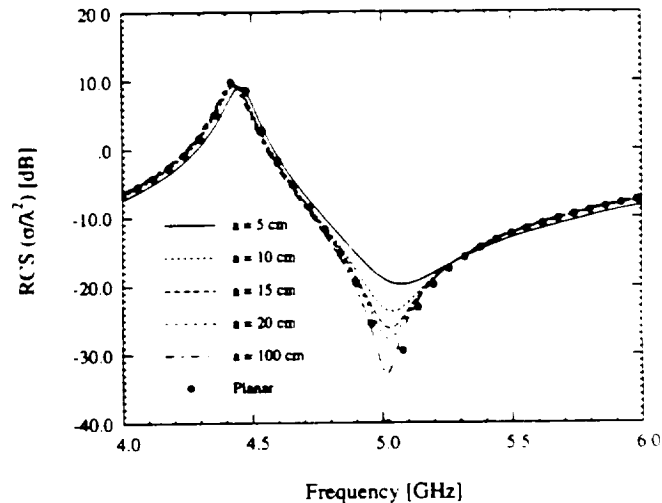


Fig. 8. RCS frequency response for a $2 \text{ cm} \times 3 \text{ cm}$ patch residing in a $5 \text{ cm} \times 6 \text{ cm} \times 0.07874 \text{ cm}$ cavity with $\epsilon_r = 2.17$ as a function of curvature for H-polarization ($\alpha = 90^\circ$).

In this case, the scattered field is attributed to the ϕ component of the surface fields (z -directed magnetic currents). Therefore, substrate modes diffract near the patch, resulting in discrete lobes for the discrete array while creeping waves shed isotropically for the continuous wraparound cavity. Low observable designs will favor discrete cavity arrays over continuous cavities since the scattering may be channeled in preferred directions and the overall scattering level is consistently lower. A final example is shown in Fig. 12, where we observe that other than the expected higher scattering from the wraparound cavity, the scattering behavior of the two arrays is very similar.

VI. CONCLUSIONS

In this paper, we have presented a finite element-boundary (FE-BI) integral technique suitable for electromagnetic scattering calculations involving cavities embedded within a circular, metallic cylinder. This formulation is analogous to the FE-BI approach used by Jin and Volakis [1], [5], [6] and may accordingly be used for the analysis of scattering by a large array of cavity-backed patch antennas. These cavities need not be identical, periodically spaced, or homogeneously filled and may in fact possess lumped impedance loads or surface metallization layers. The FE approach employs vector finite elements that properly represent the electromagnetic fields and possess high geometrical fidelity for cylindrical-rectangular cavities. Such elements were presented and are analogous to the bricks used for modeling rectangular cavities. In addition, we presented an efficient method for evaluating the on-surface and far-zone dyadic Green's functions. The presented formulation is amenable to solution using the BiCG-FFT method provided uniform zoning is used across the aperture, and as a consequence this implementation has low computational and memory demand. We have presented some validation of this work with appropriate limiting cases that provides further archival reference data. In addition, we showed how this formulation may be used to influence conformal antenna designs.

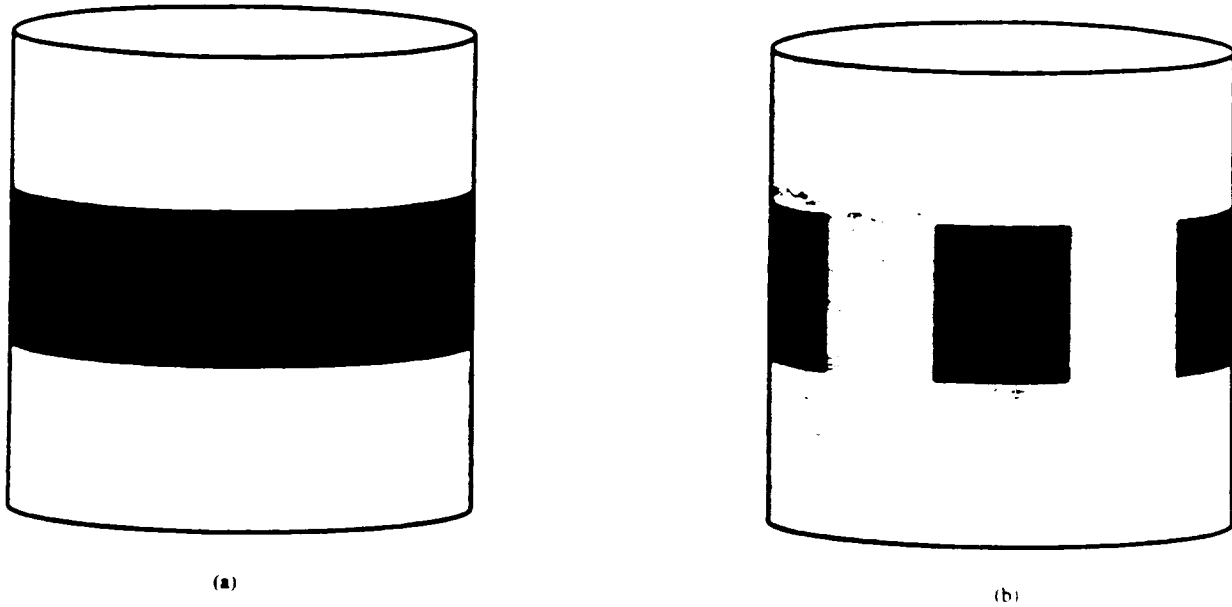


Fig. 9. Illustration of two types of arrays: (a) continuous wraparound array; (b) discrete wraparound cavity array.

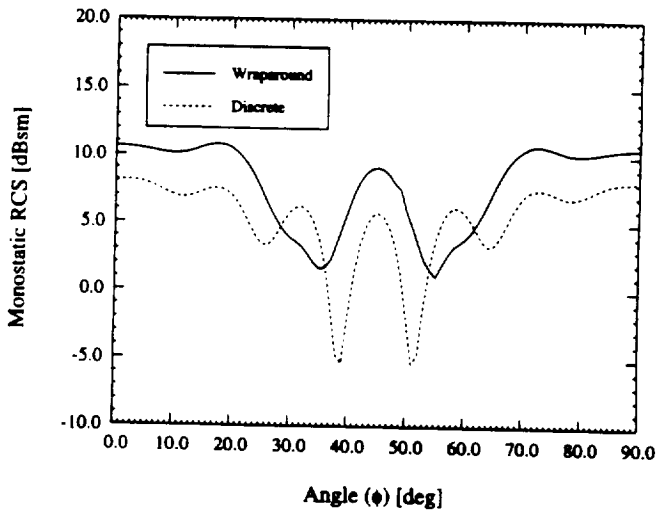


Fig. 10. Comparison of E-polarized monostatic RCS at 3 GHz for a four-patch array placed on a wraparound collar or in four discrete cavities. The cylinder radius is 15.28 cm. The patches and cavities are identical to the one used in Fig. 7. The observation plane is $\theta = 90^\circ$.

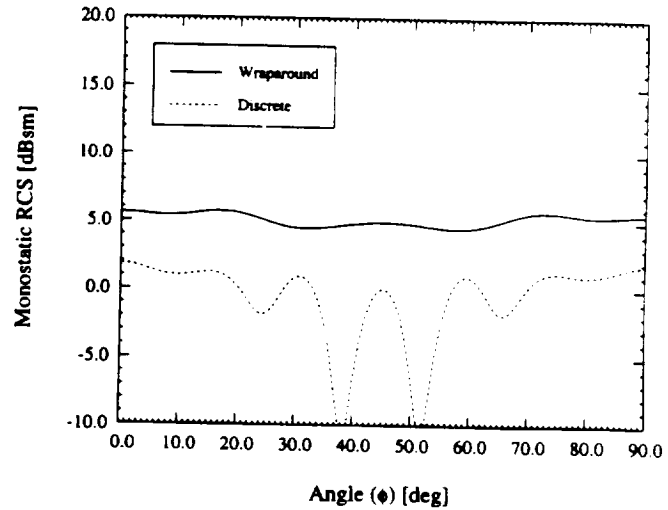


Fig. 11. Comparison of H-polarized monostatic RCS at 3 GHz for a four patch array placed on a wraparound collar or in four discrete cavities. The cylinder radius is 15.28 cm. The patches and cavities are identical to the one used in Fig. 8. The observation plane is $\theta = 90^\circ$.

APPENDIX:
FOCK FUNCTIONS

The asymptotic form of the dyadic Green's function with observation both on the surface of the cylinder and in the far field involves Fock functions. These have been extensively studied and tabulated by Logan [13]. The numerical evaluation of these functions is performed for either small arguments or large arguments.

The on-surface Fock functions used in this paper are

$$v(\xi) = \frac{1}{2} e^{j\pi/4} \sqrt{\frac{\xi}{\pi}} \int_{-\infty}^{\infty} \frac{w_2(\tau)}{w_2'(\tau)} e^{-j\xi\tau} d\tau$$

$$u(\xi) = e^{j3\pi/4} \frac{\xi^{3/2}}{\sqrt{\pi}} \int_{-\infty}^{\infty} \frac{w_2'(\tau)}{w_2(\tau)} e^{-j\xi\tau} d\tau \quad (\text{A-1})$$

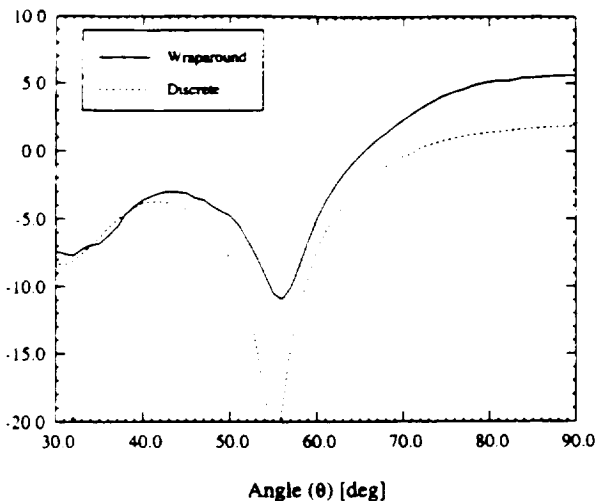
where $w_2(\tau)$ and its derivative $w_2'(\tau)$ denote Airy functions of the Second Kind. For small arguments ($\xi < 0.6$), the asymptotic expansion of (A-1) is given by

$$v(\xi) \sim 1.0 - \frac{\sqrt{\pi}}{4} \xi^{3/2} + j \frac{7}{60} \xi^3 + \frac{7}{512} \sqrt{\pi} e^{-j\pi/4} \xi^{5/2} + \dots$$

$$u(\xi) \sim 1.0 - \frac{\sqrt{\pi}}{2} e^{-j\pi/4} \xi^{3/2} + j \frac{5}{12} \xi^3 + \frac{5}{64} \sqrt{\pi} e^{-j\pi/4} \xi^{5/2} + \dots \quad (\text{A-2})$$

while a rapidly converging residue series is used for $\xi > 0.6$:

$$v(\xi) \sim e^{-j\pi/4} \sqrt{\pi \xi} \sum_{n=1}^{10} (\tau_n')^{-1} e^{-j\xi\tau_n'}$$



12. Comparison of H-polarized monostatic scattering at 3 GHz by a patch array placed on a wraparound collar or in four discrete cavities. cylinder radius is 15.28 cm. The patches and cavities are identical to the used in Fig. 8. The observation plane is $\phi = 0^\circ$.

TABLE I

Table B-1		
Zeros of the $w_2(\tau)$ and $w_2'(\tau)$		
$\tau_n = \tau_n e^{-j\frac{\pi}{3}}$ and $\tau_n' = \tau_n' e^{-j\frac{\pi}{3}}$		
n	$ \tau_n $	$ \tau_n' $
1	2.33811	1.011879
2	4.08795	3.24819
3	5.52056	4.82010
4	6.78661	6.16331
5	7.94413	7.37218
6	9.02265	8.48849
7	10.0402	9.53545
8	11.0085	10.5277
9	11.9300	11.4751
10	12.8288	12.3848

$$u(\xi) \sim 2e^{j\frac{\pi}{4}} \sqrt{\pi} \xi^{\frac{1}{2}} \sum_{n=1}^{10} (\tau_n)^{-1} e^{-j\xi\tau_n} \quad (\text{A-3})$$

where τ_n and τ_n' are zeros of $w_2(\tau)$ and $w_2'(\tau)$, respectively. These zeros are given in Table I.

The far-zone Fock functions are given by

$$\begin{aligned} g^{(l)}(\xi) &= \frac{j^l}{\sqrt{\pi}} \int_{\Gamma} \frac{e^{j\xi\tau}}{w_1(\tau)} d\tau \\ f^{(l)}(\xi) &= \frac{j^l}{\sqrt{\pi}} \int_{\Gamma} \frac{e^{j\xi\tau}}{w_1'(\tau)} d\tau \\ G^{(l)}(\xi) &= g^{(l)}(\xi) e^{j\frac{\xi^3}{3}} \\ F^{(l)}(\xi) &= f^{(l)}(\xi) e^{j\frac{\xi^3}{3}} \end{aligned} \quad (\text{A-4})$$

where $w_1(\tau)$ and its derivative $w_1'(\tau)$ denote Airy functions of First Kind and the integration contour is given by Logan [1]. These functions, $g^{(0)}(\xi)$, $g^{(1)}(\xi)$, and $f^{(0)}(\xi)$, may be

TABLE II

Table B-2			
Constants for (A-5) and (A-6)			
m	$c(m)$	$\alpha'(m)$	$Ai(m)$
1	0.7473831	1.01879297	0.5356566
2	-0.6862081	3.2481975	-0.41901548
3	-2.9495325	4.82009921	0.38040647
4	-3.4827075	6.16330736	-0.35790794
5	8.9378967	7.37217726	0.34230124
6	56.1946214	8.48848673	-0.33047623
7		9.53544905	0.32102229
8		10.52766040	-0.31318539
9		11.47505663	0.30651729
10		12.38478837	-0.30073083

calculated using

$$\begin{aligned} g^{(0)}(\xi) &= 2.0e^{-j\frac{\xi^3}{3}} \quad \xi < -1.3 \\ &= 1.39937 + \sum_{m=1}^6 \frac{c(m)}{m!} (\kappa\xi)^m \quad -1.3 \leq \xi \leq 0.5 \\ &= \sum_{m=1}^{10} \frac{e^{[\kappa\alpha'(m)\xi]}}{\alpha'(m)Ai(m)} \quad 0.5 < \xi \leq 4.0 \\ &= 1.8325e^{[-(0.8823-j0.5094)\xi-j\frac{\xi^3}{3}]} \quad \xi > 4.0 \quad (\text{A-5}) \end{aligned}$$

$$\begin{aligned} g^{(1)}(\xi) &= -j2.0 \left(\xi^2 + j\frac{0.25}{\xi} - \frac{0.25}{\xi^4} \right) e^{-j\frac{\xi^3}{3}} \quad \xi < -2.8 \\ &= \sum_{m=1}^6 \frac{c(m)\kappa^m}{m!} (\xi)^{m-1} \quad -2.8 \leq \xi \leq 0.5 \\ &= \kappa \sum_{m=1}^{10} \frac{e^{[\kappa\alpha(m)\xi]}}{Ai(m)} \quad 0.5 < \xi \leq 4.0 \\ &= -1.8325(0.8823 - j0.5094 + j\xi^2) \\ &\quad \cdot e^{[-(0.8823-j0.5094)\xi-j\frac{\xi^3}{3}]} \quad \xi > 4.0 \quad (\text{A-6}) \end{aligned}$$

$$\begin{aligned} f^{(0)}(\xi) &= j2\xi \left(1 - \frac{0.25}{\xi^3} + \frac{0.5}{\xi^6} \right) e^{-j\frac{\xi^3}{3}} \quad \xi < -1.1 \\ &= 0.77582 + e^{-j\pi/3} \sum_{m=1}^6 \frac{c(m)}{m!} (\kappa\xi)^m \quad -1.1 \leq \xi \leq 0.5 \\ &= e^{-j\pi/3} \sum_{m=1}^{10} \frac{e^{[\kappa\alpha(m)\xi]}}{Ai'(m)} \quad 0.5 < \xi \leq 4.0 \\ &= 0.0 \quad \xi > 4.0 \end{aligned} \quad (\text{A-7})$$

with constant $\kappa = e^{-j5\pi/6}$ and the coefficients for (A-5) and (A-6) given in Table II.

The corresponding constants for (A-7) are given as shown in Table III.

TABLE III

Table B-3 Constants for (A-7)			
m	c(m)	α(m)	A _i (m)
1	1.146730417	2.33810741	0.70121082
2	0.86284558	4.08794944	-0.80311137
3	-2.0192636	5.52055983	0.86520403
4	-9.977776	6.78670809	-0.91085074
5	-14.59904	7.94413359	0.94733571
6	49.0751	9.02265085	-0.97792281
7		10.04017434	1.00437012
8		11.00852430	-1.02773869
9		11.93601556	1.04872065
10		12.82877675	-1.06779386

FE MATRIX ENTRIES

The matrix entries for the FE portion of the system (5) are given in this appendix assuming that the cylindrical shell elements (4) are used in (6). These integrals are given by

$$\begin{aligned}
 I_{\rho\rho}^{(1)} &= \frac{\tilde{s}_s \tilde{s}_t}{(\alpha h)^2} \left[\rho_b^2 h \ln \left(\frac{\rho_b}{\rho_a} \right) \int_{\phi_i}^{\phi_r} (\phi - \tilde{\phi}_s)(\phi - \tilde{\phi}_t) d\phi \right. \\
 &\quad \left. + \frac{\alpha}{2} \left(\frac{\rho_b^2}{\rho_a^2} - 1 \right) \int_{z_b}^{z_t} (z - \tilde{z}_s)(z - \tilde{z}_t) dz \right] \\
 I_{\rho\phi}^{(1)} &= -\frac{\tilde{s}_s \tilde{s}_t}{th^2} \left[2\rho_b \ln \left(\frac{\rho_b}{\rho_a} \right) + \tilde{\rho}_t \left(1 - \frac{\rho_b}{\rho_a} \right) \right] \\
 &\quad \cdot \int_{z_b}^{z_t} (z - \tilde{z}_s)(z - \tilde{z}_t) dz \\
 r_{\rho z}^{(1)} &= -\frac{\tilde{s}_s \tilde{s}_t \rho_b}{\alpha^2} \int_{\phi_i}^{\phi_r} (\phi - \tilde{\phi}_s)(\phi - \tilde{\phi}_t) d\phi \\
 r_{\phi\phi}^{(1)} &= \frac{\tilde{s}_s \tilde{s}_t \alpha}{(th)^2} \left[h \left(\frac{1}{4} (\rho_b^4 - \rho_a^4) \right. \right. \\
 &\quad \left. \left. + \frac{1}{3} (\tilde{\rho}_s + \tilde{\rho}_t) (\rho_a^3 - \rho_b^3) + \frac{1}{2} \tilde{\rho}_s \tilde{\rho}_t (\rho_b^2 - \rho_a^2) \right) \right. \\
 &\quad \left. + \left(2(\rho_b^2 - \rho_a^2) - 2t(\tilde{\rho}_s + \tilde{\rho}_t) + \tilde{\rho}_s \tilde{\rho}_t \ln \left(\frac{\rho_b}{\rho_a} \right) \right) \right. \\
 &\quad \left. \cdot \int_{z_b}^{z_t} (z - \tilde{z}_s)(z - \tilde{z}_t) dz \right] \\
 r_{zz}^{(1)} &= -\frac{\tilde{s}_s \tilde{s}_t}{t^2} \int_{\rho_a}^{\rho_b} (\rho - \tilde{\rho}_s)(\rho - \tilde{\rho}_t) d\rho \\
 I_{zz}^{(1)} &= \frac{\tilde{s}_s \tilde{s}_t h}{(t\alpha)^2} \left[\alpha \left(\frac{1}{2} (\rho_b^2 - \rho_a^2) - t(\tilde{\rho}_s + \tilde{\rho}_t) + \tilde{\rho}_s \tilde{\rho}_t \ln \left(\frac{\rho_b}{\rho_a} \right) \right) \right. \\
 &\quad \left. + \frac{1}{2} (\rho_b^2 - \rho_a^2) \int_{\phi_i}^{\phi_r} (\phi - \tilde{\phi}_s)(\phi - \tilde{\phi}_t) d\phi \right] \\
 r_{zz}^{(1)} &= \frac{\tilde{s}_s \tilde{s}_t \rho_b^2}{(\alpha h)^2} \ln \left(\frac{\rho_b}{\rho_a} \right) \int_{\phi_i}^{\phi_r} (\phi - \tilde{\phi}_s)(\phi - \tilde{\phi}_t) d\phi \\
 &\quad \cdot \int_{z_b}^{z_t} (z - \tilde{z}_s)(z - \tilde{z}_t) dz \\
 r_{zz}^{(1)} &= \frac{\tilde{s}_s \tilde{s}_t \alpha}{(th)^2} \left[\frac{1}{4} (\rho_b^4 - \rho_a^4) + \frac{1}{3} (\tilde{\rho}_s + \tilde{\rho}_t) (\rho_a^3 - \rho_b^3) \right. \\
 &\quad \left. + \frac{1}{2} \tilde{\rho}_s \tilde{\rho}_t (\rho_b^2 - \rho_a^2) \right] \times \int_{z_b}^{z_t} (z - \tilde{z}_s)(z - \tilde{z}_t) dz
 \end{aligned}$$

$$\begin{aligned}
 I_{zz}^{(2)} &= \frac{\tilde{s}_s \tilde{s}_t h}{(t\alpha)^2} \left[\frac{1}{4} (\rho_b^4 - \rho_a^4) + \frac{1}{3} (\tilde{\rho}_s + \tilde{\rho}_t) (\rho_a^3 - \rho_b^3) \right. \\
 &\quad \left. + \frac{1}{2} \tilde{\rho}_s \tilde{\rho}_t (\rho_b^2 - \rho_a^2) \right] \times \int_{\phi_i}^{\phi_r} (\phi - \tilde{\phi}_s)(\phi - \tilde{\phi}_t) d\phi
 \end{aligned} \tag{B-1}$$

Each of the above unevaluated integrals is of the form

$$\begin{aligned}
 \int_L^U (\xi - \tilde{\xi}_s)(\xi - \tilde{\xi}_t) d\xi &= \frac{1}{2} (U^2 - L^2) (\tilde{\xi}_t - \tilde{\xi}_s) \\
 &\quad + \frac{1}{3} (U^3 - L^3) - \tilde{\xi}_s \tilde{\xi}_t (U - L)
 \end{aligned} \tag{B-2}$$

The integrals $I_{st}^{(1),(2)}$ are used in the assembly of the FE portion ($[A]$) of the system.

REFERENCES

- [1] J.-M. Jin and J. L. Volakis, "A hybrid finite element method for scattering and radiation by microstrip patch antennas and arrays residing in a cavity," *IEEE Trans. Antennas Propagat.*, vol. 39, no. 11, pp. 1598-1604, Nov. 1991.
- [2] J. L. Volakis, A. Chatterjee, and J. Gong, "A class of hybrid finite element methods for electromagnetics: A review," to appear in *J. Electromagn. Waves Appl.*, 1994.
- [3] Z. J. Cendes, "Vector finite elements for electromagnetic field computation," *IEEE Trans. Magn.*, vol. 27, no. 5, pp. 3958-3966, Sept. 1991.
- [4] A. Bossavit, "A rationale for edge-elements in 3D fields computations," *IEEE Trans. Magn.*, vol. 24, no. 1, pp. 74-79, Jan. 1988.
- [5] J.-M. Jin and J. L. Volakis, "A finite element-boundary integral formulation for scattering by three-dimensional cavity-backed apertures," *IEEE Trans. Antennas Propagat.*, vol. 39, no. 1, pp. 97-104, Jan. 1991.
- [6] ———, "Electromagnetic scattering by and transmission through a three-dimensional slot in a thick conducting plane," *IEEE Trans. Antennas Propagat.*, vol. 39, no. 4, pp. 543-550, Apr. 1991.
- [7] A. Chatterjee, J.-M. Jin, and J. L. Volakis, "Computation of cavity resonances using edge-based finite elements," *IEEE Trans. Microwave Theory Tech.*, vol. 40, no. 11, pp. 2106-2108, Nov. 1992.
- [8] C.-T. Tai, *Dyadic Green's Functions in Electromagnetic Theory*. Scranton, PA: International Textbook, 1971.
- [9] P. H. Pathak and N. N. Wang, "An analysis of the mutual coupling between antennas on a smooth convex surface," Ohio State Univ. ElectroScience Lab., Rep. 784583-7, Oct. 1978.
- [10] J. Boersma and S. W. Lee, "Surface field due to a magnetic dipole on a cylinder: Asymptotic expansions of exact solution," Univ. Illinois Electromagnetics Lab., Rep. 78-17, 1978.
- [11] T. S. Bird, "Comparison of asymptotic solutions for the surface field excited by a magnetic dipole on a cylinder," *IEEE Trans. Antennas Propagat.*, vol. 32, no. 11, pp. 1237-1244, Nov. 1984.
- [12] ———, "Accurate asymptotic solution for the surface field due to apertures in a conducting cylinder," *IEEE Trans. Antennas Propagat.*, vol. 33, no. 10, pp. 1108-1117, Oct. 1985.
- [13] N. A. Logan, "General research in diffraction theory," Lockheed Aircraft Corp., Missiles and Space Div., vol. 1 and 2, Rep. LMSD-288088, Dec. 1959.
- [14] O. Einarsson, R. E. Kleinman, P. Laurin, and P. L. E. Uslenghi, "Studies in radar cross sections L—Diffraction and scattering by regular bodies IV: The circular cylinder," Univ. of Michigan, Tech. Rep. 7133-3-T, 1966.
- [15] A. S. Gorianov, "An asymptotic solution of the problem of diffraction of a plane electromagnetic wave by a conducting cylinder," *Radio Eng. Electron. Phys.*, vol. 3, pp. 23-39, 1958. (English translation of *Radiotekhnika i Elektronika*, vol. 3)
- [16] T. K. Sarkar, "On the application of the generalized biconjugate gradient method," *J. Electromagn. Waves Appl.*, vol. 1, no. 3, pp. 223-242, 1987.
- [17] C. F. Smith, A. F. Peterson, and R. Mittra, "The biconjugate gradient method for electromagnetic scattering," *IEEE Trans. Antennas Propagat.*, vol. 38, no. 6, pp. 938-940, June 1990.



Leo C. Kempel (S'89) was born on October 30, 1965, in Akron, OH. He participated in the cooperative education program from January 1986 to September 1989 with General Dynamics/Fort Worth Div. and received the BSEE degree from the University of Cincinnati, Cincinnati, OH, in 1989. He received the MSEE degree and the Ph.D. degree from the University of Michigan in 1990 and 1994, respectively.

Since September 1989 he has been associated with the Radiation Laboratory at the University of Michigan as a Graduate Student Research Assistant. He is currently a Senior Electrical Engineer with Mission Research Corp. Combat Applications Group, Valparaiso, FL. His research interests include analytical and computational electromagnetics as applied to scattering and radiation problems.

Dr. Kempel is a member of Tau Beta Pi and Eta Kappa Nu.

John L. Volakis (S'77-M'82-SM'89), for a photograph and biography, please see p. 1242 of this issue of this TRANSACTIONS.

A Hybrid Finite Element–Boundary Integral Method for the Analysis of Cavity-Backed Antennas of Arbitrary Shape

Jian Gong, *Student Member, IEEE*, John L. Volakis, *Senior Member, IEEE*, A. C. Woo, and H. T. G. Wang

Abstract—An edge-based hybrid finite element-boundary integral (FE-BI) formulation using tetrahedral elements is described for scattering and radiation analysis of arbitrarily shaped cavity-backed patch antennas. By virtue of the finite element method (FEM), the cavity irregularities, the dielectric super/substrate inhomogeneities, and the diverse excitation schemes inside the cavity may be readily modeled when tetrahedral elements are used to discretize the cavity. On the aperture, the volume mesh reduces to a triangular grid allowing the modeling of nonrectangular patches. Without special handling of the boundary integral system, this formulation is typically applicable to cavity-backed antenna systems with moderate aperture size. To retain an $O(N)$ memory requirement, storage of the full matrix due to the boundary integral equation is avoided by resorting to a structured triangular aperture grid and taking advantage of the integral's convolutional property. If necessary, this is achieved by overlaying a structured triangular grid on the unstructured triangular grid and relating the edge field coefficients between the two grids via two narrow banded transformation matrices. The combined linear system of equations is solved via the biconjugate gradient (BiCG) method, and the FFT algorithm is incorporated to compute the matrix-vector product efficiently, with minimal storage requirements.

I. INTRODUCTION

MICROSTRIP antennas have been extensively investigated experimentally, analytically, and numerically for decades. By and large, numerical methods have been serving the engineers and researchers in the analysis and design of these conformal antennas for many years. Among them the moment method in conjunction with various integral equation (IE) formulations played a major role [1]–[3]. However, IE methods are associated with field representations in which the appropriate Green's function for the specific geometry must be employed, and this limits their versatility. Moreover, IE techniques are usually formulated on the assumption of an infinite substrate, a model that obviously deviates from the practical configuration, leading to inaccuracies for larger bandwidth antennas. Furthermore, in the context of IE methods, antenna excitations are represented using simplified models that differ more or less from the actual configurations. Also,



Fig. 1. Illustration of a cavity-backed patch antenna and the different computational regions.

due to the singularity of the current distribution near the patch-probe junction(s), special measures must be taken [4], not to mention additional IE complexities due to possible substrate anisotropies or inhomogeneities in the antenna substructure. In contrast, the hybrid finite element–boundary integral (FE–BI) technique alleviates these difficulties, and this was demonstrated recently when the method was applied to rectangular patch antennas [5].

In this paper, we present an edge-based hybrid FE–BI formulation using tetrahedral elements for a characterization of arbitrarily shaped cavity-backed antennas. An example of such a configuration is shown in Fig. 1, where a cavity is recessed in a metallic ground plane enclosing the FEM volume and the antenna elements on the aperture may be excited by different schemes, such as a simple probe, a magnetic frill generator, a practical coaxial cable, microstrip lines, slots, or a CPW line. In the context of the FEM, the cavity is first discretized into a number of tetrahedral elements that naturally reduce to triangles on the cavity's aperture. For nonrectangular patches this triangular gridding is, in general, nonuniform, and the exact boundary integral formulation based upon this mesh applies to any patch shape. As a result, the hybrid FE–BI technique is capable of modeling arbitrarily shaped cavity-backed antenna configurations, different substrate inhomogeneities, anisotropies, and various practical excitation schemes.

As is well known, the boundary integral (BI) equation subsystem leads to a fully populated matrix whose size is determined by the number of aperture mesh edges. For large apertures, this analysis becomes impractical in terms of storage and computation time requirements, and to overcome this inefficiency a uniform zoning of the aperture is required.

Manuscript received August 27, 1993; revised March 28, 1994.

J. Gong and J. L. Volakis are with the Radiation Laboratory, University of Michigan, Ann Arbor, MI 48109-2122 USA.

A. C. Woo is with NASA Ames, Research Center, Moffett Field, CA 94035 USA.

H. T. G. Wang is with the Naval Air Warfare Center, China Lake, CA 93555 USA.

IEEE Log Number 9404515.

By resorting to the structured mesh, the boundary integral matrix can be cast into a discrete convolutional form, thus permitting the computation of the matrix-vector products via the discrete Fourier transform (DFT), avoiding a need to store the full BI matrix. This memory-saving scheme has already been applied to IE solutions involving rectangular [6], [13] and triangular [7] surface grids, and in this paper we describe how the BiCG-FFT solver is implemented for triangular meshes. The differences between the rectangular and triangular meshes are also described, and results are presented that demonstrate the method's versatility in computing the scattering and input impedance of various nonrectangular printed antennas.

II. FORMULATION

In this section, we present the edge-based hybrid FE-BI formulation using variational principles, where the matrix algebra notation is employed so that one can readily extend the formulae to the general anisotropic case. As derived in [5], the complete functional pertinent to the scattering and radiation by a cavity-backed configuration (shown in Fig. 1) may be written as

$$\begin{aligned}
 F(\mathbf{E}) = & \frac{1}{2} \iiint_V \left\{ (\nabla \times \mathbf{E}) \cdot \frac{1}{\mu_r} (\nabla \times \mathbf{E}) - k_0^2 \epsilon_r \mathbf{E} \cdot \mathbf{E} \right\} dv \\
 & + 2jk_0 Z_0 \iint_S (\mathbf{E} \times \mathbf{H}^i) \cdot \hat{z} dS + \iint_V \mathbf{E} \\
 & \cdot \left(jk_0 Z_0 \mathbf{J}_i + \nabla \times \frac{1}{\mu_r} \mathbf{M}_i \right) dv - 2k_0^2 \iint_S (\mathbf{E} \times \hat{z}) \\
 & \cdot \left\{ \iint_{S'} (\mathbf{E} \times \hat{z}) \cdot \left(\bar{\mathbf{I}} + \frac{1}{k_0^2} \nabla \nabla \right) G_0(\mathbf{r}, \mathbf{r}') dS' \right\} dS
 \end{aligned} \quad (1)$$

where \mathbf{J}_i and \mathbf{M}_i represent interior electric and magnetic current sources within the cavity V ; \mathbf{H}^i is the incident field, if any, from the exterior region; the surface S encompasses the cavity aperture excluding the portion occupied by the antenna elements; ϵ_r and μ_r denote, respectively, the relative permittivity and permeability; k_0 is the free space wave number, $\bar{\mathbf{I}}$ the unit dyad, and $G_0(\mathbf{r}, \mathbf{r}')$ the free space Green's function with \mathbf{r} and \mathbf{r}' denoting the observation and integration points.

A. Cavity Volume Modeling

In proceeding with the discretization of (1), it is convenient to reexpress it as

$$F = F_V + F_S \quad (2)$$

where F_V denotes the volume integral contributions and, similarly, F_S accounts for the surface integral contributions. The cavity volume is subdivided into N tetrahedral elements V_e ($e = 1, 2, \dots, N$), and within each tetrahedron the field is expanded using edge-based elements as

$$\mathbf{E} = [V]_e^T \{E\}_e \quad (3)$$

with

$$\begin{aligned}
 [V]_e &= \{ \{V_x\} \{V_y\} \{V_z\} \}, \\
 \{V_u\} &= \begin{pmatrix} V_{u1} \\ V_{u2} \\ \vdots \\ V_{un} \end{pmatrix}, \quad u = x, y, z \\
 \{E\}_e &= \begin{pmatrix} E_1 \\ E_2 \\ \vdots \\ E_6 \end{pmatrix}_e
 \end{aligned} \quad (4)$$

in which V_{un} is the u ($u = x, y$ or z) component of the volume vector basis functions along the n th edge. The unknown vector $\{E\}_e$ has six entries, one for each tetrahedron edge. (In this paper, we use square brackets for matrices and curly brackets for vectors.) Inserting (3) into (2), and taking the first variation of F_V with respect to $\{E\}_e$, yields

$$\delta F_V = \sum_e \{ [A]_e \{E\}_e + \{K\}_e \} \quad (5)$$

where

$$[A]_e = \iiint_{V_e} \left\{ \frac{1}{\mu_r} [DV]_e [DV]_e^T - k_0^2 \epsilon_r [V]_e [V]_e^T \right\} dv \quad (6)$$

$$\begin{aligned}
 \{K\}_e &= \iiint_{V_e} [V]_e \left\{ jk_0 Z_0 \begin{pmatrix} J_{ix} \\ J_{iy} \\ J_{iz} \end{pmatrix} \right. \\
 &\quad \left. + \nabla \times \frac{1}{\mu_r} \begin{pmatrix} M_{ix} \\ M_{iy} \\ M_{iz} \end{pmatrix} \right\} dv
 \end{aligned} \quad (7)$$

$$[DV]_e^T = \begin{bmatrix} \frac{\partial}{\partial y} \{V_z\} - \frac{\partial}{\partial z} \{V_y\} \\ \frac{\partial}{\partial z} \{V_x\} - \frac{\partial}{\partial x} \{V_z\} \\ \frac{\partial}{\partial x} \{V_y\} - \frac{\partial}{\partial y} \{V_x\} \end{bmatrix} \quad (8)$$

To carry out the above integrations, it remains to introduce the volume expansion or shape functions V_e . For our implementation we employed the linear edge-based shape functions for tetrahedral elements given in [8] and [9].

B. Aperture Modeling

To discretize the surface integrals in (1), the aperture is subdivided into triangular elements since these correspond to the faces of the tetrahedrals. Within each triangle, the field is represented as

$$\mathbf{E} = [S]_e^T \{E_s\}_e \quad (9)$$

where

$$\begin{aligned} \{S\}_e &= [\{S_x\} \{S_y\}]_e \\ \{S_u\} &= \begin{pmatrix} S_{u1} \\ S_{u2} \\ S_{u3} \end{pmatrix}, \quad u = x, y \\ \{E_s\}_e &= \begin{pmatrix} E_{s1} \\ E_{s2} \\ E_{s3} \end{pmatrix}_e \end{aligned} \quad (10)$$

in which S_{ui} is the u ($u = x, y$) component of the surface vector basis functions along the i th edge. On substituting (9) into the surface integrals of (2) and taking the first variation of F_S with respect to $\{E_s\}_e$, we obtain

$$\delta F_S = \sum_e \{[B]_e \{E_s\}_e + \{L\}_e\} \quad (11)$$

where

$$\begin{aligned} [B]_e &= \iint_{S_e} \iint_{S'_e} \left\{ -2k_0^2 [S_e] [S'_e]^T \right. \\ &\quad \left. + 2 \left[\frac{\partial}{\partial x} \{S_y\} - \frac{\partial}{\partial y} \{S_x\} \right] \left[\frac{\partial}{\partial x'} \{S_y\}^T - \frac{\partial}{\partial y'} \{S_x\}^T \right] \right\} \\ &\quad \cdot G_0(\mathbf{r}, \mathbf{r}') dS dS' \end{aligned} \quad (12)$$

and

$$\{L\}_e = j2k_0 Z_0 \iint_{S_e} [S_e] \begin{pmatrix} H_y^i \\ -H_x^i \end{pmatrix} dS. \quad (13)$$

Note that in (12) the elements of the array $[S_e]$ are functions of the observation vector \mathbf{r} , whereas the elements of $[S'_e]^T$ are with respect to the integration point \mathbf{r}' . A suitable set of linear edge-based surface basis functions is

$$S_i(\mathbf{r}) = \begin{cases} \frac{l_i}{2A_e} \hat{z} \times (\mathbf{r} - \mathbf{r}_i) \epsilon(\mathbf{r}) & \mathbf{r} \in S_e \\ 0 & \text{otherwise.} \end{cases} \quad (14)$$

In this expression, l_i denotes the length of the i th edge and \mathbf{r}_i is the position vector of the vertex opposite to the i th edge. Since each edge shares two triangles, one is defined as the plus and the other as the minus triangle. Therefore, $\epsilon(\mathbf{r})$ is given by

$$\epsilon(\mathbf{r}) = \begin{cases} 1 & \mathbf{r} \in S_e^+ \\ -1 & \mathbf{r} \in S_e^- \end{cases} \quad (15)$$

where $S_e = S_e^+ + S_e^-$. The constant A_e in (14) denotes the area of the plus or minus triangle depending on whether $\mathbf{r} \in S_e^+$ or $\mathbf{r} \in S_e^-$. We note that $S_i(\mathbf{r}) \times \hat{z}$ yields the basis functions used by Rao *et al.* [10] in their moment method solution of boundary integral equations.

C. System Assembly

To construct the final system for the solution of the electric field components we combine (5) and (11), and after assembly we obtain the system

$$\{[A]\{E\} + \{K\}\} + \{[B]\{E_s\} + \{L\}\} = 0. \quad (16)$$

In this, $\{K\}$ and $\{L\}$ are the excitation vectors due to the interior current sources and the exterior excitation, respectively. The unknown electric field vector $\{E\}$ consists of all field expansion coefficients with respect to the element edges except those coinciding with perfectly electrically conducting (PEC) walls, PEC antenna element(s), or PEC pins inside the cavity. Finally, the vector $\{E_s\}$ represents the unknown surface fields whose entries are part of those in $\{E\}$ with their corresponding edges on the aperture. The explicit expressions for the matrices and vectors in (16) can be readily extracted from (6), (7), and (12) (see also [11]). It is evident that $[A]$ and $[B]$ are symmetric as a result of the assumed isotropic medium and reciprocity. In addition, $[A]$ exhibits high sparsity due to the FEM formulation, whereas $[B]$ is fully populated. Two approaches may be followed in carrying out the solution of the combined subsystems when an iterative solver is employed, such as the biconjugate gradient (BiCG) method [13]. These two approaches differ in the manner used for the evaluation of matrix-vector products called for in the iteration steps. One could sum the coefficient matrices $[A]$ and $[B]$ by adding up the corresponding matrix entries prior to the execution of the BiCG algorithm, or instead the resulting vectors may be summed after carrying out the individual matrix-vector products. We observed that the first approach is more efficient in terms of computation time after reordering the combined matrix and storing only the nonzero elements. This is because, in the context of this scheme, the combination of the two matrices is performed only once outside the iteration. However, the second approach is compatible with the BiCG-FFT scheme, where the FFT algorithm is employed to exploit the convolutional property of the integral operator, thus eliminating a need to explicitly store the entire BI matrix. Below, we discuss the implementation of the matrix-vector product of the boundary integral system for the BiCG-FFT solution.

D. Implementation of the Boundary Integral Matrix Vector Products Using FFT

We refer to Fig. 2, which shows an overlay of a uniform grid over a nonuniform mesh. The boundary integral equation is implemented using the structured triangular grid, and the relation between the unstructured and structured mesh is described in the next section. We recognize that the triangular grid consists of equal right triangles and thus involves three different classes of edges (classes 1, 2, and 3). These include the x directed, y directed, and the diagonal edges, all of which are uniformly spaced. For the FFT implementation, each class of edges is independently numbered in accordance with their geometric location. Specifically, the i th class will carry the numbering (m, n) if the edge is the m th along the x direction and the n th along the y direction. The indices (m, n) take the

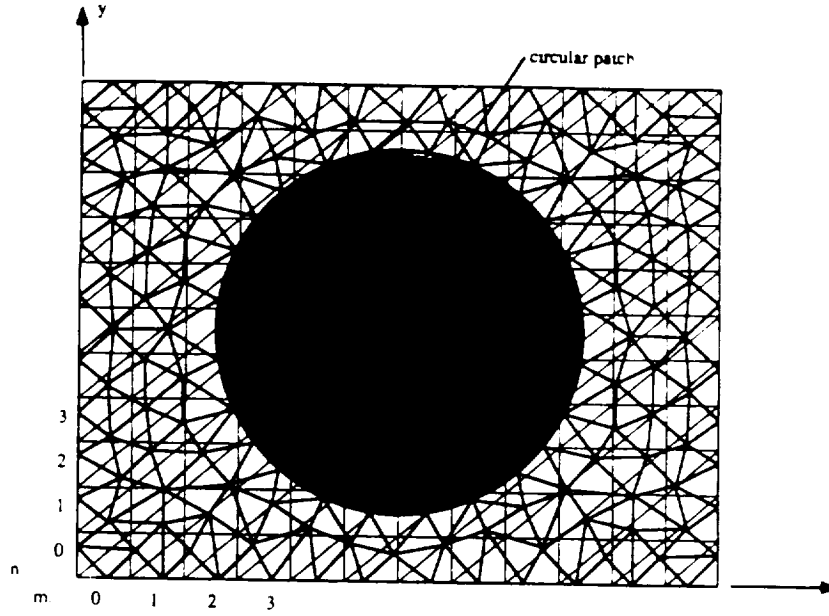


Fig. 2. Overlay of a structured triangular aperture mesh over an unstructured mesh, shown here to conform to a circular patch

values

$$\begin{aligned} m &= 0, 1, 2, \dots, M^i \\ n &= 0, 1, 2, \dots, N^i \end{aligned}$$

with $i = 1$ for the y directed edges, $i = 2$ for the diagonal edges, and $i = 3$ for the x directed edges. Consequently, we find that

$$M^i = \begin{cases} M-2 & i=1 \\ M-1 & i=2 \\ M-1 & i=3 \end{cases} \quad N^i = \begin{cases} N-1 & i=1 \\ N-1 & i=2 \\ N-2 & i=3 \end{cases} \quad (17)$$

where M and N denote the numbers of elements along the x and y directions, respectively.

To perform the integrations for the evaluation of the boundary integral matrix elements, it is now convenient to rewrite the basis functions (14) in terms of the new indices (m, n) . We readily find that the edge-based basis functions associated with each of the aforementioned class of edges can be rewritten as shown in (18)–(20) at the bottom of the page, where the superscripts refer to the edge class. Each entry of the boundary

matrix–vector product can now be calculated as

$$\begin{aligned} \{\text{BI subsystem}\} &= \{B\}\{E_s\} \\ &= \sum_{j=1}^3 \left[\sum_{m'=0}^{M^j} \sum_{n'=0}^{N^j} B_{mn,m'n'}^{ij} E_{m'n'}^j \right] \end{aligned} \quad (21)$$

in which (m, n) are the geometric location indices for the i th class observation edges, whereas (m', n') are the same for the j th class edges belonging to integration elements. Thus, the specification of the indices $i, m,$ and n completely defines the entry $k_i = nM^i + M$ of the column resulting after the execution of the boundary matrix–vector product. It is readily found that

$$\begin{aligned} B_{mn,m'n'}^{ij} &= \\ &= -2k_0^2 \iint_{S_r} \iint_{S_r'} S_{mn}^i \cdot S_{m'n'}^j G_0(\mathbf{r}, \mathbf{r}') dx dy dr' dy' \\ &+ \frac{8}{(\Delta x \Delta y)^2} \iint_{S_r} \iint_{S_r'} \epsilon_i(\mathbf{r}) \epsilon_j(\mathbf{r}') l_i l_j \\ &G_0(\mathbf{r}, \mathbf{r}') dx dy dr' dy' \end{aligned} \quad (22)$$

$$S_{mn}^1(x, y) = \frac{1}{\Delta x} \begin{cases} (n\Delta y - y)\hat{x} + (x - m\Delta x)\hat{y} & (x, y) \in S_r^+ \\ (y - (n+1)\Delta y)\hat{x} + ((m+2)\Delta x - x)\hat{y} & (x, y) \in S_r^- \\ 0 & \text{otherwise.} \end{cases} \quad (18)$$

$$S_{mn}^2(x, y) = \frac{\sqrt{(\Delta x)^2 + (\Delta y)^2}}{\Delta x \Delta y} \begin{cases} (n\Delta y - y)\hat{x} + (x - (m+1)\Delta x)\hat{y} & \in S_r^+ \\ (y - (n+1)\Delta y)\hat{x} + (m\Delta x - x)\hat{y} & \in S_r^- \\ 0 & \text{otherwise.} \end{cases} \quad (19)$$

$$S_{mn}^3(x, y) = \frac{1}{\Delta y} \begin{cases} ((n+2)\Delta y - y)\hat{x} + (x - (m+1)\Delta x)\hat{y} & (x, y) \in S_r^+ \\ (y - n\Delta y)\hat{x} + (m\Delta x - x)\hat{y} & (x, y) \in S_r^- \\ 0 & \text{otherwise.} \end{cases} \quad (20)$$

with

$$l_i = \begin{cases} \Delta y & i = 1 \\ \sqrt{(\Delta x)^2 + (\Delta y)^2} & i = 2 \\ \Delta x & i = 3. \end{cases} \quad (23)$$

More important, it can be shown that the BI subsystem exhibits the convolutional property $B_{mn,m'n'}^{ij} = B_{(m-m'),(n-n')}^{ij}$, and thus we can rewrite (21) as

$$[B]\{E_s\} = \sum_{j=1}^3 B^{ij} * E^j \quad (24)$$

where the $*$ denotes convolution. It is now seen that the computation of the boundary matrix-vector product can be performed by employing the 2-D discrete Fourier transform (DFT), thus avoiding a need to store the BI matrix other than those entries that are unique. When the symmetry property of $B_{(m-m'),(n-n')}^{ij}$ is also invoked, implying

$$B_{(m-m'),(n-n')}^{ij} = B_{(m'-m),(n'-n)}^{ji} \quad (25)$$

it is concluded that the total nonredundant entries in the BI matrix are

$$N_p = \sum_{i=1}^3 \sum_{j=1}^3 N^i (M^i + M^j - 1). \quad (26)$$

This should be compared to the $(\sum_{i=1}^3 M^i N^i)^2$ entries whose storage would normally be required if the BI system was not cast in convolutional form. We remark that N_p is nevertheless equal to twice the number of entries required for uniform rectangular grids [6] for one class of edges. To avoid aliasing, it is necessary that $B_{(m-m'),(n-n')}^{ij} = B_p^{ij}(\tilde{m}, \tilde{n})$ be cast in a 2-D array that has the usual periodic form, and zero padding may also be required to make use of the standard FFT routines. Specifically, the matrix-vector product (21) is executed by using the MFT \times NFT array (27), shown at the bottom of the page, with the corresponding field vector given by

$$E_p^j(\tilde{m}, \tilde{n}) = \begin{cases} E^j(\tilde{m}, \tilde{n}) & 0 < \tilde{m} < M^j, \quad 0 < \tilde{n} < N^j \\ 0 & \text{otherwise.} \end{cases} \quad (28)$$

and MFT and NFT must be powers of 2 if a radix 2 FFT algorithm is used.

In the BiCG-FFT algorithm the BI subsystem vector is computed as

$$\{\text{BI subsystem}\} = \sum_{i=1}^3 \hat{S} \{ \text{DFT}^{-1} \{ \text{DFT} \{ B_p^{ij} \} \cdot \text{DFT} \{ E_i^j \} \} \}. \quad (29)$$

The presence of the operator \hat{S} indicates the necessary reordering of the 2-D array that results after the inverse FFT operation into a single column with the proper indexing for addition to the FEM subsystem. It should be remarked that in contrast to [7] the integrals (22) are evaluated without introducing any approximation. This is necessary to preserve the global combined system symmetry.

III. MESH OVERLAY SCHEME FOR NONRECTANGULAR PATCHES

As described above, the BiCG-FFT solver requires uniform aperture gridding so that the BI subsystem can be put in block circulant form. This can always be achieved during mesh generation whenever the patches are rectangular in shape or in case of radiators that are placed at some distance (usually small) below the aperture. However, for circular, triangular, or other nonrectangular patches on the aperture, it is not possible to construct a uniform mesh using the mesh generator. Typically, the aperture mesh is necessary to conform to the patch shape, leading to an unstructured free surface grid. In this case, to make use of the efficient, low-memory BiCG-FFT algorithm, an approach is proposed to overlay on the unstructured aperture grid another coincident structured grid, as shown in Fig. 2. The boundary integral subsystem is then constructed using the overlaid uniform grid, whose edge fields can be related to those on the unstructured grid via two sparse transformation matrices. That is, it is necessary to append to the system (16) the relations

$$\begin{aligned} \{E_s\}_u &= [T_F] \{E_s\}_{nu} \\ \{E_s\}_{nu} &= [T_B] \{E_s\}_u \end{aligned} \quad (30)$$

where the subscripts u and nu refer to the field coefficients of the uniform and nonuniform aperture grids, respectively. Also, $[T_F]$ and $[T_B]$ refer to the forward and backward transformation matrices, respectively, with N_u and N_{nu} denoting the numbers of the uniform and nonuniform mesh edges on the cavity aperture.

$$B_p^{ij}(\tilde{m}, \tilde{n}) = \begin{cases} B^{ij}(-\tilde{m}, -\tilde{n}), & 0 < \tilde{m} < M^i, \quad 0 < \tilde{n} < N^j \\ B^{ij}(-\tilde{m}, -\tilde{n}), & \text{MFT} - M^i + 1 < \tilde{m} < \text{MFT} \\ & 0 < \tilde{n} < N^j \\ B^{ij}(\tilde{m}, \tilde{n} - 1 - \text{NFT}), & 0 < \tilde{m} < M^i, \\ & \text{NFT} - N^j + 1 < \tilde{n} < \text{NFT} \\ B^{ij}(\tilde{m} - 1 - \text{MFT}, \tilde{n} - 1 - \text{NFT}), & \text{MFT} - M^i + 1 < \tilde{m} < \text{MFT} \\ & \text{NFT} - N^j + 1 < \tilde{n} < \text{NFT} \\ 0 & \text{otherwise.} \end{cases} \quad (27)$$

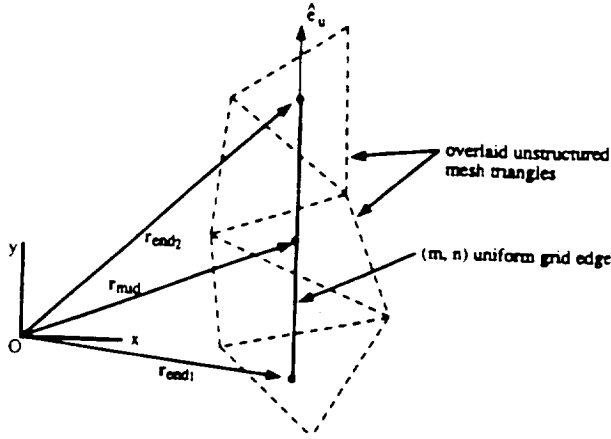


Fig. 3. Illustration of the parameters and geometry used in constructing the transformation matrix elements between the structured and unstructured mesh.

To derive the elements of $[T_F]$, we begin with the expansion (9) and enforce it at three points on each edge belonging to the uniform grid. We conveniently place these three points at the center and ends of the edge (see Fig. 3). Given the fields at these points, we can interpolate the field along the (m, n) edge of the uniform grid using the weighted average

$$\begin{aligned}
 (\mathbf{E}_u)_{(m,n)} = \frac{1}{2} \hat{e}_u \cdot \left\{ \frac{1}{2N_{\text{end}_1}} \sum_{k=1}^{N_{\text{end}_1}} \mathbf{E}_{nu}^k(\mathbf{r}_{\text{end}_1}) \right. \\
 + \frac{1}{N_{\text{mid}}} \sum_{k=1}^{N_{\text{mid}}} \mathbf{E}_{nu}^k(\mathbf{r}_{\text{mid}}) \\
 \left. + \frac{1}{2N_{\text{end}_2}} \sum_{k=1}^{N_{\text{end}_2}} \mathbf{E}_{nu}^k(\mathbf{r}_{\text{end}_2}) \right\} \quad (31)
 \end{aligned}$$

in which \hat{e}_u denotes the unit vector along x, y or the diagonal, depending on the class of edge being considered. The quantities \mathbf{E}_{nu}^k represent the fields in the nonuniform grid triangles with the superscript k being a sum variable in case $\mathbf{r}_{\text{end}_1}, \mathbf{r}_{\text{end}_2}$, or \mathbf{r}_{mid} specify a point shared by more than one triangle. Obviously, $N_{\text{end}_1}, N_{\text{mid}}$, and N_{end_2} denote the number of nonuniform grid triangles sharing the node at $\mathbf{r}_{\text{end}_1}, \mathbf{r}_{\text{mid}}$, and $\mathbf{r}_{\text{end}_2}$, respectively, and will typically be equal to unity.

After assembling (31) into (30), we find that the elements of the forward transformation matrix are given by

$$\begin{aligned}
 (T_F)_{ij} = \frac{1}{2} \hat{e}_u \cdot \left\{ \frac{1}{2N_{\text{end}_1}} \sum_{k=1}^{N_{\text{end}_1}} \sum_{\ell=1}^3 \epsilon_{ij\ell} \mathcal{S}_\ell^k(\mathbf{r}_{\text{end}_1}) \right. \\
 + \frac{1}{N_{\text{mid}}} \sum_{k=1}^{N_{\text{mid}}} \sum_{\ell=1}^3 \epsilon_{ij\ell} \mathcal{S}_\ell^k(\mathbf{r}_{\text{mid}}) \\
 \left. + \frac{1}{2N_{\text{end}_2}} \sum_{k=1}^{N_{\text{end}_2}} \sum_{\ell=1}^3 \epsilon_{ij\ell} \mathcal{S}_\ell^k(\mathbf{r}_{\text{end}_2}) \right\} \quad (32)
 \end{aligned}$$

in which

$$\epsilon_{ij\ell} = \begin{cases} 1 & j = j_\ell \\ 0 & \text{otherwise} \end{cases}$$

and the global indices i and j correspond to the i th uniform grid edge and the j th nonuniform grid edge. The subscript i is the global index used in numbering the nonuniform grid edges, whereas the subscript ℓ ($\ell = 1, 2$, or 3) is the local edge index used in the definition of the basis functions \mathcal{S}_ℓ (see (14)). We remark that the explicit computation and storage of the transformation matrix elements results in a substantial increase in efficiency because it avoids the usual assembly process during each iteration step and that the proposed overlay scheme allows the analysis of large nonrectangular patch arrays because storage of a fully populated BI system matrix is avoided. The user needs only to provide an additional data file that flags the uniform grid edges lying on a PEC element, and this is an important user-oriented feature of the formulation. Following the same procedure, we can obtain the expression for the entries of the backward transformation matrix. It should be noted that assuming each uniform grid edge traverses three or less nonuniform grid triangles, the nonzero entries in each row of $[T_F]$ will be 9 or less. However, they can reach a maximum of 18 if the midpoint and endpoints reside on an edge of the nonuniform grid. The maximum nonzero entries in each row of $[T_B]$ will be 15, but the typical number will be much less.

IV. NUMERICAL CONSIDERATIONS

Based on the presented FE-BI formulation, a computer program was written for the analysis of the radiation and scattering by cavity-backed patch antennas of arbitrary shape. The antenna geometry is supplied to this program in an input file that, as a minimum, must contain lists of 1) the nodes and their (x, y, z) coordinates, 2) the nodes forming each tetrahedron, 3) the nodes on the cavity aperture, and 4) the nodes on metallic boundaries. For arbitrary antenna geometries, it is necessary to employ a sophisticated volume mesh generation package, and a number of these are available commercially. Typically, each of these packages generates a "universal file" that can be readily preprocessed to extract the aforementioned input lists.

A major effort was devoted to writing the program in a manner that minimizes the storage and computational requirements. Specifically, the boundary conditions on the metallic surfaces are enforced *a priori* to obtain a system that involves only nonzero field components. The sparse finite element matrix was stored as a single array of length $N_u N_{nz}$, where N_u is the total number of unknowns within the cavity volume and N_{nz} denotes the maximum number of nonzero row entries. The BI matrix was stored in different ways, depending on whether the FFT was to be employed for the evaluation of the matrix-vector products. If the BiCG solution was to be carried out without the FFT, then the $N_u \times N_u$ BI integral matrix was added to the FE array, resulting in a 1-D array about $N_u N_{nz} + N_u^2$ long. For slot antennas, including cavity-backed spirals, and moderately sized systems, it was found preferable not to use the FFT, thus avoiding any interpolation errors. In that case the generation of a single combined FE-BI matrix before execution of the BiCG algorithm reduces the computational requirements. This is because a number

of operations associated with the repeated combinations of the FE and BI subsystems within the BiCG iteration is avoided.

When the FFT is to be used as part of the BiCG solver, the FE and BI matrices must be kept in separate arrays throughout the execution process. In this case, the FE matrix is again stored as a single array, and similarly the nonredundant elements of the BI matrix are stored in another single array of length $9N(2M - 1)$. The factor of nine is due to the three classes of edges, and as usual M and N denote the number of elements along the x and y directions, respectively. Because of the storage and computational efficiency of the BiCG-FFT algorithm, it is necessary to resort to uniform aperture grids for conformal antennas involving a substantial number of aperture edges. Of course, one should always use uniform triangular grids when the patches on the aperture are rectangular or if the array supports a superstrate. In the case of nonrectangular patches it will be necessary to overlay a structured triangular grid over the unstructured grid generated by the mesh generator. This must be done in the preprocessing stage, and should be taken into account when constructing the FE matrix. For scattering computations, the overlay of the structured grid is almost always the preferred approach because it does not, generally, compromise the accuracy of the computed scattering cross section. However, for antenna parameter computations, the interpolation scheme between the structured and unstructured grid edges may be of concern, depending on the specific antenna geometry. Generally, thin annular slots and planar spirals should be treated without resorting to structured grids, and to our experience this does not cause a large computational burden because these antennas are associated with small apertures. In the case of circular, triangular, or other nonrectangular patches, the structured grid was not seen to compromise the computational accuracy. Of course, conclusions based on one type of antenna do not necessarily apply to others, and thus the suggested alternatives must be examined separately for each antenna before choosing one approach over the other. Of importance here is that the formulation is suitable for modeling any antenna shape and feed structure.

V. RESULTS

We present below some representative numerical results for the purpose of validating and demonstrating the robustness of the tetrahedral formulation for scattering and radiation by different configurations of cavity-backed antennas. In each case the computed results via the FE-BI method are compared with reference measured or calculated data.

Scattering and radiation by a circular patch: Fig. 4 illustrates a circular patch residing on the surface of a 0.406 cm thick substrate having a relative dielectric constant of $\epsilon_r = 2.9$. The patch's diameter is 2.6 cm, and the substrate is enclosed in a circular cavity 6.292 cm wide. This cavity and the patch are recessed in a low cross section body for measuring its RCS. A comparison of the measured and calculated backscatter RCS as a function of frequency is also shown in Fig. 4. For this computation, the direction of the incident plane wave

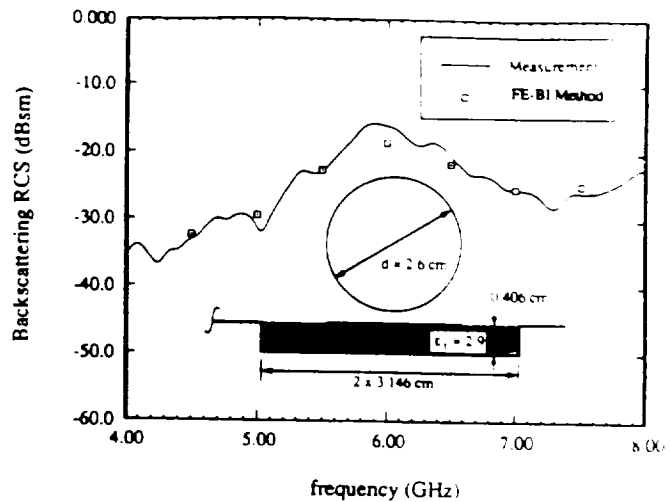


Fig. 4. Comparison of the computed and measured σ_{bs} back scatter RCS as a function of frequency for the shown circular patch. The incidence angle was 30° off the ground plane.

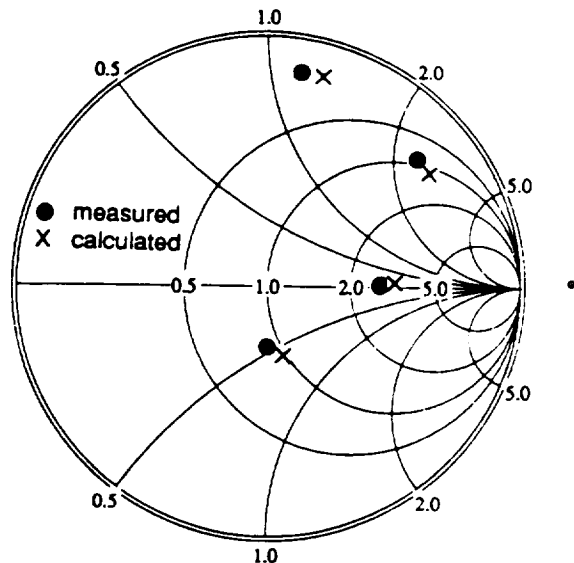


Fig. 5. Comparison of the computed and measured input impedance for the circular path shown in Fig. 4. The feed was placed 0.8 cm from the center of the patch, and the frequency was swept from 3 GHz to 3.8 GHz.

was 60° from normal, and as seen the agreement between measurements and calculations is very good throughout the 4–9 GHz band. Input impedance measurements and calculations for the same patch are displayed in Fig. 5. The probe feed in this case was placed 0.8 cm from the patch's center, and it is again seen that the measurements and calculations are in good agreement.

Radiation by a one-arm conical spiral: We considered the modeling of this radiator to demonstrate the geometrical versatility of the FE-BI method. Two projections of the spiral radiator and surface mesh are illustrated in Fig. 6. The top and bottom edges of the strip forming the spiral follow the lines $\rho = 0.0503\lambda \exp[0.221(\phi \pm 2.66)]$, $z = a_{\pm} \exp(0.221\phi)$.

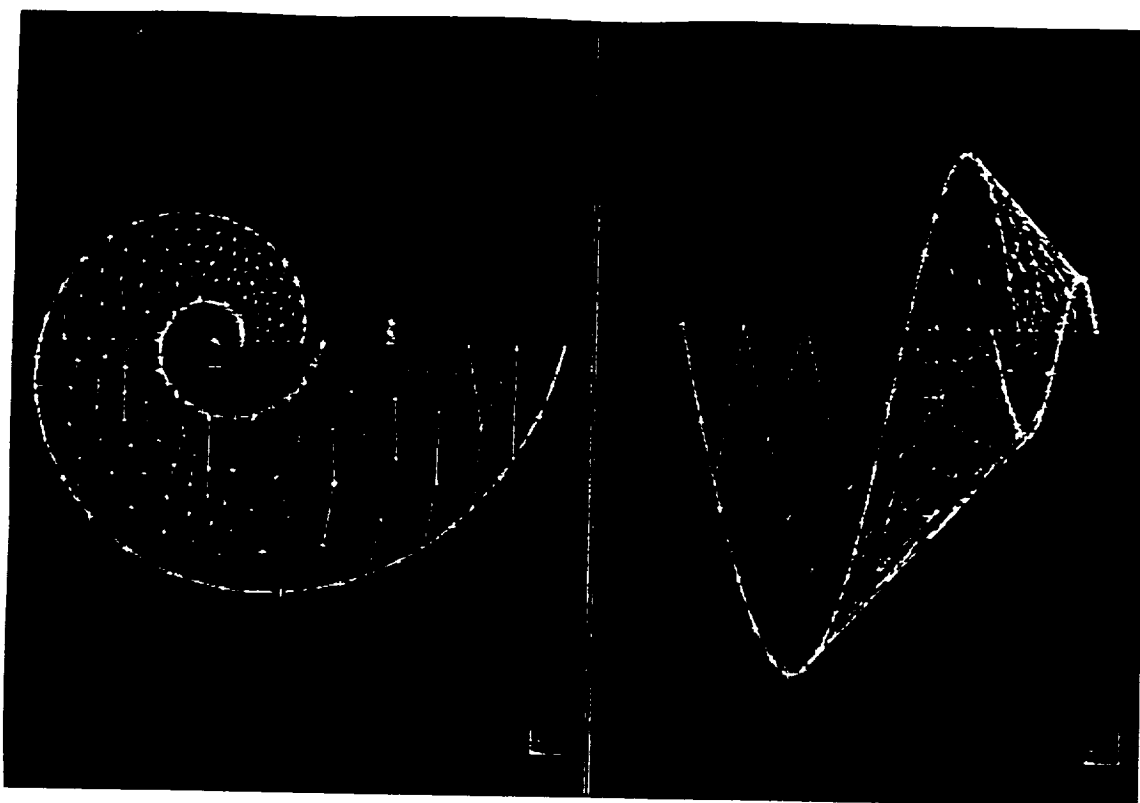


Fig. 6. Illustration of the configuration and mesh of the one-arm conical spiral used for the computation of Fig. 7.

where (ρ, ϕ, z) denote the standard cylindrical coordinates, a_{\pm} are equal to 0.0832λ and 0.0257λ , respectively, and $0 < \phi < 2\pi$. This spiral arm resides on an inverted cone (9.24 cm tall) whose bottom cross section has a diameter of 1.68 cm and the top cross section has a diameter of 21.78 cm. For our calculations $\lambda = 30$ cm ($f = 1$ GHz) and the spiral was situated in a circular cavity 10.01 cm deep. The computed E_{θ} principal plane radiation pattern taken in the $\phi = 90^{\circ}$ plane, using a probe feed at the cavity base, is given in Fig. 7. It is seen that this pattern is in good agreement with the data given in [12]. As can be expected, the E_{θ} pattern (not shown) differed from the measured data near the horizon because of interference from the finite circular cavity housing the spiral that was included in the analytical model. The latter was not part of the measurement configuration, which consisted of the spiral antenna on a large circular plate.

Annular slot impedance: Fig. 8 shows a narrow circular (0.75 cm wide) annular slot situated in a circular cavity 24.7 cm wide and 3 cm deep. Because the annular slot is narrow, the implementation of the BI subsystem is very small for this application, and as a result there is no need to invoke the FFT in the BiCG algorithm. The FE-BI method is basically quite effective in modeling small aperture configurations without a need for special computational considerations. Input impedance calculations as a function of frequency for this radiator, excited by a probe placed across the slot, are shown in Fig. 8, and agree well with the values calculated via a modal-boundary integral method [14]. For these calculations, the frequency was swept from 700–1000 MHz. The dielectric

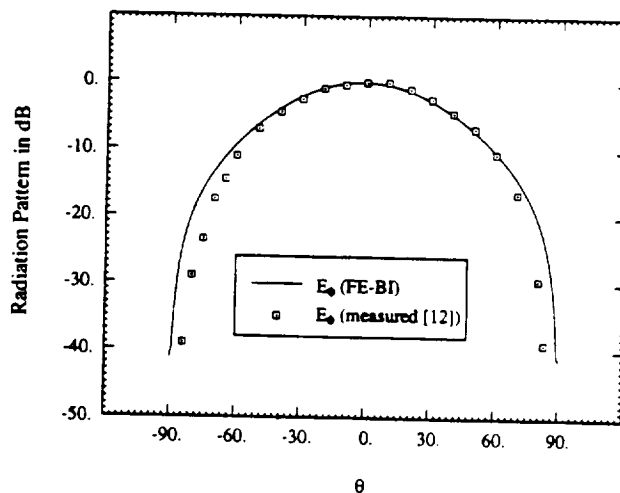


Fig. 7. Comparison of the calculated radiation pattern (E_{θ}), taken in the $\phi = 90^{\circ}$ plane, with data in reference [12] for the one-arm conical spiral shown in Fig. 6.

constant of the material filling the cavity was set to $\epsilon_r = 1.35$ as in [14], and this is an effective value to account for the presence of a dielectric slot cover used as part of the measurement model for holding the plate.

VI. CONCLUSION

We presented a hybrid finite element-boundary integral (FE-BI) formulation that incorporates linear tetrahedrals. The

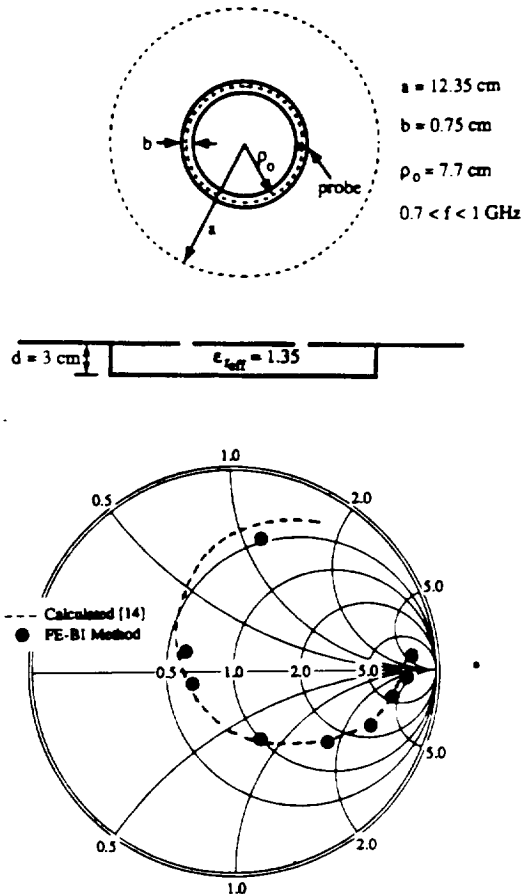


Fig. 8. Comparison of input impedance calculations for the illustrated cavity-backed slot.

method was specifically developed for the radiation and scattering analysis of cavity-backed printed antennas, where the FEM is used for modeling the cavity region and the BI equation acts as a global boundary condition for terminating the mesh on the cavity aperture. The FE-BI formulation is particularly suited for the analysis of complex configurations, and much emphasis was given here in developing a solution technique requiring $O(N)$ storage in spite of the resulting fully populated BI subsystem. The latter was achieved by making use of the convolutional property resulting from the structured mesh, thus permitting use of the FFT in the BiCG iterative solver for computing the matrix-vector products. For nonrectangular patch geometry, a novel numerical scheme is proposed to overlay on the unstructured free mesh a uniform triangular grid, avoiding the storage of the large BI subsystem. For scattering calculations associated with large aperture structures, use of the FFT proved essential in minimizing the computational requirements.

A number of patches, slots, and planar and nonplanar spiral antennas were analyzed for the purpose of demonstrating the versatility and accuracy of the FE-BI technique. Certainly, the need to use a sophisticated mesh generation package is deterrent to the application of the technique for the analysis of simple antenna configurations. However, this is unavoidable when dealing with complex geometries and, moreover,

the pervasive use of such commercial packages on desktop computers makes the technique quite attractive

REFERENCES

- [1] E. H. Newman and P. Tulyathan, "Analysis of microstrip antennas using moment methods," *IEEE Trans. Antennas Propagat.*, vol. AP-29, pp. 47-53, Jan. 1981.
- [2] J. R. Mosig and F. E. Gardiol, "Analytical and numerical techniques in Green's function treatment of microstrip antennas and scatterers," *IEE Proc., Pt. H*, vol. 130, pp. 175-182, 1983.
- [3] M. C. Bailey and M. D. Deshpande, "Analysis of elliptical and circular microstrip antennas using moment methods," *IEEE Trans. Antennas Propagat.*, vol. AP-33, pp. 854-959, Sept. 1985.
- [4] D. Zhang and K. A. Michalski, "Analysis of coaxial fed antennas of arbitrary shape with thick substrates," *J. Electromagn. Waves Appl.*, vol. 25, no. 12, pp. 1303-1327, 1991.
- [5] J. M. Jin and J. L. Volakis, "A hybrid finite element method for scattering and radiation by microstrip patch antennas and arrays residing in a cavity," *IEEE Trans. Antennas Propagat.*, vol. 39, no. 11, pp. 1598-1604, Nov. 1991.
- [6] ———, "A biconjugate gradient FFT solution for scattering by planar plates," *Electromagnetics*, vol. 12, pp. 105-119, 1992.
- [7] A. F. Peterson, S. L. Ray, C. H. Chan, and R. Mittra, "Numerical implementations of the conjugate gradient method and the CG-FFT for electromagnetic scattering," in *PIER 5: Application of Conjugate Gradient Method to Electromagnetics and Signal Analysis*, T. K. Sarkar, ed. New York: Elsevier, 1991, ch. 7.
- [8] M. L. Barton and Z. J. Cendes, "New vector finite elements for three dimensional magnetic field computations," *J. Appl. Phys.*, vol. 61, no. 8, pp. 3919-3921, 1987.
- [9] A. Chatterjee, J. M. Jin, and J. L. Volakis, "Computation of cavity resonances using edge-based finite elements," *IEEE Trans. Microwave Theory Tech.*, vol. 40, pp. 2106-2108, Nov. 1992.
- [10] S. M. Rao, D. R. Wilton and A. W. Glisson, "Electromagnetic scattering by surfaces of arbitrary shape," *IEEE Trans. Antennas Propagat.*, vol. AP-30, pp. 409-418, May 1982.
- [11] J. L. Volakis, J. Gong, and A. Alexanian, "Electromagnetic scattering from microstrip patch antennas and spirals residing in a cavity," *Electromagnetics*, vol. 14, no. 1, pp. 63-85, 1994.
- [12] D. W. Smith and P. E. Mayes, "Numerical and experimental analysis of circularly polarized radiating line antennas," Univ. of Illinois, Electromagnetics Lab. Rep. 90-4, 1990.
- [13] T. K. Sarkar, "On the application of the biconjugate gradient method," *J. Electromagn. Waves Appl.*, vol. 1, no. 3, pp. 223-242, 1987.
- [14] H. Morishita, K. Hirasawa, and K. Fujimoto, "Analysis of a cavity-backed annular slot antenna with one point shorted," *IEEE Trans. Antennas Propagat.*, pp. 1472-1478, Oct. 1991.
- [15] A.K. Jain, *Fundamentals of Digital Image Processing*. Englewood Cliffs, NJ: Prentice, 1989.



Jian Gong (S'91) was born in Jiangsu, China. He received the B.S. degree in physics from Shandong University, China, in 1982, and the M.S. degree in electrical engineering in 1992 from the University of Michigan, Ann Arbor, where he is currently pursuing the Ph.D. degree.

Since then, he has served as a lecturer at China University of Mining and Technology (CUMT), Jiangsu, China. During the period 1988-1990 he was a Research Associate at the School of Electronic and Electrical Engineering, University of Birmingham, Birmingham, UK. From 1990 to 1991 he was a Graduate Teaching Assistant in the Center for Imaging Science at Rochester Institute of Technology, Rochester, NY. Since September 1991 he has been a Graduate Research Assistant at the Radiation Laboratory, University of Michigan. His current interests include computational electromagnetics as applied to wave propagation/scattering as well as antenna simulation and design.

Mr. Gong is a member of Tau Beta Pi.